Production of Antiprotons in Interactions of Light Nuclei and the Search for Dark Matter in Space Experiments

Presented by

Reham Ibrahim Sayed Ibrahim

A Thesis Submitted
to
Faculty of Science

In Partial Fulfillment of the
Requirements for
the Degree of
Doctor of Philosophy
(Mathematical Astronomy)

Department of Astronomy, Space Science, and Meteorology
Faculty of Science
Cairo University

(2021)

Abstract

Student Name: Reham Ibrahim Sayed Ibrahim

Title of the thesis: Production of Antiprotons in Interactions of Light Nuclei and the Search for Dark Matter in Space Experiments

Degree: Doctor of Philosophy (Mathematical Astronomy)

The aim of the thesis is to review the recent antiproton results from space experiments for the indirect detection of dark matter. The evidence of dark matter is reviewed. The different candidates and search approaches are discussed. The several uncertainties challenging the confirmation of the recent AMS-02 signal are reviewed. The upcoming SPD experiment at the NICA collider is introduced. A Monte Carlo study for the measurement of antiproton yield at the SPD is performed. It is shown that the SPD experiment could significantly contribute to the indirect search for dark matter by lowering the uncertainty on the antiproton-production cross sections.

Keywords: Dark Matter, Space Experiments, Cosmic Rays,
Spin Physics Detector

Spervisors: **Signature:**

1 - Prof. Hayman Metwally

2 - Prof. Alexey Guskov

Prof. S. M. Robaa

Chairman of Department of Astronomy,
Space Science, and Meteorology
Faculty of Science – Cairo University

Acknowledgments

I would first like to express my gratitude to both my supervisors: Prof. Z. M. Hayman, for being the best mentor a person can hope to have and for teaching me to navigate the world of academia; and Prof. A. V. Guskov, for the idea behind this thesis and for giving me the opportunity to work with him during these years, and for his patient guidance during them.

I am thankful for the JINR institute for facilitating my visits there during working on this thesis. I would also like to acknowledge the team at the Dzhelepov Laboratory of Nuclear Problems at JINR for welcoming me during these visits. I would like to thank my colleagues at the Astronomy Department of Cairo University for the great moments we share together that keep us going.

Finally, I am grateful for my family for their support during me whole journey. I would like to particularly thank my brother for always being there to listen to me vent.

Summary

The aim of the thesis is to review the recent antiproton results from space experiments for the indirect detection of dark matter; review the uncertainties surrounding the recent AMS-02 signal; and, finally, assess the possibility of measuring the antiproton yield at the upcoming Spin Physics Detector at the NICA collider.

The thesis contains seven chapters, and a list of references:

Chapter 1: Evidence of Dark Matter

In this chapter, the evidence of dark matter is reviewed. The account given focused on the rotation curves of spiral galaxies, the mass discrepancy in galaxy clusters, and observations of gravitational lensing in the absence of luminous lenses. The Bullet Cluster event was discussed as the strongest indicator of the collisionless nature of dark matter.

Chapter 2: Basics of Particle Physics

In this chapter, the fundamental particles of the Standard Model of particle physics were introduced. The four fundamental forces of nature were discussed, along with the theory that govern each force and the particle mediators that facilitate the corresponding interactions. A brief account of the Standard Model successes and challenges was given.

Chapter 3: Types and Candidates of Dark Matter

In this chapter, the different classifications of dark matter candidates are discussed. The most-explored candidates are reviewed in further detail; such as MACHOs, WIMPs, axions, and more. Alternative interpretations of the dark-matter phenomena were also discussed in light of theories of modified gravity.

Chapter 4: Searches for Dark Matter

In this chapter, the different approaches employed to pursue the identity of dark matter are reviewed; including collider searches, direct detection, and indirect detection of dark matter. The paradigms underlying each approach are discussed, along with hypotheses common to all approaches. A brief account of recent results and upcoming efforts was given for each approach.

Chapter 5: Antiprotons as a Probe for Dark Matter

In this chapter, the properties of primary and secondary cosmic rays were reviewed. The recent antiproton results from space experiments for the indirect detection of dark matter are discussed. The uncertainties surrounding the recent AMS-02 signal are explored. The next steps and outlook for minimizing the uncertainties are reviewed.

Chapter 6: The Spin Physics Detector at NICA

In this chapter, the Spin Physics Detector is introduced. The motivation and objectives of the program are outlined. The general layout and main components of the detector are described. The computing system of the experiment and the SpdRoot toolkit are discussed. The planned timeline for the project is outlined.

Chapter 7: Measuring Antiproton Production at NICA

In this chapter, an introduction was first given about the motivation behind this work. The measurements of antiproton yield at the SPD were proposed. Then, a Monte Carlo simulation study was performed in two stages: first, using Pythia8, and second, using the SpdRoot toolkit. The different aspects and requirements of the proposed measurements were assessed in light of the planned capabilities of the SPD. Finally, a discussion was given about the results obtained and the next steps for which this thesis lays the ground.

Contents

Abstract **i**

Acknowledgments **ix**

Summary **xi**

Contents **xv**

List of Tables **xix**

List of Figures **xxi**

List of Abbreviations **xxvi**

Introduction **1**

1 Evidence of Dark Matter **9**

1.1 Rotation Curves of Spiral Galaxies 12

1.2 Galaxy Clusters 14

1.3 Gravitational Lensing 19

Bullet Cluster 24

1.4 The Cosmic Web 24

1.5 Discussion 26

2 Basics of Particle Physics 29
2.1 Fundamental Particles 31
2.2 Four Forces of Nature 34
2.3 The Standard Model 38
2.4 Discussion 40

3 Types and Candidates of Dark Matter 43
3.1 Types of Dark Matter 45
Production 45
Particle Nature 46
Mass and Speed 47
3.2 Candidates of Dark Matter 47
3.2.1 MACHOs 48
3.2.2 SM Neutrinos 53
3.2.3 WIMPs 56
3.2.4 Sterile Neutrinos 58
3.2.5 Axions 62
3.2.6 Modified Gravity as an Alternative to Dark Matter 64
3.3 Discussion 69

4 Searches for Dark Matter 73
4.1 Collider Searches 76
4.2 Direct Detection 83
4.3 Indirect Detection 91
4.4 Discussion 97

5 Antiprotons as a Probe for Dark Matter 101
5.1 Cosmic Rays 103
5.2 AMS-02 Antiprotons Results 112

5.3 Uncertainties 118
5.4 Antiproton Production in Hadronic Collisions 124
5.5 Discussion 133

6 The Spin Physics Detector at NICA 137

6.1 Motivation & Aims 139
6.2 Polarized Beams & Detector Setup 142
6.3 Computing System 149
  6.3.1 SpdRoot 151
6.4 Project Timeline & Discussion 152

7 Measuring Antiproton Production at NICA 155

7.1 Introduction & Motivation 157
7.2 Antiproton Production Simulation Using Pythia8 159
7.3 Antiproton Production Simulation Using SpdRoot 164

Concluding Remarks 175

References 183

Arabic Summary 201

List of Tables

2.1 Elementary fermions 33
2.2 Elementary bosons 33
2.3 The four fundamental forces 36

4.1 Direct detection experiments 90

5.1 Abundances of light isotopes in CRs 130
5.2 Relative contributions of antiproton-production channels . 130

7.1 The relative yields of antiprotons in MC *pp* collisions . . . 162

List of Figures

1 The microscopic and macroscopic worlds 5

1.1 The rotation curve of the Milky Way 14
1.2 The main parts of the Milky Way 15
1.3 Gravitational lensing 20
1.4 Lensing configuration 22
1.5 The Bullet Cluster event 25

3.1 Results from the MACHO project 50
3.2 Constraints of the PBHs density parameter 54
3.3 Axions parameter space 65
3.4 The rotation curve from Milgrom's formula 68
3.5 Newtonian and MOND dynamical masses for galaxy clusters 68

4.1 Potential interactions of DM with ordinary particles 76
4.2 Missing transverse momentum 80
4.3 Recoil energy spectra 85
4.4 Recoil modulation 86
4.5 DAMA modulation results 92
4.6 WIMP constraint set 92
4.7 Positron fraction spectrum 98

5.1 Elemental abundances in CRs and the solar system 104
5.2 Primary CRs spectrum 105
5.3 Primary spectrum modulation 107
5.4 A particle cascade 109
5.5 Compilation of particle ratios in CRs 110
5.6 Outline of the AMS-02 114
5.7 Primary proton and helium spectra 115
5.8 Constraints on DM mass and annihilation cross section . . 117
5.9 Sources of uncertainty of antiproton signal 123
5.10 Accumulative uncertainty on antiproton signal 124
5.11 The isospin factor 126
5.12 The ratio $\bar{\Lambda}/\bar{p}$ in pp collisions 127
5.13 Comparison of parameterizations 128
5.14 The parameter space requiring coverage 132

6.1 General layout of the SPD setup 141
6.2 Luminosity and beam intensity dependence on proton energy 142
6.3 The general layout of the SPD 145
6.4 The SPD beam pipe 146
6.5 The SPD vertex detector 146
6.6 The SPD electromagnetic calorimeter 148
6.7 Proposed technologies for the SPD time-of-flight system . . 149
6.8 The SPD computing system 151

7.1 Antiproton-production cross sections in MC pp collisions . 161
7.2 The angular distribution of produced antiprotons 161
7.3 Antiprotons momentum spectra according to production mechanisms 162

7.4 Momentum spectra of antiprotons and negative pions and kaons . . . 165
7.5 The SPD kinematic range using Pythia8 . . . 165
7.6 The SPD kinematic range using SpdRoot . . . 166
7.7 Antiproton detection efficiency . . . 167
7.8 Event-time reconstruction accuracy . . . 169
7.9 The relative speeds of charged particles . . . 170
7.10 Mass reconstruction for antiprotons and negative pions and kaons . . . 171
7.11 The $\bar{\Lambda}/\bar{p}$ ratio range accessible at the SPD . . . 172
7.12 Reconstruction of hyperon decays . . . 173

List of Abbreviations

AMS	Alpha Magentic Spectrometer
B/C	Boron-to-Carbon ratio
BH	Black Hole
BSM	Beyond the Standard Model
CDM	Cold Dark Matter
CDR	Conceptual Design Report
CM	Center of Mass
CMBR	Cosmic Microwave Background Radiation
CP	Charge-conjugation Parity
CRs	Cosmic Rays
DAQ	Data AcQuisition
DD	Direct Detection
DM	Dark Matter
ECal	Electromagnetic Calorimeter
GR	General Relativity
GUT	Grand Unified Theory
HDM	Hot Dark Matter
ID	Indirect Detection
ISM	InterStellar Medium
ISS	International Space Station
LHC	Large Hadron Collider
LMC	Large Magellanic Cloud

MACHO	MAssive Compact Halo Object
MC	Monte Carlo
ML	Machine Learning
MOND	MOdified Non-relativistic Dynamics
NICA	Nuclotron-based Ion Collider fAcility
PAC	Programme Advisory Committee
PBH	Primordial Black Hole
PDF	Parton Distribution Function
PDG	Particle Data Group
PID	Particle IDentification
QCD	Quantum ChromoDynamics
QED	Quantum ElectroDynamics
R&D	Research and Development
SM	Standard Model of particle physics
SPD	Spin Physics Detector
SUSY	SUperSYmmetry
TDR	Technical Design Report
TeVeS	Tensor-Vector-Scalar theory
TOA	Top Of the Atmosphere
TOF	Time Of Flight
VD	Vertex Detector
WDM	Warm Dark Matter
WIMP	Weakly Interacting Massive Particle

Introduction

It had once been thought that the contents of the Universe are those that we can see; but as time went on, we found out that what we can see is only a sliver of the electromagnetic spectrum. So we started to understand that “there are more things in Heaven and Earth” than we can perceive with our eyes. We then developed tools and instruments to allow us to detect what we cannot see, which includes all the rest of the spectrum from radio waves to gamma rays. A few decades later, we were confronted with another harsh fact; that is, what we can detect electromagnetically makes up less than a tenth of the contents of the Universe. We thus came to be introduced to the “Dark Universe”; namely, dark matter and dark energy. Dark energy is widely known as the driver of the accelerating expansion of the Universe, notwithstanding that we do not yet understand its nature. Now, dark energy is known to make up around 68% of the energy budget of the Universe. As for dark matter, it makes up about 27% of that budget. This leaves only about 5% that is made up of all the objects we can electromagnetically observe, including every living organism. Although there has been a lot of evidence of dark matter, the first compelling observations that established its existence were of the discrepancy between luminous masses and gravitational masses in galaxies and galaxy clusters. The observations proved one time after another that the gravitational drive in these celestial objects cannot be attributed to luminous matter alone. This meant that there is a component that has a gravitational effect but no electromagnetic one; hence, *dark matter*.

Along our journey in understanding the forces at work in the physical world, four fundamental forces have been known to govern the Universe, from the micro to the macro (see Figure 1). These forces are: gravity, electromagnetism, the weak force, and the strong force. Each of them is known to be responsible for one form of interaction, and each of them is governed or interpreted by one standing theory. Since the discovery of these forces, physicists were able to unify three of them within one theory, known as the Standard Model of particle physics. But one force remains out of reach; that is, gravity. Although the General Theory of Relativity has achieved remarkable successes in the arena of gravity, dark matter and dark energy still challenge it to this day. It is not surprising that Einstein, after the publication of his theory of general relativity, went on a quest to unify the forces of nature. He believed that the answer lies there as well. Nevertheless, that was one quest he could not conquer. The incompatibility between gravity and the rest of the forces manifests clearly in dark matter, where all the evidence of it is gravitational in nature with no hope of solving the mystery without integrating the rest of the forces into the solution.

There are no short of candidates and theories for the identity of dark matter. They vary to include non-interactive Standard Model particles, new exotic particles, and even new gravitational theories that accommodate the effects of dark matter. However, there is no proof so far that validates a specific theory. To experimentally look for the required proof, several approaches are utilized. These are collider searches, direct detection, and indirect detection. Each of these approaches is based on a different hypothesis, but they all share the ideas that the dark matter effects are caused by a new particle that have not yet been identified, and that there is some form of interaction between that new particle species and the Standard Model particles. No one search technique can accomplish the goal alone. They all complement each other to add to the constraints of the properties of potential dark matter candidates, while

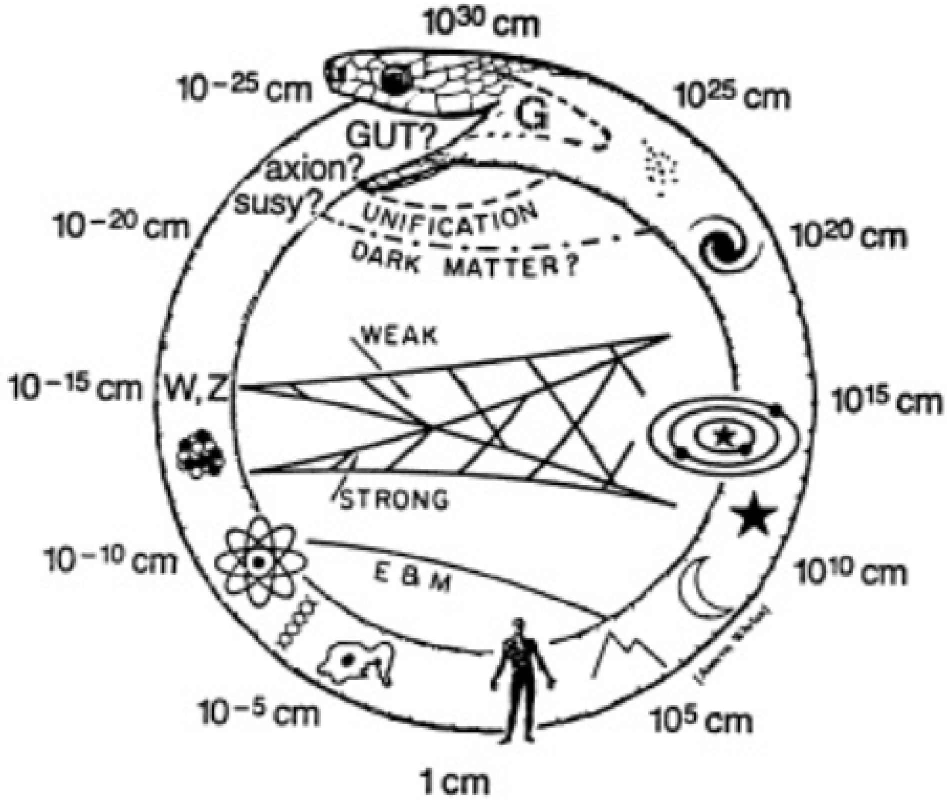

Figure 1: The modified Uroboros representing the links between the microscopic (*left*) and macroscopic (*right*) worlds[1].

each of them might have its blind spots.

Indirect detection experiments are based on the hypothesis that dark matter particles decay and pair-annihilate producing Standard Model particles as final products. They thus seek to detect these final products as anomalies in rare cosmic ray components. This is usually done by measuring the flux of different CR components with high precision, either by ground-based, balloon, or space-based experiments; depending on the targeted CR component. The most recent of these experiments is the AMS-02 spectrometer which is targeting charged cosmic rays; and have measured the fluxes of electrons, positrons, protons, and antiprotons with unprecedented precision that exceeds 95%. Among the results of the AMS-02 was the antiproton-to-proton flux ratio covering energies up to 450 GeV. The measurements indicate a signal that could be associated with a dark matter particle of a mass around 80 GeV/c^2. However, the signal is surrounded by several sources of uncertainty including galactic propagation parameters, solar modulation, and primary CR spectra. But the uncertainty that is most dominant originates from the antiproton-production cross sections. The collective effect of all uncertainties is to bring the statistical significance of the signal from above $5\,\sigma$ to below $2\,\sigma$.

Secondary cosmic rays, such as antiprotons, are produced in collisions of primary cosmic rays with the nuclei of the interstellar medium. Most secondary antiprotons are produced in proton-proton, proton-helium, and helium-helium collisions, while the contribution of heavier-nuclei collisions is negligible. To detect any potential anomaly in the cosmic antiproton spectrum, the secondary production has to first be subtracted from the overall flux. To do that, we need to have accurate estimations of the production cross sections of antiprotons in each collision channel, with a precision that matches that of the original measurements. Moreover, antiprotons are also produced eventually by decays of short-lived hyperons and antineutrons. This production mechanism also has to be taken into account. Unfortunately, the data on antiproton production in hadronic collisions are scarce at best. There are only a few datasets of proton-proton collisions, while the first proton-helium dataset was released in 2018 by the LHCb collaboration. In addition, most of the datasets available on proton-proton collisions are decades old and did not apply a feed-down correction for antiproton production via decays.

During the last few years, several studies have been devoted to defining the range of measurements for the antiproton-production cross sections required in order to match the precision level of the AMS-02 measurements. These efforts have succeeded in outlining the parameter space that requires coverage. At this point, several experiments started to adopt this requirement as part of their physics programs, such as LHCb and COMPASS++/AMBER. However, each experiment would have different kinematic access according to its operation mode and energy scales. It is unlikely that one experiment could cover the entire parameter space required.

The Spin Physics Detector (SPD) is planned to be constructed at the Nuclotron-based Ion Collider fAcility (NICA) at JINR, in Dubna, Russia. It is planned as a universal facility for studying nucleon spin structure and related phenomena. The experiment will use proton and deuteron beams in its first stage, with the possibility to include helium in later stages. With a luminosity of up to 10^{32} cm^{-2}s^{-1}, and a 4π coverage, the SPD will likely be able to contribute to the indirect search for dark matter by performing the measurements of antiproton-production cross sections required for minimizing the corresponding uncertainty on the recent AMS-02 signal, or any potential upcoming signal in fact.

In this work, we are going to investigate the possibility of performing these measurements and their potential impact on optimizing our ability to draw a conclusion regarding the AMS-02 signal. We will first explore a more-thorough account of our understanding of dark matter from the time we became aware of it until this point of time. Then we will start assessing the SPD capabilities against the proposed measurements, using Monte Carlo simulations and several estimation techniques. We will explore several factors; including detection efficiency, potential coverage, particle identification capabilities, and reconstruction of secondary decays. Finally, we will draw our conclusions from this study and outline the next steps that could be taken to optimize its use.

Chapter 1

Evidence of Dark Matter

In what follows, we are going to review the most compelling pieces of evidence of the existence of dark matter (DM), so far. For the purposes of this Chapter, we will define DM as non-luminous matter. In Chapter 3, we will discuss the different candidates for what DM can be made of.

Evidence of DM falls under a category that has been traditionally called "the astronomy of the invisible" (cf.[2, 3]). At some point in the history of astronomy, the outermost planets along with binary stars belonged to that category as well. It usually starts with a gravitational manifestation: some object is not where it is supposed to be; or another object is not moving the way it is expected to move. That is what happened in 1844 when the planet Uranus appeared to have shifted from its expected position. Later, a new planet, Neptune, was discovered, and found out to be the reason for Uranus' shift (cf.[2]). In that same year, Bessel noted the irregular motion of the star Sirius, the brightest star in the night sky (cf.[3]). He then suggested that an invisible companion to Sirius was causing the irregularity, which was proven in 1862 by Alvan Clarke when he observed Sirius B for the first time (cf.[2]).

In as much the same manner, in the 1930s, Zwicky realized that the dynamics of several galaxy clusters suggested that individual galaxies had a mass about a hundred times larger than expected from their luminosity (cf.[3–5]). The evidence continued to compile for several decades, which we will discuss in further details in the following Sections. However, in an age when seeing is believing, the astronomical community was still reluctant to accept the concept of DM. Nevertheless, by the year 1978, it was established that there is a huge matter component that does not emit any electromagnetic radiation; but one whose gravitational effects could no longer be overlooked (cf.[3, 6]).

1.1 Rotation Curves of Spiral Galaxies

From their luminosity, we know that spiral galaxies are supposed to have most of their masses concentrated in a central bulge, whereas the spiral arms form a disk around that bulge (cf.[5]). Any stars or gas within the gravitational field of the galaxy revolve around the galactic center. The rotation curve of a spiral galaxy—or, in fact, any type of galaxy—is a plot of the orbital speed at each point as a function of its distance from the galactic center (cf.[5, 6]). In general, the motion around the galactic center is fairly circular; but the orbital speed varies with distance so that it balances out the gravitational pull toward the center.

During the first half of the previous century, measuring rotation curves used to be performed spectroscopically by measuring the blue or red shifts of the light from the stars in the galaxies. However, this was quite limiting, since there are regions within the gravitational field where there are no stars. But after discovering the 21-cm line of neutral hydrogen in 1951, it was possible to extend the rotation curves as far as there is a neutral hydrogen component in the galactic gas. Then, radio astronomers were able to calculate the orbital speed at each point from measurements of the Doppler shift of the 21-cm line (cf.[5, 6]).

For a point at a distance r from the galactic center, the balance between the gravitational force and centrifugal force is given by (cf.[4, 5])

$$\frac{mv^2(r)}{r} = \frac{GmM(r)}{r^2}, \tag{1.1.1}$$

where m is the mass of the object affected by the field, $v(r)$ is the orbital speed at r, G is the gravitational constant, and $M(r)$ is the mass enclosed within the radius r. From (1.1.1), the orbital speed can be given by

$$v(r) = \sqrt{\frac{GM(r)}{r}}. \tag{1.1.2}$$

If the radius r is less than the radius R of the central bulge of the spiral galaxy, then the enclosed mass is given by (cf.[5])

$$M(r) = \frac{4}{3}\pi r^3 \rho, \tag{1.1.3}$$

where ρ is the average density within R. Otherwise, the enclosed mass is almost constant ($\sim M$) since the mass outside the central bulge is relatively negligible. Thus, we can conclude that

$$v(r) = \begin{cases} r\sqrt{\frac{4}{3}\pi G\rho} & \text{for} \quad r < R, \\ \sqrt{\frac{GM}{r}} & \text{for} \quad r \geq R. \end{cases} \tag{1.1.4}$$

The resulting rotation curve expected from (1.1.4) is a linear increase in the orbital speed from the center to the edge of the central bulge at R, then $v(r)$ is expected to decrease with the square root of r, which is called a *Keplerian decline* (cf.[2, 4, 7]). However, observations show that rotation curves of spiral galaxies plateau outside the central bulge of the galaxy. So, even though the orbital speed increases as expected for $r < R$, it appears to be almost constant for $r \geq R$ (cf.[3, 4, 7, 8]). This implies that the enclosed mass is still increasing proportionally with r outside the central bulge. Figure 1.1 shows both the expected and observed shapes of the rotation curves of a typical spiral galaxy; in this case, Our Milky Way.

Meanwhile, galactic mass distributions obtained from luminosity mea-

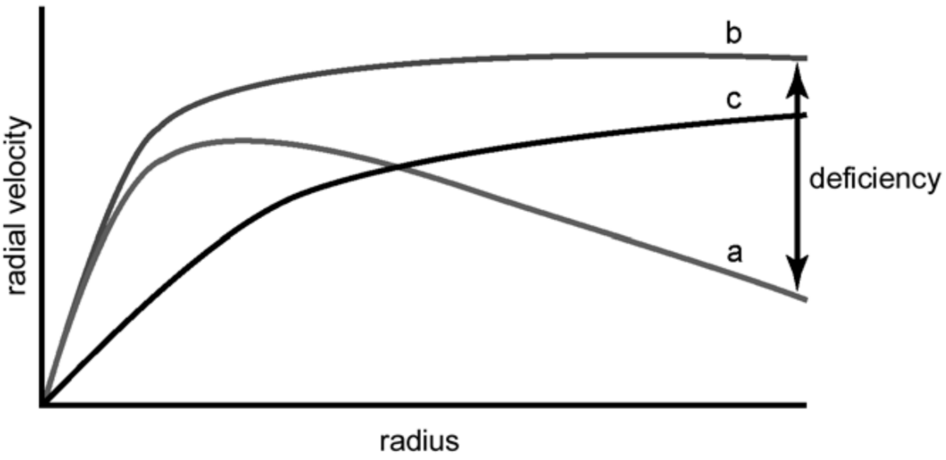

Figure 1.1: A schematic of (a) the expected and (b) the observed rotation curves of the Milky Way, and (c) the required addition from non-luminous (dark) matter to reconcile both curves [6].

surements give no indication that the mass is still growing outside the central bulge (cf.[3, 9]). The simplest explanation for this enigma is that there is an invisible matter component in the galaxy—that is, DM—that manifests gravitationally but does not give out any electromagnetic radiation (cf.[2, 6, 8]).

This adds to the importance of rotation curves, since they can help shed some light on the distribution of that non-luminous matter within the galaxy (cf.[4]). Astronomers utilized the fact that we reside in a spiral arm of the Milky Way to understand its main structure, which is shown in Figure 1.2. Rotation curves of spiral galaxies remain one of the most compelling pieces of evidence of the existence of DM.

1.2 Galaxy Clusters

A galaxy cluster is a bound system of galaxies that move under the effect of a common gravitational potential (cf.[5]). In general, galaxy clusters

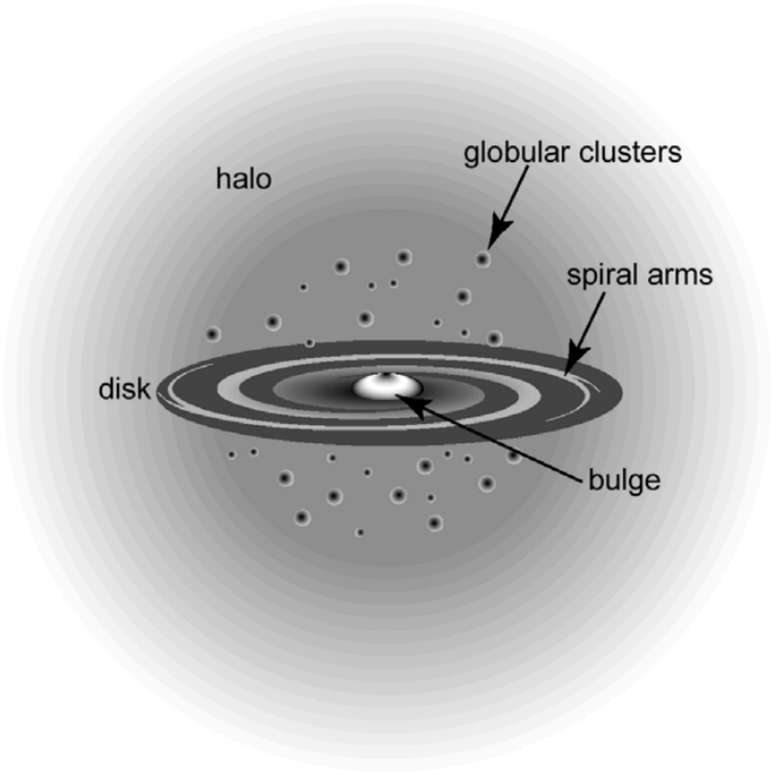

Figure 1.2: An outline of the main parts of the Milky Way[6].

are classified into regular and irregular. Regular clusters usually form spherical structures and contain mostly elliptical galaxies; while irregular clusters, which are more common, can contain any type of galaxy, and, as the name suggests, do not assume any certain shape (cf.[6]).

The study of galaxy clusters provide a magnifying glass of many astronomical disciplines, especially structure formation and cosmology. Unlike the stellar motion in galaxies, the motion of individual galaxies in a cluster is essentially random. However, by observing this motion, the collective mass of the galaxy cluster can be estimated. Another estimate of this mass can also be obtained using the luminosity of each member galaxy. The former estimate is usually referred to as the dynamical mass, while the latter is called the luminous mass (cf.[5]).

The dynamical mass of a galaxy cluster can be calculated using the *virial theorem*, which defines the relation between the time-averaged kinetic energy, K, and the time-averaged potential energy, W, for a bound system (cf.[5, 6]). For such a system composed of n point masses, the moment of inertia would be (cf.[5, 8])

$$I = \sum_{i=1}^{n} m_i r_i^2, \tag{1.2.1}$$

and its first and second derivatives would, respectively, be

$$\dot{I} = 2\sum_{i=1}^{n} m_i \vec{r}_i \cdot \vec{v}_i, \tag{1.2.2}$$

and

$$\ddot{I} = 2\sum_{i=1}^{n} m_i \left(v_i^2 + \vec{r}_i \cdot \ddot{\vec{r}}_i\right), \tag{1.2.3}$$

where m_i, $\vec{r}_i$, and $\vec{v}_i$ denote the mass, position, and velocity of the i^{th} particle. In a self-gravitating system, the acceleration of the i^{th} particle due to the effect of the other particles is given by (cf.[8])

$$\ddot{\vec{r}}_i = \sum_{j\neq i} G m_j \frac{(\vec{r}_j - \vec{r}_i)}{|\vec{r}_j - \vec{r}_i|^3}. \tag{1.2.4}$$

Substituting from (1.2.4) into (1.2.3), we obtain

$$\begin{aligned} \tfrac{1}{2}\ddot{I} &= 2K + \textstyle\sum_{i=1}^{n}\sum_{j\neq i} G m_i m_j \dfrac{\vec{r}_i \cdot (\vec{r}_j - \vec{r}_i)}{|\vec{r}_j - \vec{r}_i|^3} \\ &= 2K - \dfrac{G}{2}\textstyle\sum_{i=1}^{n}\sum_{j\neq i} \dfrac{m_i m_j}{|\vec{r}_i - \vec{r}_j|} \\ &= 2K + W, \end{aligned} \tag{1.2.5}$$

where

$$K = \frac{1}{2}\sum_{i=1}^{n} m_i v_i^2, \tag{1.2.6}$$

and

$$W = -\frac{G}{2}\sum_{i=1}^{n}\sum_{j\neq i}\frac{m_i m_j}{|\vec{r}_i - \vec{r}_j|}, \tag{1.2.7}$$

are the total kinetic energy and the total gravitational potential energy of the system, respectively (cf.[8]). However, for a system in a dynamical equilibrium, *i.e.* bound system, the time-averaged moment of inertia does not change when taken over several dynamical timescales (cf.[5, 8]), which is the average time a particle requires to complete one orbit within the system. Thus, (1.2.5) becomes

$$2\left\langle K\right\rangle_t + \left\langle W\right\rangle_t = 0, \tag{1.2.8}$$

where $\langle\rangle_t$ denotes the time average. When the age of a system is much longer than the dynamical timescale, the virial theorem is approximated to

$$2K + W \approx 0. \tag{1.2.9}$$

For a self-gravitating sphere, *e.g.* a galaxy cluster, the total potential energy can be calculated from (cf.[5])

$$\begin{aligned} W &= -\textstyle\int_0^R G\dfrac{\left(\frac{4}{3}\pi r^3\rho\right)\left(4\pi r^2\rho\right)}{r}dr \\ &= -G\tfrac{R^5}{5}\left(\tfrac{4}{3}\pi\rho\right)\left(4\pi\rho\right) \\ &= -\tfrac{3}{5}\tfrac{G}{R}\left(\tfrac{4}{3}\pi R^3\rho\right)^2 \\ &= -\frac{3}{5}\frac{GM^2}{R}, \end{aligned} \tag{1.2.10}$$

where M is the total mass, R is the radius, ρ is the average density, and

r is the radial distance. The total kinetic energy of such a system is given by (cf.[5])

$$K = \frac{1}{2} M v_{\mathrm{rms}}^2, \tag{1.2.11}$$

where v_{rms} is the root-mean-square speed of each particle in the system. Substituting from (1.2.10) and (1.2.11) into (1.2.9), the total mass of the system is given by

$$M = \frac{5}{3} \frac{R v_{\mathrm{rms}}^2}{G}. \tag{1.2.12}$$

Hence, if both R and v_{rms} are known, an estimate of the dynamical mass of a galaxy cluster can readily be obtained from (1.2.12).

In 1933, Zwicky applied the virial theorem to estimate the mass of the Coma Cluster (cf.[2, 5, 6]). The Coma Cluster was very convenient to study; because of its nearly-spherical structure, and its apparent position away from the plane of the Milky Way (cf.[5, 8]). Zwicky then estimated the luminous mass of the cluster based on the luminosities of the individual galaxies. He found an extremely large discrepancy between the two estimates, such that the ratio of the gravitational mass to the luminous mass was fifty to one (cf.[5, 6]). This meant that if the Coma Cluster only contained the mass estimated from its luminosity, its member galaxies would not have been bound together as they appear, according to their motion. This, in turn, implies that there is a large unaccounted-for mass component, *i.e.* DM.

Three years after Zwicky announced his findings, a similar study involving the Virgo Cluster was carried out by Sinclair Smith (cf.[5, 6]). He found the ratio of the gravitational mass to the luminous mass to be as large as one hundred. Decades later, with all the modern measurements, these first estimates turned out to be fairly accurate, and the problem of DM within galaxy clusters persists. A lot of other clusters have been studied as well. Now, it is even possible to map the DM distribution using this and several other techniques (cf.[2, 4]); some of which we will discuss in the rest of this Chapter.

1.3 Gravitational Lensing

Einstein's theory of general relativity (GR) is essentially based upon the idea that gravity and acceleration are equivalent. This is a consequence of the concept that mass dictates how space curves, while the curvature of space dictates how massive objects move (cf.[5, 6]). However, space curvature does not only affect matter, but also energy, which includes visible light. Thus, light follows the contours of space while it passes through it, which causes the phenomenon known as the *bending of light*.

The bending of light was one of the first predictions of GR. It was Eddington who first realized the possibility of observing this phenomenon for a beam of light passing through the vicinity of a large gravitational field. During the second decade of the twentieth century, the Sun was the most massive object available, so the light coming from the background stars of the sky area surrounding the Sun will bend when it passes through the gravitational field. But how to observe the stars during daylight? The answer was the 1919 total solar eclipse. Eddington led the expedition that observed that the apparent positions of the stars surrounding the sun shifted slightly but consistently from their apparent positions in the night sky (cf.[6, 8]). Thus the bending of light—and effectively, the general theory of relativity—was proven.

Gravitational lensing is a direct result of the bending of light, where a massive foreground object can bend the light coming from a background object, causing its image to appear distorted, amplified, and in some cases producing multiple images of the same object (cf.[2, 5, 10]). Thus, the first object acts as a lens, as shown in Figure 1.3, and hence the name of the phenomenon.

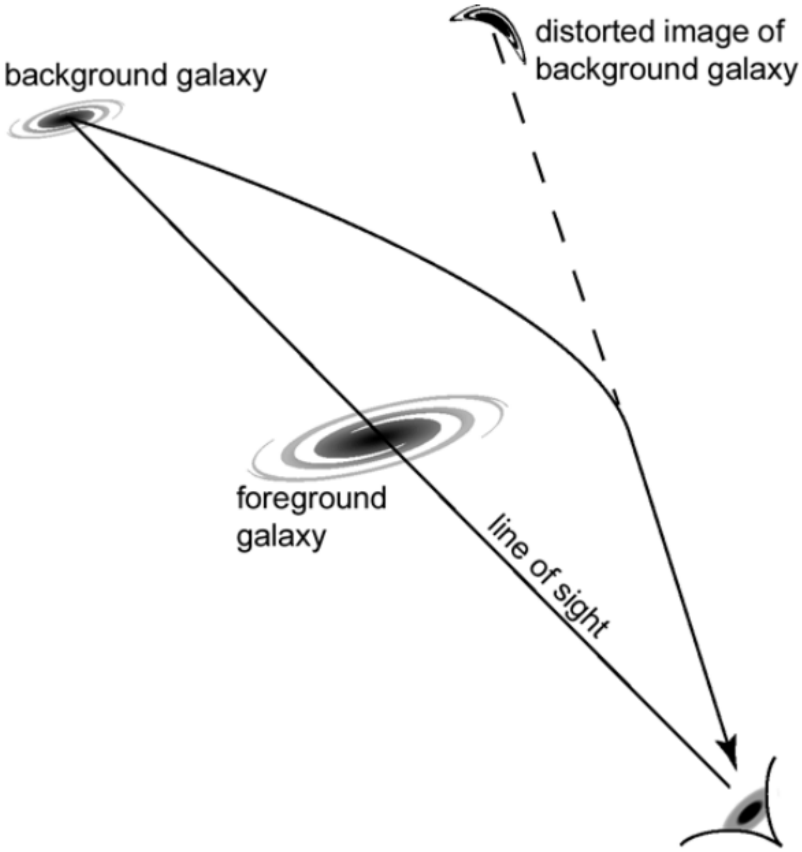

Figure 1.3: The phenomenon of gravitational lensing [6].

Even though Einstein did realize, in 1936, the possibility of a star acting as a gravitational lens for the light coming from another star in the background, he did not think that the technological capabilities at that time made it possible to observe such a phenomenon (cf.[3, 6, 8]). But, a year after, Zwicky proposed that it would be more probable to observe gravitational lensing if the objects in question were galaxies, or galaxy clusters, and that it would be possible to use this to estimate the amount of DM and map its distribution within the lens structure (cf.[6, 8]). More than forty years later, Walsh, Carswell, and Weymann discovered the first gravitational lens; and it turned out that Zwicky was right (cf.[6]). Since then, our knowledge of the field has rapidly expanded, and many more gravitational lenses were detected.

When a light ray bends due to a gravitational lens, it curves with a soft angle. However, if the size of the gravitational lens is much smaller than both the distance between the observer and the lens and the distance between the lens and the light source, the *thin-lens approximation* can be applied; and the light path can be assumed to compose of two straight lines (cf.[5]). In this case, the deflection angle, α_D, due to a point mass, M, is given by (cf.[10])

$$\alpha_D(x) = \frac{4GM}{xc^2}, \tag{1.3.1}$$

where x is the distance of closest approach of the light ray to the gravitational lens, and c is the speed of light. This point-mass approximation can also give acceptable estimates in cases of extended lenses. For a circular mass distribution, (1.3.1) can be written as (cf.[5])

$$\alpha_D(R) = \frac{4G}{c^2}\frac{M(R)}{R}, \tag{1.3.2}$$

where $M(R)$ is the mass enclosed within the radius R.

The *lens equation* governs the relation between the deflection angle, α_D, the observer-source angular-diameter distance, D_{OS}, and the lens-source angle-diameter distance, D_{LS}; where the angular-diameter distance is the distance measure in Our Non-Euclidean Universe (cf.[5, 8]).

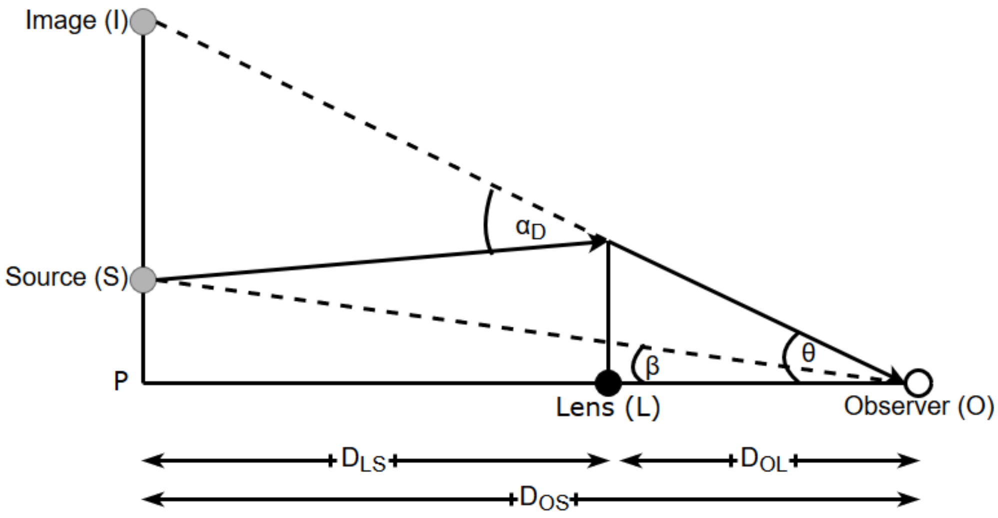

Figure 1.4: Lensing configuration

Figure 1.4 shows that

$$PI = PS + SI, \tag{1.3.3}$$

and it follows from (1.3.3), when β, θ, and α_D are all small angles, that

$$D_{OS}\theta = D_{OS}\beta + D_{LS}\alpha_D, \tag{1.3.4}$$

where θ and β are the angular positions of the image and the source, respectively, with respect to the observer. If we define a scaled deflection angle, α, as

$$\alpha = \frac{D_{LS}}{D_{OS}}\alpha_D, \tag{1.3.5}$$

we can write (1.3.4) as

$$\theta = \beta + \alpha. \tag{1.3.6}$$

In the case of a circular mass distribution, the above lens equation might have multiple solutions; and thus multiple images can be created for the same source (cf.[5, 8]).

When the background source is an extended object, the images produced are arcs known as *Einstein rings* (cf.[5, 8, 10]). In a perfect situation where the observer, the lens, and the source are in complete alignment, those rings form a perfect circle the radius of which is called *Einstein radius* (cf.[6]). When a gravitational lens produces multiple images that are discernible by the observer, the phenomenon is called *strong lensing*; and in that case the mass can be estimated from the angular size of the arcs using the lens equation. But when the mass of the lens is relatively small and the light source is fairly aligned with the lens, the multiple images are unresolved, and a single brighter image of the source is seen by the observer. This is called *microlensing* (cf.[6, 8]). Another type of lensing is *weak lensing*, where one distorted image is detected. In this case, the lens properties can only be investigated through statistical studies of the lens effect on many background sources. However, this is particularly useful, not only in estimating the lens mass, but also in mapping the matter distribution within the lens—whether luminous or dark (cf.[5, 6, 10]).

Gravitational lensing is one of the most convenient tools for tracking the distribution of DM through the structure of the Universe. Estimating the mass of a lens is straight-forward when the geometry is known, without the need to apply any theoretical models (cf.[6, 10]). Lensing effects have even been observed without any apparent mass to cause it, which—if the observations are valid—are indicative of a non-luminous (dark) lens (cf.[5]). At this point, lensing observations have already shown that galaxy clusters contain as much as 50 times more DM than luminous matter; and that, in many cases, the DM is more concentrated (cf.[2]).

Bullet Cluster

The most outstanding proof of DM so far has been obtained by use of the weak and strong gravitational lensing phenomena. It was the result of the cluster 1E0657-56; or what is known as the *Bullet Cluster* (cf.[5, 10]). It represents the "smoking gun" for the existence of DM. The *Bullet Cluster* is the result of the collision of two giant galaxy clusters, one larger than the other. Each of these clusters consisted of luminous matter, in the form of galaxies and X-ray-emitting gas, and DM. The collision caused the smaller cluster to pass through the larger one, like a "bullet" (cf.[5]).

Lensing observations, along with optical and X-ray observations, show that while the impact of the collision displaced the luminous matter from the DM halos, and slowed it down, the DM halos themselves passed through each other unaffected by the collision (cf.[5, 10]), as shown in Figure 1.5. This implies that DM is naturally collisionless. This conclusion was again confirmed by the more recent event for the cluster MACS J0025.4-1222 (cf.[5, 10]).

1.4 The Cosmic Web

When an electron in a hydrogen atom moves from an excited state to the ground state, the energy lost is emitted in the form of an emission line. Such lines are referred to as *Lyman-Alpha lines* (cf.[5]). Reversely, when a neutral hydrogen atom absorbs energy from an electromagnetic wave such that an electron is excited from the ground state to a higher one, the wavelength of the energy absorbed by the hydrogen atom will manifest as an absorption line in the spectrum of the electromagnetic wave. When this happens in the intergalactic medium, the series of the absorption

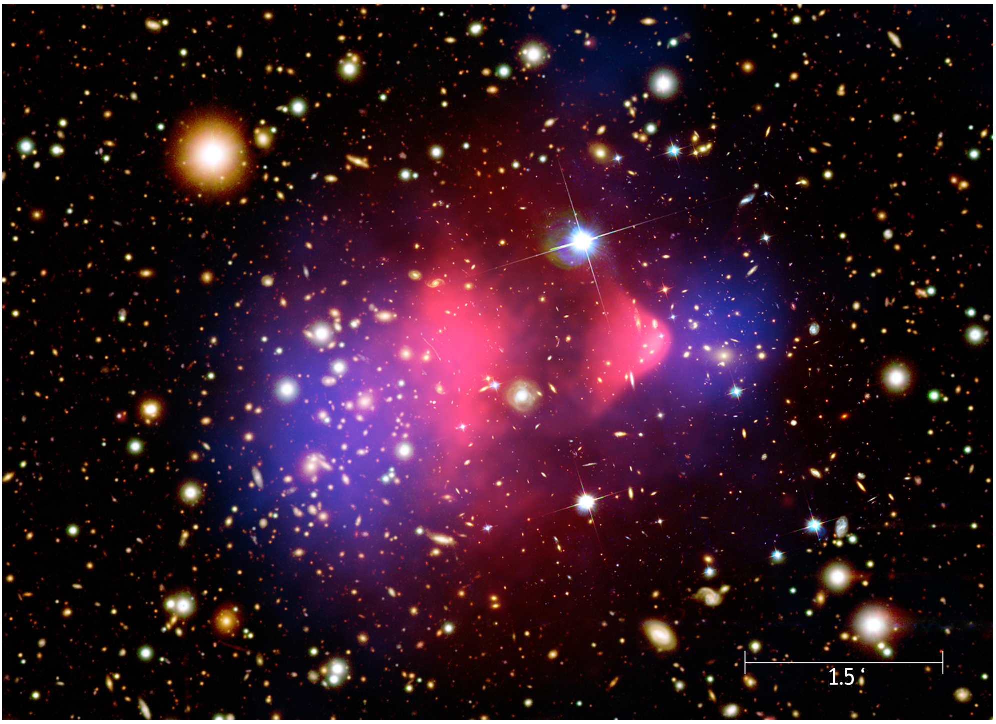

Figure 1.5: X-ray image (*pink*) of the X-ray-emitting gas in both clusters, superimposed over a visible light image of the member galaxies, with DM distribution calculated from gravitational lensing (*blue*). (*©NASA/CXC/M. Weiss*)

lines resulting from the excitation of the neutral hydrogen atoms is called the *Lyman-Alpha forest* (cf.[2, 5, 8]).

Quasars (or quasi-stellar objects) are active galactic nuclei located at very high redshifts. Their energy spectrum includes visible and radio waves. While the electromagnetic radiation of quasars passes through the intergalactic medium, the neutral hydrogen in that medium absorbs the relative energies giving rise to the Lyman-Alpha forest, which has been observed in the spectra of distant quasars (cf.[5]). Because of the expansion of the Universe, the wavelengths absorbed by the neutral hydrogen would be stretched to longer wavelengths. Thus, the magnitude by which these Lyman-Alpha absorption lines are stretched can be used by an observer to trace the times and sites of absorption; and, hence, the distribution of neutral hydrogen in the intergalactic medium (cf.[5]).

Since galaxies can only be used to trace matter (or DM) distribution in the Universe to the extent of obtaining an estimate, the Lyman-Alpha forest has been crucial in tracing the finer structures throughout the Universe (cf.[2, 5, 8]). Observations of the Lyman-Alpha forest indicate that the gas in the intergalactic medium is arranged in sheets and filaments, which have been dubbed the "*Cosmic Web*" (cf.[5]). These observations suggest the existence of some relatively-small concentrations of DM that trap these structures of luminous matter around them without forming a stable configuration (cf.[5]). Hence, the Cosmic Web can also be used to trace DM.

1.5 Discussion

In this Chapter, we have reviewed the various accumulating pieces of evidence that strongly suggest the existence of an unknown component of matter in Our Universe. We have also seen that some observations can provide us with clues to the nature of DM. Now, a few points to note are:

- The evidence on the existence of a DM component in Our Universe—and even in Our Milky Way—has been piling for more that eight decades now. Even though a lot of debate is still going on about the nature of DM (as will be discussed in Chapter 3), the existence of an exotic component; namely, DM, has long been accepted as a fact. Its contribution to the energy budget of the Universe has even been measured to be more than 26% of the whole energy-matter content.

- All the evidence of DM seems to be gravitational. This can be both a challenge and an advantage. While most theories about DM candidates stem from a particle physics view, it seems that gravity is the dominant field that governs the interactions of this unknown matter component. However, if we were to succeed in deciphering DM, we could open a gateway to a successful theory that finally unify gravity with the rest of the forces of nature, which will be briefly reviewed in Chapter 2.

- Electromagnetic observations proved insufficient when pursuing DM. It may thus be advisable to apply other methods of investigation. Some such methods are already being pursued (as will be discussed in Chapter 4). However, creative experimental and theoretical approaches can be crucial to help us reach an answer quicker.

- None of the evidence can yet tell us what exactly is the identity of DM. We still do not know what causes it to react differently than ordinary matter. It could be normal particles in exotic structures, or exotic particle species we have not encountered before. It could even be a special manifestation of the duality of matter. All these avenues are still open for further investigation.

- Notwithstanding the scarce information that DM evidence can tell us about its nature, it is clear that it does not interact electromagnetically; and that it is collisionless as has been demonstrated by the analyses of the Bullet Cluster and the MACS J0025.4-1222 events.

Even though the evidence of DM is macroscopic in scale, both theoretical models of DM and the experimental search for it involve a lot of particle physics, which is mainly microscopic in scale. Thus, to be able to explore all aspects of DM, one needs a working knowledge of particle physics and its currently-standing theory, *i.e.* the Standard Model (SM) . With that purpose in mind, the next Chapter will briefly review the fundamentals of the SM, starting with an account of the elementary particles that constitutes all matter in the Universe, then moving to the interactions that occur between these particles, and finally to the theoretical models that govern these interactions.

Chapter 2

Basics of Particle Physics

2.1 Fundamental Particles

Elementary (or fundamental) particles are those that are not made up of smaller particles However, *elementarity* is a theoretical concept that can never, in principle, be proven experimentally. Our view of fundamental particles is always limited by the energy scale we can currently investigate (cf.[11]). In this Section, an account of the currently known elementary particles is given, to lay the groundwork for reviewing the SM.

Fundamental particles are categorized into two main classes: matter particles and field particles (cf.[11]). Matter particles are what constitutes all the objects in the Universe whereas field particles are simply representatives of the fields of the forces of interactions between matter particles, which will be further discussed in §2.2. Matter particles are referred to as *fermions* while field particles are referred to as *bosons* (cf.[12–14]). Each of these classes obey a different spin-statistics theorem. While fermions obey Fermi-Dirac statistics, bosons obey Bose-Einstein statistics (hence the names) (cf.[11]). The most significant differences between fermions and bosons are that: First, while fermions obey the Pauli exclusion principle, which states that no two particles can occupy the same quantum state, bosons do not; and second, fermions have half-integer spins while bosons have integer spins (cf.[11, 15]).

Fermions are categorized into *quarks* and *leptons*. There are currently six known quarks and six known leptons (cf.[11–15]). Each category is usually divided into three *generations*. Generations have two particles each, and have similar properties but increasing masses (cf.[11]). Each of the quarks and leptons is also associated with a *flavor*, which is specified by what are referred to as *flavor quantum numbers* (cf.[12, 13]).

There are three charged leptons: the electron (e^-), the muon (μ^-), and the tau (τ^-), and three neutral ones called neutrinos: ν_e, ν_μ, and ν_τ. Charged leptons carry a charge of -1; and each neutrino is associated with one of the charged leptons. The six known quarks are: up (u), down (d), charm (c), strange (s), top (t), and bottom (b) (cf.[14, 15]). They all have fractional charges of $+\frac{2}{3}$ for u, c, and t, and $-\frac{1}{3}$ for d, s, and b (cf.[11, 15]). Quarks also have an additional charge called *color charge*. It can take the values: red, green, or blue (cf.[12, 14]). The significance of this charge will be more clear in §2.2. Table 2.1 summarizes all known fermions and their properties.

As for elementary bosons, they are the mediators of interactions between fermions. There are the gauge bosons: eight gluons, the W and Z bosons, the photon, and the graviton, in addition to the *Higgs boson* (cf.[11, 12, 15]). Each boson mediates a specific field of interaction, which will be further discussed in §2.2. The properties of elementary bosons are shown in Table 2.2.

Each particle has an antiparticle that has the same mass but opposite charge and quantum numbers, except for some particles (*e.g.* the photon) that are their own antiparticles (cf.[11, 12]). The first antiparticle to be observed was the *positron*, the antiparticle of the electron. It was discovered by Anderson in 1932 (cf.[15]). Only a year before that, the existence of the positron was hinted at by Dirac when a wave equation produced four solutions: two describing the electron, and the other two describing a particle identical to it but with an opposite electric charge, *i.e.* the positron (cf.[15]). Antiparticles are usually denoted by a bar on top to distinguish them from their counter-particles. For instance, a particle P will have an antiparticle $\bar{P}$.

Table 2.1: Properties of elementary fermions. Data obtained from the Review of Particle Physics by the Particle Data Group (PDG)[16].

Elementary Fermions						
Property	**1st generation**		**2nd generation**		**3rd generation**	
	Quarks					
	Up	Down	Charm	Strange	Top	Bottom
Symbol	u	d	c	s	t	b
Mass [MeV/c^2]	2.16	4.67	1270	93	4180	172900
Charge [e]	$+2/3$	$-1/3$	$+2/3$	$-1/3$	$+2/3$	$-1/3$
Spin	1/2	1/2	1/2	1/2	1/2	1/2
	Leptons					
	Electron	Electron neutrino	Muon	Muon neutrino	Tau	Tau neutrino
Symbol	e^-	ν_e	μ^-	ν_μ	τ^-	ν_τ
Mass [MeV/c^2]	~ 0.51	< 0.002	~ 106	< 0.19	~ 1777	< 18.2
Charge [e]	-1	0	-1	0	-1	0
Spin	1/2	1/2	1/2	1/2	1/2	1/2

Table 2.2: Properties of elementary bosons, as obtained from [16].

Boson	Symbol	Mass [GeV/c^2]	Charge [e]	Spin
Photon	γ	0	0	1
Gluon	g	0	0	1
Graviton[1]	G	$< 6 \times 10^{-38}$	0	2
W boson	W	80.379	±1	1
Z boson	Z	91.1876	0	1
Higgs boson	H	125.10	0	0

[1] Hypothetical

While leptons can be found free in nature, quarks always exist within a structure as far as is experimentally proven. Quarks bond to constitute particles named *hadrons* (cf.[13]). There are two classes of hadrons: *baryons* and *mesons*. Baryons are composed of three quarks or anti-quarks. For example, the proton is composed of two up quarks and one down quark while the neutron is made up of one up quark and two down quarks. A meson, on the other hand, consists of a quark and an anti-quark (cf.[12, 13, 15]). For example, the pion (π^+) consists of an up quark (u) and a down anti-quark ($\bar{d}$).

Leptons are associated with a lepton number, which is conserved in interactions. Baryons are also associated with a baryon number, also conserved. Quarks have a fractional baryon number of $+\frac{1}{3}$ (cf.[12, 14]).

The majority of matter content in the Universe is composed of up and down quarks—which make up the nucleons: protons and neutrons—along with electrons and their associated neutrinos. More massive particles are only observed in particle-physics laboratories or energetic structures like supernovae and cosmic showers. It is believed that the more massive particles were of more significance at the early stages of the evolution of the Universe (cf.[11, 12, 15]).

2.2 Four Forces of Nature

There are currently four forces of interaction that are known: the strong force, the weak force, the electromagnetic force, and the gravitational force (cf.[13, 14, 17]). However, there is no reason to believe that has always been the case. In fact, theorists believe that these four interactions might have once been a single interaction at the beginning (*i.e.* early stages) of the Universe; and that the separation occurred as the Universe cooled down (cf.[11]). The strength of each interaction depends on the energy (cf.[13]). Each of the four forces has a theory that governs it. Furthermore, the electromagnetic and weak interactions have been unified by the *electroweak theory* (cf.[12]). There are currently a lot of efforts employed to the unification of the four forces of interaction in one theory; there are even many *Grand Unified Theories* (GUTs) already developed that unify the strong, weak, and electromagnetic interactions into one force (cf.[12]).

The gravitational force acts on any two bodies at any distance from each other—thus, it has an infinite range. Gravity dominates on a macroscopic scale. The currently-standing theory of gravity is the *General Theory of Relativity* (cf.[11, 12, 14]), which was formulated by A. Einstein and has been established through proven predictions. Even though GR has been contradicted by observations in some points (*e.g.* the accelerating expansion of the Universe), a more successful theory is yet to be found. The gravitational interaction is hypothesized to be mediated by the *graviton*, which remains a hypothetical particle (cf.[11]).

The electromagnetic force acts on any two electrically-charged particles. It also has an infinite range. Electromagnetism is governed by quantum electrodynamics (QED) which has been merged into the electroweak theory (cf.[12]). The electromagnetic interaction is mediated via the exchange of photons(cf.[14, 17]).

The gravitational and electromagnetic interactions were the first to be discovered. However, there remained the question of what held the nucleus together. Why is the nucleus not affected by the electric repulsion? There must be a '*nuclear force*' much stronger than the electromagnetic one, even if it was shorter in range (cf.[17]). Another puzzle was how the

Table 2.3: The four fundamental forces (cf.[12, 13]).

Interaction	Relative strength	Range $[m]$	Virtual particles	Theory
Gravitation	10^{-39}	∞	Graviton	GR
Electromagnetism	1/137	∞	Photon	QED
Weak	10^{-6}	10^{-18}	$W^{\pm}$, Z	Electroweak
Strong	1	10^{-15}	Gluons	QCD

neutron produced a proton and an electron in a β-decay.

It was later discovered that there are—not one, but two—additional forces that act within the nucleus. One of them is the weak force, which acts on all matter particles according to certain rules (cf.[11, 12, 17]). It is responsible for the β-decay, and is, consequently, responsible for the production of energy in the Sun. The weak interaction is clearly very short-ranged (see Table 2.3), and is governed by the electroweak theory. The $W^{\pm}$ and Z bosons mediate the weak interactions; and due to their mass, it is less likely for them to be emitted. In fact, this is the reason of the short range (or 'weakness') of the interaction, not the lack of intrinsic strength (cf.[14]).

The strong force acts on quarks, and it is what holds them bound together into hadrons, and the hadrons into nuclei (cf.[14]). The strong force is governed by quantum chromodynamics (QCD). The force between quarks is mediated by the exchange of gluons (cf.[13]). Quarks and gluons have a color charge; and it can be red, green, or blue. But it is not related to actual colors of course. Just like electrically-charged atoms bond to form electrically-neutral molecules, colorfully-charged quarks bond to form colorless hadrons through the strong interactions (cf.[12]). The strong force is also color invariant. An interesting feature of the strong force is the coupling strength, which tends to zero when the distance between the affected particles does. This gives rise to what is called *asymptotic freedom* (cf.[14]), which essentially means that the quarks and gluons act as free particles as long as they are inside a hadron. However, the coupling strength increases dramatically if the particles are pulled apart, which is known as *color confinement*. This is what led to the popular conclusion that quarks can never be found free outside hadrons.

If we consider these four interactions collectively, several recurring features can be compared. The first feature is the relative strength of each interaction. Ordered from the strongest to the least strong, they are: strong interactions, electromagnetic interactions, weak interactions, and gravitational interactions (cf.[11, 17]). As for the range of interactions, they can be ordered from the shortest to the longest as: strong, then weak interactions; whereas both electromagnetic and gravitational interactions have infinite ranges (cf.[13]). Consequently, both strong and weak interactions dominate at small scales while not being important at large scales. In spite of the electromagnetic and gravitational interactions both having infinite range, gravity is less strong; thus, it is only dominant on large scales. However, since electromagnetism depends on the charge, it is more important on small, molecular scales, but, taking into account that the Universe is electrically neutral, electromagnetism becomes negligible on large scales (cf.[11, 14]).

Another feature we can compare is the virtual particles involved in each interaction, where, by virtual, we mean transient, or a particle that is exchanged between two particles to mediate their interaction. Virtual particles are bosons. We have the graviton (hypothesized) for the gravitational interaction, the photon for the electromagnetic interaction, the

$W^{\pm}$ and Z bosons for the weak interaction, and the gluons for the strong interaction (cf.[12, 17]). These particles can also be considered as the quanta exchanged during the interactions.

A convenient way to know if a particle is affected by one of the four forces, is to consider the four corresponding charges of the particle. The mass can be considered to be the gravitational charge. The electrical (positive or negative) charge is associated with electromagnetism. The spin is considered as the weak charge; and finally,the color charge (red, green, or blue) is associated with the strong interaction (cf.[11]). In particle physics, interactions are visually represented by what is known as *Feynman diagrams*, where real and virtual particles are differentiated by the shapes of their trajectories (cf.[17]).

2.3 The Standard Model

The SM is often considered the most successful theory formulated by the human race. Essentially, it is a theory that outlines the set of particles that make up the Universe, along with the rules that govern the interactions between these particles (cf. [11, 17–20]). In terms of theories, the SM is the result of merging the electroweak theory, which governs both the electromagnetic and weak interactions, and QCD, which governs the strong force.

In mathematical terms, a field theory is defined by its *Lagrangian function*, or simply, the *Lagrangian*. The Lagrangian is a function of the kinetic and potential energies of the system, which are in turn functions of the generalized coordinates of the system, and their derivatives. By applying the least-action principle on a Lagrangian function, the field equations of the theory are deduced (cf.[18]). The SM belongs to what are known as *gauge theories*. These are theories of which the Lagrangian is invariant under certain symmetry groups (cf.[11–13]). So far, there is no gauge theories that successfully describe the gravitational interaction; and consequently, the SM does not apply to gravity.

The gauge bosons result from the gauge invariances of the Lagrangian. In the 1960s, Glashow, Weinberg, and Salam unified both the electromagnetic interaction and the weak interaction into the electroweak force. This force, governed by the electroweak theory, had four gauge bosons. However, these four bosons were still all massless; that is, their masses were equal to zero. Any attempt to add a term to the Lagrangian in order for the bosons to acquire masses, would result in breaking the invariance (cf.[19]). Hence, Weinberg and Salam implemented the *Higgs mechanism* developed in 1964, based on spontaneous symmetry breaking (cf.[11, 12]). The Higgs mechanism is responsible for giving gauge bosons—and even fermions—their masses. With this piece of the puzzle, the electroweak theory was complete.

The Higgs mechanism results in a scalar field, which has been predicted to be the mathematical manifestation of an additional boson; that is, the *Higgs boson* (cf.[18, 19]). In 2012, the Higgs boson was experimentally discovered by the ATLAS and CMS collaborations[21, 22]. The discovery of the Higgs boson validated the Higgs mechanism beyond a doubt, and further established the SM. Thus, the final Lagrangian of the SM is composed of the electroweak Lagrangian—including the Higgs terms—and the QCD Lagrangian (cf.[11]).

The SM currently represents the best theory that describes the physics of Our Universe at a subatomic level. However, the picture is not yet complete. The SM still does not include gravity, which is necessary for understanding the Universe on a macroscopic scale. This becomes clear when we consider many of the yet-to-be-solved mysteries of the Universe, from DM to the matter-antimatter asymmetry and the accelerating expansion of the Universe (cf.[13, 17, 19]). There still is a lot of work to be done to reach a version of the SM that explains all our observations of the Universe. This is the reason why so many efforts are being aimed to understand what is called the physics beyond the SM (BSM) (cf.[12]). A more in-depth account of the SM development, successes, failures, and expectations, can be found in [11, 12, 23–25].

2.4 Discussion

In this Chapter, a brief account has been given of the elementary particles that make up the Universe and how they mediate and are governed by the four fundamental forces of nature; along with the theories that govern each of these forces. In particular, we have seen how the SM has unified three of them. However, some points worth noting are:

- Since the concept of *elementarity* is used to refer to particles that cannot be broken down to smaller components, this concept will always remain a conventional assumption. Our classification of particles as elementary or non-elementary will always be determined by the capabilities of available technology. As observational techniques become more advanced, we can detect finer structures. There was a time when the “atom” was an elementary particle; now there is a plethora of elementary particles. In this regard, we can not tell what the future might still reveal.

- Although four forces of nature are recognized, many scientists believe that these four forces all stem from one single force, and that the separation only occurred at the later stages of the evolution of Our Universe. Perhaps this elegant idea has always been the motivation behind all the efforts devoted to unifying the four forces. The more we know about the most exotic components of the Universe, the more pieces of the puzzle we will have in order to build a more-complete picture of how these forces relate to one another.

- At this point, three of the fundamental forces have been unified by one theory, *i.e.* the SM. However, gravity remains stubbornly out of reach of any unification attempts. It has even been a lifelong dream of Einstein to unify gravity with electromagnetism within a geometric field theory. Nevertheless, he could not achieve it. The identification of the strong and weak forces has complicated the task further. The discrete (quantized) nature of the SM contrasts with the pure continuity of gravity. Our best hope would be identifying the continuity elements of the discrete forces and the discreteness elements of the continuous forces, which might even comprise another form of nature duality. Studying components like DM are definitely a crucial tool in this pursuit of a one theory to rule them all.

- As discussed in the previous section, despite the many successes of the SM, it still cannot explain many phenomena in the Universe. Some of them are those manifested by DM. Thus, pursuing the identity of DM could lead to the key to physics BSM. There is no lack of theories that try to interpret DM with as little deviation as possible from the SM principles. Several approaches can as well be applied toward proving or disproving these theories.

As already mentioned, the identity of DM is yet to be known. However, in the next Chapter, we will review how different candidates of DM are classified. In addition, we will give an account of each of the DM candidates that are most considered in theoretical models. Even though those models are not limited to these candidates and include many other suggested ones, the account below will draw a comprehensive picture of the potential properties that are to be expected from different candidates, and the observational manifestations of such properties.

Chapter 3

Types and Candidates of Dark Matter

3.1 Types of Dark Matter

There are several properties that can be used to classify DM particles: the mechanisms of particle production, the nature of the particle components themselves, which determines the model obeyed by the particles, or the mass range of the candidate particles. In what follows, each of these properties are briefly considered.

Production

On one hand, DM particles can theoretically be produced either thermally or non-thermally—via other mechanisms. Thermal DM particles were produced in the early stages of the Universe as pairs of particles and antiparticles through the collision of plasma at a high cosmic temperature. It is hypothesized that these DM pairs would then annihilate each other and produce SM particles. Eventually, due to the expansion of the Universe, the annihilation rate would fall until it is below the expansion rate of the Universe. From that point forward, the comoving number density of such particles would become constant. This is called the “freeze out” of the particle species, and after that point the remaining particles are considered relics of the Big Bang nucleosynthesis (cf.[2, 5]). Weakly Interacting Massive Particles (WIMPs) are a potential candidate for such production mechanism. On the other hand, non-Thermal DM particles could have been produced gravitationally due to the expansion of the Universe. In such case, some of the candidates would be WIMPZILLAs, winos, and axions.

Particle Nature

DM particles can either be baryonic—that is, obey the SM—or non-baryonic of an unknown nature. Based on the Big Bang model of the beginning of the Universe, a bound of baryonic density has been obtained based on the abundances of the primordial nuclei. That boundary is estimated to be (cf.[26])

$$\Omega_{\text{bar}} = 0.028 \pm 0.012. \tag{3.1.1}$$

However, another estimate can be obtained from the luminous mass observed in the Universe. That estimate is[27]

$$\Omega_{\text{lum}} = 0.0036 \pm 0.0020. \tag{3.1.2}$$

This discrepancy between the baryonic density and the luminosity density suggests that there is a missing baryonic component. In other words, some baryons are not luminous, *i.e.* dark baryons (cf.[28]). The most potential candidates for that type of DM are MAssive Compact Halo Objects (MACHOs) or Primordial Black Holes (PBHs) (cf.[5, 26]), which will be discussed in §3.2.1.

Even though baryonic DM is needed to account for the rest of the baryonic density in the Universe, it is not enough to make up the the rest of the matter content in the Universe, which is estimated to be approximately six times the baryonic matter (cf.[28]). Another reason why baryonic DM is only one type of DM is that no baryonic candidate can explain the early density fluctuations which were the seeds of structure formation in the Universe. These fluctuations have been interpreted from observations of the Cosmic Microwave Background Radiation (CMBR)[29, 30]. Thus, non-baryonic DM is thought to make up most of the DM in the Universe. Such particles are assumed to have extremely-weak interactions with baryonic matter; and, hence, cannot be detected with conventional methods. Despite the development of many models constraining the properties of non-baryonic DM particles, the true nature of these particles is still a mystery. The only fact about non-baryonic DM particles at this point is that they are relics of the Big Bang (cf.[2, 5]). This would suggest large masses for these particles in order to be consistent with the DM relic density of the Universe. WIMPs are the most potential candidates for non-baryonic DM particles.

Mass and Speed

DM candidates can also be classified based upon their masses. These masses determine the speed of the particles at their freeze-out temperature during the early stages of the Universe. On one hand, Hot Dark Matter (HDM) particles moving with relativistic speeds have light masses. Neutrinos are the main candidate for HDM particles (cf.[26]). On the other hand, Cold Dark Matter (CDM) move with non-relativistic speeds and have heavy masses (cf.[28]). An intermediate type between HDM and CDM is called Warm Dark Matter (WDM). Its most probable candidate is sterile neutrinos (cf.[5]), which will be discussed in §3.2.4.

3.2 Candidates of Dark Matter

There is a multitude of candidates for DM particles. Some of them are more supported by theory than others; and some candidates fit the observational constraints better. In this Section, each of the most theoretically-considered candidates is briefly reviewed.

3.2.1 MACHOs

MACHOs are the most likely candidates for baryonic DM. They are supposed to be massive concentrations of dark baryons that float in galaxies without belonging to any stellar system. Naturally, they have no electromagnetic radiation even though they are supposedly composed of normal baryons (although not always). There are several sub-candidates that could constitute the bulk of MACHOs, ranging from black holes and neutron stars to brown dwarfs and untethered planets (cf.[6, 31]).

Although these objects cannot be observed using telescopes, they can be detected and studied via observations of microlensing events. When a MACHO passes in front of a luminous celestial object, the brightness of that object transiently increases due to the MACHO acting as a gravitational lens. Of course the magnitude of the observed lensing effect would depend on several variables such as the lens mass and distance (cf.[6]). In 1986, theoretician Bohdan Paczynski developed a new analysis procedure for such microlensing events[32], which made astronomers ready to take it to the next observational step.

Even though the theoretical foundation had been established, there were still some observational risks to be taken into account. One technical problem was that variable stars naturally change in brightness without any lensing effects. So, how could a microlensing event be distinguished from a variable star? Due to the physical properties of a star, the brightness of a variable star changes differently at different wavelengths of light. Also, eclipsing binary systems change brightness periodically. However, a gravitational lens would cause the brightness of a background star to change similarly at all wavelengths, and the *lightcurve* would appear symmetric before and after the brightness peak. Thus, the answer to that problem was to observe the incoming light in two colors and compare the lightcurve at both wavelengths (cf.[6]). Another problem was the unlikeliness of a MACHO aligning with a background star, along with the short event duration—expected to be less than a day—which required more-frequent observations. Luckily, these problems did not discourage astronomers to pursue MACHOs. A ($2,000 \times 2,000$-pixel) CCD camera, able to simultaneously image $500,000$ stars, was developed particularly for that purpose. Less than a decade after Paczynski's paper, the MACHO project was born[33].

The MACHO collaboration monitored microlensing events in the Large Magellanic Cloud (LMC) and the central bulge of the Milky Way for seven years starting in 1992 (cf.[6, 34]). After less than a year of observations, the MACHO collaboration led by Charles Alcock announced the first detection of a definite microlensing event with a magnification factor of seven[35]. The lightcurve of the event is shown in Figure 3.1. Many other microlensing events were detected after that first event.

After the MACHO project ended, the collaboration concluded that the MACHOs masses range from 0.15 $M_\odot$ to 0.9 $M_\odot$, where $M_\odot$ denotes the solar mass, and that the total mass in MACHOs—which was found to be $9^{+4}_{-3} \times 10^{10}$ $M_\odot$ out to 50 kpc—represents about 20% of the mass of the galactic halo of Our Milky Way [36]. However, theoretical models include MACHOs of masses ranging from 10^{-16} $M_\odot$ to 1 $M_\odot$ (cf.[31]). Still, some astronomers are worried that the microlensing events detected by the MACHO collaboration are not of DM objects, but simply of stars

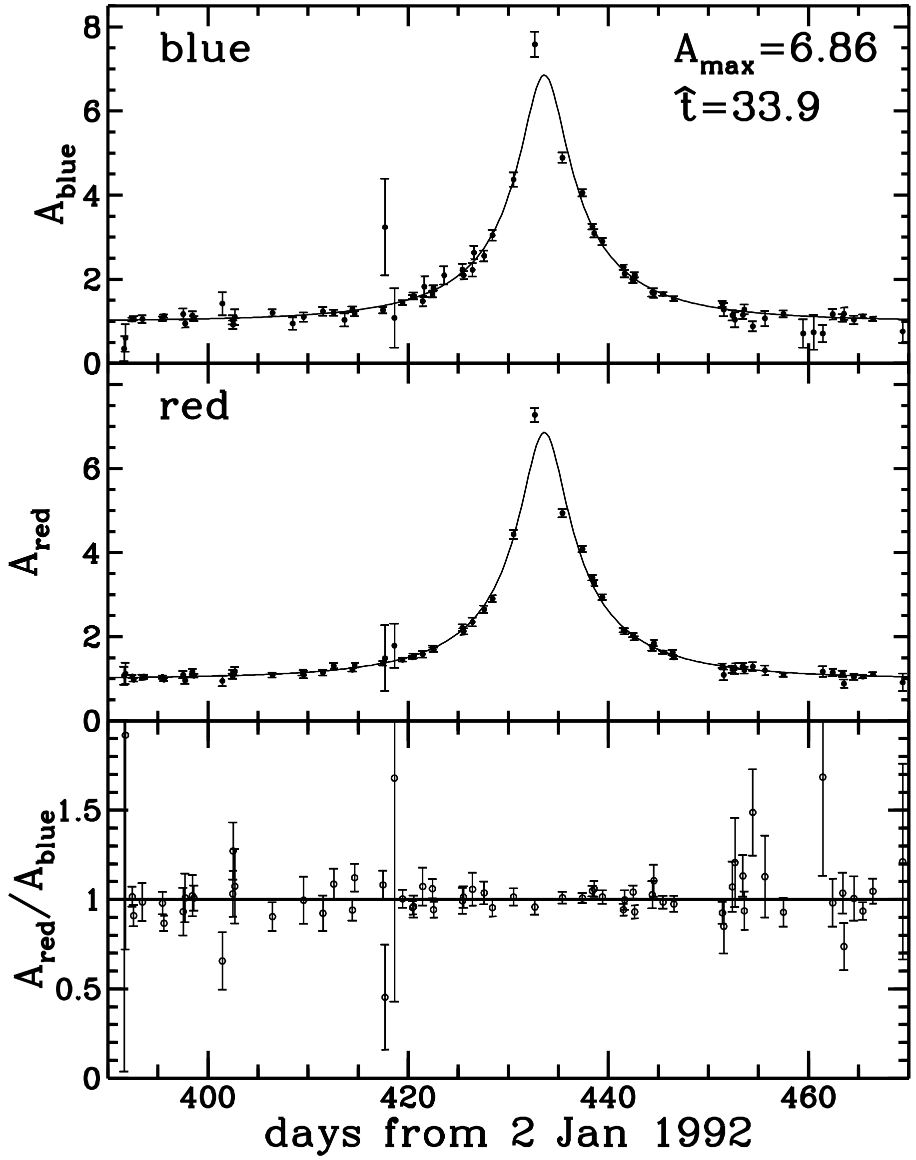

Figure 3.1: A theoretical microlensing model fitted simultaneously to the blue (*top panel*) and red (*middle panel*) lightcurves of the first event detected by the MACHO collaboration; and the ratio of red to blue flux of the event (*bottom panel*) normalized to a median of unity[35].

microlensing each other due to the non-flat layout of the LMC. However, that is not the common view (cf.[6]). Nevertheless, other searches for MACHOs and other DM objects with microlensing phenomena have been carried out. Among them are the EROS Experiment that operated from 1990 to 2003[37], and the OGLE project that started in 1992 and is still operating[38, 39]. Observational results have not yet contradicted the above limits reached by the MACHO project.

PBHs

In general, Black Holes (BHs) are known to be regions with very strong gravitational fields that no particles—not even light, *i.e.* photons—can escape. Thus, it follows that they cannot be observed via electromagnetic telescopes. However, there are several differences between "ordinary" BH and PBHs, which we are about to discuss. While ordinary BHs are known to be corpses of massive stars that have gravitationally collapsed, PBHs are supposed to be the product of density perturbations in the early Universe. Moreover, while ordinary BHs have been established as existing astronomical objects[40], the existence of PBHs remains hypothetical. Perhaps, for our purposes, the most important difference between the two is that while ordinary BHs are made up of baryonic particles—since they are the remnants of once-luminous stars—PBHs are assumed to have formed during the radiation era before the Big Bang nucleosynthesis had begun. Thus, they are classified as non-baryonic, and can, consequently, make up the huge DM budget in the Universe without being limited by the 5% baryonic content (cf.[26]).

PBHs can be considered the most-investigated candidate of MACHOs (cf.[41]). There have been many models describing their possible formation mechanisms, such as early density perturbations[42], cosmic phase transitions[43], a double-inflation Universe[44, 45], or even collapse of closed cosmic strings[46]. They were first suggested as DM candidates in 1966 by Zeldovich and Novikov[47], and in 1971 by Hawking[42], who later, in 1974, identified the process known as *Hawking evaporation*[48]. This process is not exclusive to PBHs, but happens in the near vicinity of any BH. Quantum fluctuations near the event horizon of any BH produce SM-particles that move outward from the BH, such that it seems that the BH itself is emitting some radiation. However, the flux of particles produced due to this process has a rate that is inversely proportional with the square of the BH mass. Thus, the rate is very low for ordinary BHs that have extremely large masses, so they essentially appear as non-radiative as they are known to be, while PBHs have higher flux rates since their masses are known to be of the stellar order (cf.[26, 49]).

The Hawking evaporation process had a significant impact on the study of PBHs. Firstly, a reasonable conclusion has been that the evaporation process would produce an inevitable signature in the extragalactic background, which can be detected[50, 51]. Secondly, it was concluded that any currently-existing PBHs must have masses larger than 10^{15} g, since any PBHs with smaller masses would have evaporated during the age of the Universe (cf.[49, 52]). Even though there is no definite experimental evidence of the existence of PBHs, there is still a lot if interest in studying them (cf.[49, 53, 54]). Not only can PBHs be a probe of the cosmological expansion and the early Universe[55], but the evaporation mechanism can also be examined to derive constraints on the properties of BHs[56, 57].

Studies of PBHs vary between phenomenological models (cf.[41] and references within) and observational studies. The latter mainly depend on two premises: first, that PBHs would act as gravitational lenses similar to other MACHOs candidates; and second, that particles arising via Hawking evaporation of PBHs would leave an astrophysical signature in cosmic rays (CRs) which can be traced (cf.[26, 52]). Several constraints have been identified using observational techniques based on these premises, in addition to other large-structure observations and cosmological models (cf.[49, 53, 58]). These have been analyzed and combined in Reference [49]. Figure 3.2 summarizes these constraints, where $f(M) \equiv \dfrac{\Omega_{\mathrm{PBH}}}{\Omega_{\mathrm{CDM}}}$ is the ratio of the current density parameter of PBHs, Ω_{PBH}, to the current density parameter of CDM, Ω_{CDM}. Results from space experiments and other phenomenological studies are continuously updating these constraints. However, PBHs have not yet been definitely established or excluded as DM candidates.

3.2.2 SM Neutrinos

The existence of neutrinos was first postulated by Pauli in 1930 to explain the conservation of energy, momentum, and angular momentum in beta decay. In 1956, the neutrino was experimentally detected for the first time[59]. Neutrinos are considered to be the first and most popular candidates of HDM (cf.[5, 60, 61]). Neutrinos are extremely non-interactive. A neutrino can pass through the Earth without colliding with a single other particle. Moreover, neutrinos are highly abundant. These two reasons made neutrinos likely DM candidates. But their popularity as candidates is the result of their having masses, which means they can interact gravitationally; and at first these masses were not established as part of the SM (cf.[2, 6]). The masses of neutrinos are a consequence of a phenomenon

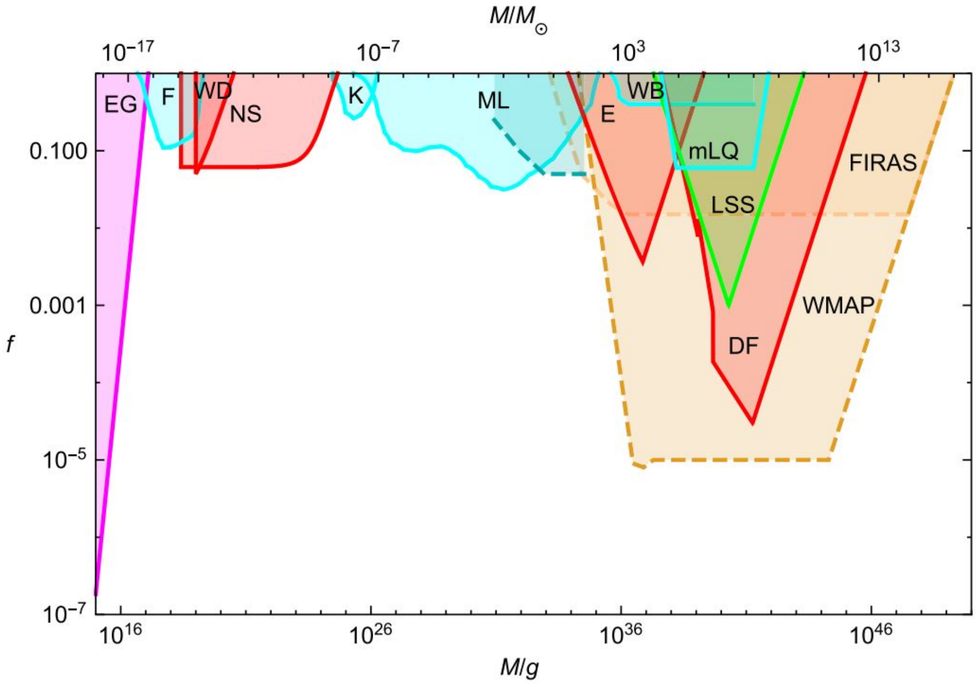

Figure 3.2: Constraints on $f(M)$ for a variety of evaporation (*magenta*), dynamical (*red*), lensing (*cyan*), large-scale structure (*green*), and accretion (*orange*) effects associated with PBHs[49].

known as *neutrino oscillation.* As stated in §2.1, there are three flavors of neutrinos; namely, electron-, muon-, and tau-neutrinos. In neutrino oscillations, a neutrino changes from one of these three flavors into another, which implies their being massive (cf.[62]).

The non-interactive nature of the neutrinos makes it extremely hard to detect—but not impossible. Since the probability of a neutrino colliding with another particle is so low, increasing the number density and amount of particles will naturally increase the probability of collision. That is the main approach behind most neutrino experiments. For example, the Super Kamioka Nucleon Decay Experiment (SuperKamiokande) uses a $32,000$-tons tank of water to catch passing neutrinos. When a neutrino collides with another particle, it turns into another lepton such as an electron or a muon. Because neutrinos are almost massless, and because they do not slow down in water—unlike photons—the leptons produced from neutrino collisions can travel faster than light in water, which causes them to emit a kind of blue light known as *Cerenkov radiation.* By surrounding the inside of the tank with detectors, the Cerenkov radiation is measured, which enables physicists to study the interactions of neutrinos. However, neutrinos are not the only particles that can produce this radiation since the Earth is continuously flooded by energetic particles of CRs. To overcome this problem and minimize other sources of Cerenkov radiation, neutrino experiments are usually conducted deep underground. For example, the SuperKamiokande is located one-kilometer deep down a mine. Another tank of $18,000$ ton of water is also surrounding the first tank, to prevent contamination by the radiation from the rocks surrounding the experiment (cf.[6]).

The calculated relativistic speed of neutrinos at the time of their decoupling from the Universe makes them a candidate of HDM (cf.[5]). But there are several scenarios of their contribution to the DM content—and to the large-scale structure of the Universe—based upon their masses. On one hand, if the electron neutrino mass is of the order of 10^{-1} eV, the contribution of neutrinos to the matter inventory would be roughly the same as the stellar contribution. On the other hand, if neutrinos were to account for most of the DM content of the Universe, their masses have to be of the order of a few keVs. In the meantime, the possibility of a neutrino mass higher than 30 eV has been ruled out since they would have smoothed out any density fluctuations at the early Universe that might have led to structure evolution. The mere existence of the cosmic structure excludes that scenario (cf.[4, 6, 60]). The most recent upper limit for the electron neutrino mass from experimental results comes from the KATRIN experiment, and is 1.1 eV[63]. Several neutrino experiments still running, in addition to data from weak lensing and space experiments, will hopefully further constraint the range of neutrino masses until it can be accurately determined. However, in light of the current constraints, it is unlikely that the contribution of neutrinos to the DM content is very significant. That is because they obey the Pauli exclusion principle and can only be compressed to a certain point. Thus, if their masses are very small as the current limits indicate, the Universe is not big enough to contain enough neutrinos for their contribution to be significant (cf.[2, 6]).

3.2.3 WIMPs

Weakly Interacting Massive Particles (WIMPs) could be the most widely discussed candidates of DM. They are a yet-hypothetical form of stable CDM particles. As the name suggests, they only interact with SM particles or even with each other weakly. The probability of their interactions is comparable to neutrinos. But unlike neutrinos, their masses far exceeds baryonic masses (cf.[4, 6, 26, 60, 64]). Their classification as CDM candidates is due to their having large masses such that they could not have been moving with relativistic speeds to be classified as HDM, or even WDM. The most relaxed limits on WIMP masses is that they are greater than 10 GeV and less than 300 TeV. Many candidates fall under the category of WIMPs, based on the framework used to consider their properties. Perhaps the most popular candidate is the neutralino, which is studied within the frame of SUperSYmmetry (SUSY) (cf.[6, 26, 60]). While some DM candidates are considered in the context of SUSY, the motivation behind the theory is mainly unrelated to DM. SUSY is essentially an attempt to unify the four forces of nature, and there is no evidence so far to prove its success. In SUSY, each SM particle has a supersymmetric partner. The neutralino happens to be the "superpartner" of several SM particles (cf.[6]).

WIMPs are assumed to be relic particles that had fallen out of equilibrium with other particles (that is, frozen out) when the temperature of the Universe dropped below the WIMP mass due to cosmic expansion. Then their interactions stopped and the remaining WIMP population continued to exist to this day (cf.[4, 61, 64]). Based on this production mechanism, most scientists believe that WIMP masses lie in the GeV to TeV range. However, the Lee-Weinberg bound[65] excludes rest masses below 2 GeV. If the above assumptions about WIMPs are true, their relic density would fall within one or two orders of magnitude of the CDM density (cf.[26]).

Before mentioning search approaches for WIMPs, we will first take a look at what their forms of interaction with SM particles or with each other are assumed to be. It is not yet conclusive whether a WIMP is a *Majorana particle*, which mean that it is its own antiparticle and can self-annihilate, or a *Dirac particle* that has a counterpart companion antiparticle, which would mean that they pair-annihilate (cf.[8]). In either case, final products of possible annihilation channels are gamma rays, and pairs of $\nu\bar{\nu}$, e^-e^+, and $p\bar{p}$. Hence, anomalies in the abundance spectrum of these particles in CRs would be regarded as possible WIMP signatures (cf.[4, 6, 60]). Another possibility is that WIMPs from the galactic halo are captured while passing through the Sun. Since the escape velocity from the solar surface is $\sim$ 600 km/s, while it is $\sim$ 1000 km/s from the core of the Sun, a single collision with a nucleus would bring the WIMP's velocity below the escape velocity. It would then lose more energy via consequent collisions, finally being captured and settling at the solar core. If enough of these WIMPs are captured, they would start to annihilate, producing neutrinos either directly or through a tree of pair-annihilation of other products (cf.[4, 8]). The resulting neutrinos will have energies relatable to the mass of the annihilating WIMP ($\sim$ 100 GeV) which will be easy to distinguish from the ordinary flow of solar neutrinos with energies $\sim$ MeV. They can thus be detected and identified as final products of WIMP annihilation.

If they exist, WIMPs could also be tracked in high-energy collider by detecting recoil energies of nuclei that collide with them, then build a statistical argument in favor of WIMPs as the colliding particles (cf.[6, 60, 64]). Needless to say that all the search strategies mentioned above have their challenges. For example, expected recoil energies are less than 100 KeV. So only a very sensitive detector with an extremely minimal background noise from the surrounding material can register such low energies (cf.[4, 8]). There are several experiments currently working and other being planned to workaround these hurdles. More on searches for WIMPs and other DM candidates will be discussed in Chapter 4. Up to this point, there is no conclusive evidence that confirms or rules out the existence of WIMPs as DM candidates (cf.[26, 64]).

3.2.4 Sterile Neutrinos

Even though *sterile neutrinos* are constantly studied in the context of DM, the motivation behind them stem from both astrophysical observations and particle physics models. As discussed in §3.2.2, the properties of neutrinos make them very favorable candidates of HDM. However, current observational constraints puts a very low upper bound on their masses, which rules out the possibility of their constituting the entirety of the DM content in the Universe. Moreover, the fact that neutrinos have masses in itself posed a challenge to the SM in its orthodox form. This prompted a lot of particle physics models to include three right-handed singlet fermions that can explain the neutrino oscillations through the model of the seesaw mechanism with minimum alteration to the SM framework (cf.[10, 66, 67]). An account of the particle physics models behind sterile neutrinos are beyond the scope of this review and can be found in References [67–69].

While these postulated fermions are usually called sterile neutrinos, they are occasionally referred to as "right-handed neutrinos" or "heavy neutral leptons". Theoretical models suggest the existence of a right-handed (spin parallel to momentum) singlet (zero spin) neutrino for each flavor of "active" neutrinos (cf.[4, 10]), which are what SM neutrinos are often referred to in this context. There are another couple of differences between active and sterile neutrinos, in addition to their spins and chiralities (cf.[5, 67]). Those are:

- While the current upper bound of the lightest active neutrino's mass is of the order of 1 eV, the mass of the lightest sterile neutrino is expected to be at least a few hundred eVs.

- While active neutrinos are weakly charged (*i.e.* they are subject to weak interactions), sterile neutrinos are only affected by gravity.

Clearly, if sterile neutrinos are constituents of DM, they would be classified as non-baryonic. As for their thermal classification, they could be either HDM or WDM, depending on their masses. With masses up to a few keV, they can be candidates of WDM. This would solve the problem of large-scale-structure formation due to HDM smoothing out density perturbations seeds, which is encountered in the case of active neutrinos (cf.[66, 70]). Sterile neutrinos are expected to have been produced via resonant and off-resonant oscillations of active neutrinos in the early stages of the Universe. In addition, their expected mass-range implies that they were never in thermal equilibrium with the rest of the Universe (cf.[67]).

Another property of sterile neutrinos is that they are unstable even though their life-time could be greater than the age of the Universe ($\sim \mathcal{O}(10^{17}$ s)). The dominant decay channel is $\nu_s \to \nu\nu\bar{\nu}$. However, this does not imply that sterile neutrinos are completely dark because of the other radiative channel of decay $\nu_s \to \nu\gamma$ (cf.[4, 10]). The energy of the resulting photon can be given by [67]

$$E_\gamma = \frac{M_{\nu_s}}{2}, \tag{3.2.1}$$

which, given the expected mass-range, would place the photon in the X-ray part of the spectrum. This means that they can be observed by X-ray telescopes like *Chandra* and *XMM-Newton*. The monochromatic nature of these photons, implied by (3.2.1), will make it easily detectable and differentiable from the ordinary astrophysical X-ray background (cf.[10, 66]).

In addition to being potential DM candidates, sterile neutrinos have astrophysical significance to another long-standing problem; that is, *pulsar kicks*. Pulsars are neutron stars with poles that intersect the Earth's line of sight during their rotation, which makes it possible to us to detect electromagnetic radiation coming out of these poles. Based on observations, the average space speed of known pulsars ranges from 250 km/s to

500 km/s. However, about 15% of pulsars have speeds greater than 1000 km/s while some have speeds up to 1600 km/s (cf.[66]). There is no known astrophysical mechanism that can drive this discrepancy. Since, on one hand, neutron stars are remnants of supernovae and, on the other hand, about 99% of a supernova energy is emitted as neutrinos, the idea that an anisotropy, caused by the production of singlet neutrinos from mixing of both active and sterile neutrinos, could be what is giving pulsars these "kicks" has been considered (An analysis of this mechanism can be found in References [71, 72]). This provided an additional approach for studying the existence of sterile neutrinos and their potential parameter space through supernova observations (cf.[4, 5]). The highest likelihood would be in the case of a nearby supernova from which an asymmetric neutrino signal can be detected by LIGO (the Laser Interferometer Gravitational-Wave Observatory) and LISA (the Laser Interferometer Space Antenna) (cf.[66]).

Currently, the most-relaxed constraint on the sterile neutrino mass is $M_{\nu_s} > 0.5$ keV. However, for sterile neutrinos to be viable candidates of WDM, observations of the Lyman-Alpha forest gives a mass of at least 2 keV [10]. With these constraints, the cosmological density of sterile neutrinos could reach $\Omega_s \sim 0.2$ (cf.[4]). While the possibility of detecting sterile neutrinos in high-energy colliders is not ruled out, it has not been realized yet. The reason could be that the mass is higher than the currently-available energy scale. It could also be due to low branching ratios since sterile neutrinos only couple feebly with baryonic matter (cf.[67]). The most prominent evidence of sterile neutrinos up to this point is an unidentified emission line at 3.5 keV in the spectra of galaxy clusters. This line has been reported independently by two groups. If it is in fact related to sterile neutrino decays, it would put the mass at 7 keV (cf.[67, 70]).

3.2.5 Axions

While the *axion* is regarded as a DM candidate, the motivation behind that hypothetical particle was solving a theoretical problem in the SM, specifically, in QCD. The problem is known as the *strong CP violation* which is the breaking of the charge-conjugation parity (CP) symmetry. In simple terms, the *CP symmetry* means that the laws of physics are the same for an antiparticle with inverted spatial coordinates as they are for its conjugate particle (cf.[6]). The Lagrangian of QCD has a free parameter, θ, that violates CP symmetry if it is not equal to zero. Since there is no CP violation in QCD, theory puts an upper limit on θ. In the meantime, experimental bounds on the neutron electric dipole moment constraints this parameter to be $< 10^{-9}$. The strong CP violation is the question: *Why is θ so small when it could have been any other value?* To solve this problem, Peccei and Quinn suggested a global chiral symmetry that is spontaneously broken. The axion is the scalar field associated with the breaking of this symmetry and, thus, is considered a boson (cf.[5, 10, 31, 60, 73]).

Since the axion is a field particle, it is expected to have a very small mass. The axion mass is given by [10]

$$m_a \simeq 0.6 \text{ eV} \, \frac{10^7 \text{ GeV}}{f_a}, \tag{3.2.2}$$

where f_a is the axion decay constant which is indicative of the scale at which the Peccei-Quinn symmetry is broken. From a cosmological point of view, axions were produced during the QCD phase transition of the Universe. The QCD phase transition can be described as the time border between quarks roaming freely in the Universe and them congealing into baryons and hadrons. Axions produced during that period, assuming they do exist, should still exist (cf.[6, 10]). There is another potential mechanism of axion production via string decay. However, it is dependent on the timeline of inflation (cf.[5]). In both scenarios, the axions would belong to non-baryonic CDM. However, when it comes to their contribution to the DM content. On one hand, it is unlikely that axions have a large contribution if they were produced through string decay (cf.[31]). On the other hand, if the majority of axions existing today were produced during the QCD phase transition, and if they have a relatively small mass, they could account for the entirety of halo DM where they would have fallen into galactic potential wells during the era of galaxy formation (cf.[4]).

While the axion can decay to two photons, its lifetime is larger than the age of the Universe by many orders of magnitude. Thus, this decay cannot be utilized to detect an axion signature (cf.[4, 61]). Nevertheless, axion conversion into photons can still be boosted by subjecting it to a magnetic field. That is the current approach for detecting axion signatures. When axions pass through a detector cavity that has a strong magnetic field, they are prompted to decay into photons. Based on expectations of the mass range, the resulting photons will be in the microwave part of the spectrum. Moreover, the range of frequencies of the resulting radiation will be quite narrow. Experiments use amplifiers to enhance the chance of detecting any potential axion signature (cf.[5, 6, 60]). Currently, two cavity experiments are looking for axion signatures at the Lawrence Livermore Laboratory and in Kyoto University. Also, the CAST (CERN

Axion Solar Telescope) experiment is trying to detect axions produced via the *Primakoff effect* (the production of neutral mesons from interactions between photon pairs, with one of them being virtual) and streaming to the Earth from the solar core (cf.[5, 66]).

Although the axion has not yet been detected, its mass range is getting more restricted from results of the experiments mentioned above, in addition to astrophysical constraints. The current mass bounds are[60]

$$10^{-5}\ \text{eV} \ \lesssim m_a c^2 \lesssim 10^{-2}\ \text{eV}, \tag{3.2.3}$$

as illustrated in Figure 3.3. Before we conclude our brief review of axions, it is perhaps worth mentioning that even though there is no conclusive evidence regarding the existence of axions or their contribution to DM, there are some astrophysical observations that are best explained by axions. It is conventional to attribute all redshifts of quasars (or Quasi-Stellar Objects) to their cosmological origins. However, in some cases, some quasars with high redshifts have been found to have physical associations with other nearby (low-redshift) quasars. This indicates that the redshifts of these quasars, which are in fact nearby, have non-cosmological origins. It is believed that they are gravitational in origin, and are produced due to bubbles of DM within these quasars. The DM bubbles are thought to be made up of particles with very long lifetimes (hundreds of millions of years), which fit the axions very well[66].

3.2.6 Modified Gravity as an Alternative to Dark Matter

Despite all the efforts devoted to identifying the nature of DM, we are still unable to pinpoint its properties and components with certainty. The only

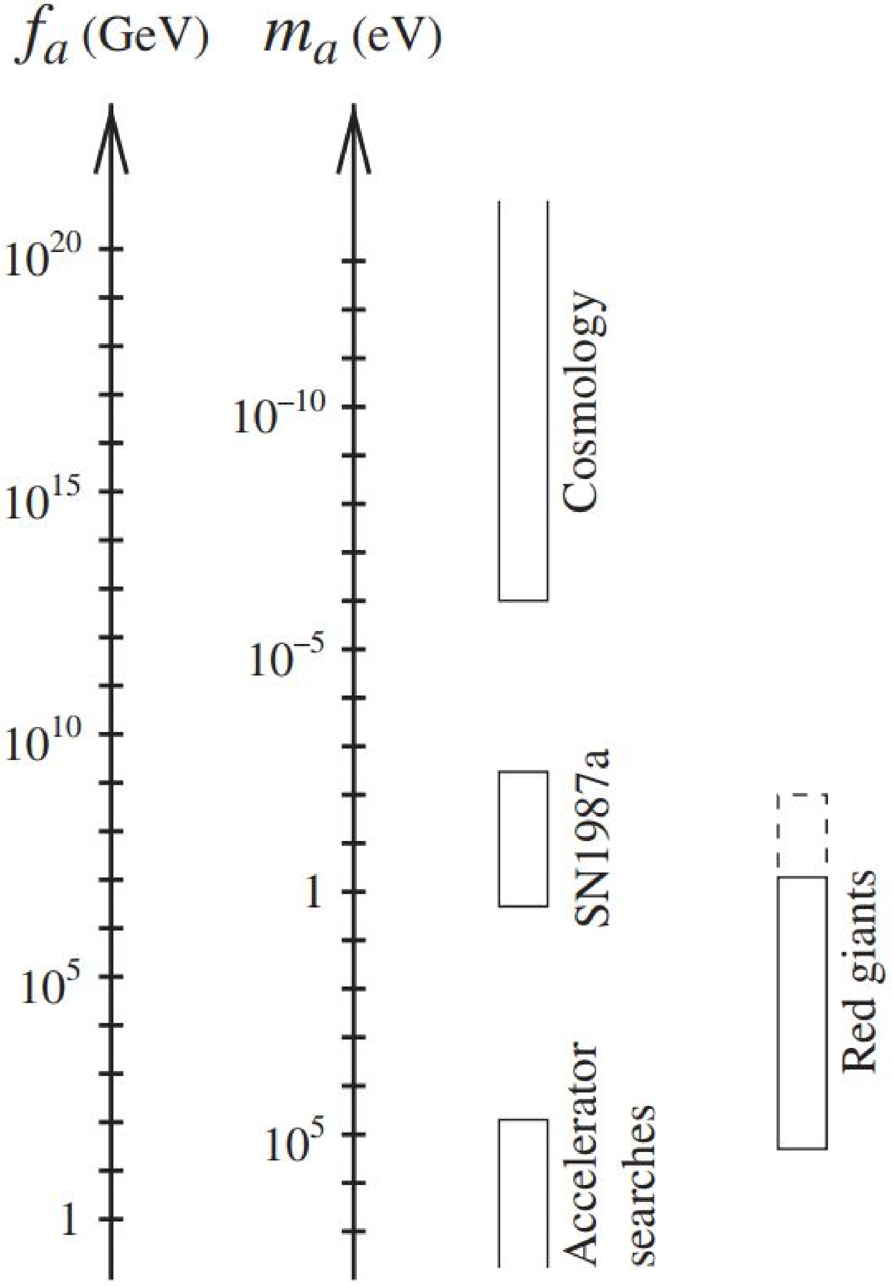

Figure 3.3: The range of parameter space, in terms of both mass (m_a) and the axion decay constant (f_a), that has been ruled out by accelerator experiments, stellar evolution models of red giants, observations of the supernova event SN1987a, and the cosmological energy density of the axions[10].

definite manifestation of what we call DM is gravitational; which poses the question: *Is the answer in the theory of gravity?* The idea that the dark components of the Universe (that is, DM and dark energy) are simply results of missing components in our theory of gravity has been gaining more attention in the last few decades. While most of our attempts are to understand the right-hand-side of the field equations of GR, which encapsulates the matter-energy content of the Universe, many theoretical physicists believe that the answer might be found on the left-hand-side of the equations, which identifies the geometrical representation of the gravitational field (cf.[4, 6, 10]). There are many formulations of gravity that attempt to reproduce the dark energy effect without a cosmological constant, such as $f(R)$ theories[74], and $f(T)$ theories[75]. In what follows we are going to review similar attempts within the context of DM.

The first attempt was in 1983, when Milgrom proposed[76] that Newton's second law does not apply at a very low acceleration, which is true for the outer parts of galaxies. He then modified the law to be

$$\vec{F} = m\,\mu\left(a/a_0\right)\,\vec{a}, \tag{3.2.4}$$
$$\mu\left(x \gg 1\right) \approx 1, \qquad \mu\left(x \ll 1\right) \approx a.$$

In the above equation, $\vec{F}$ is the force field, $\vec{a}$ and a are the acceleration vector and its magnitude, respectively, and a_0 is an acceleration constant. When (3.2.4) is merged with Newton's law of gravitation and the equilibrium between the centrifugal and gravitational force to reproduce rotation curves of spiral galaxies, (1.1.4) becomes

$$v(r) = \begin{cases} r\sqrt{\frac{4}{3}\pi G\rho} & \text{for} \quad a \to \infty, \\ (GMa_0)^{1/4} & \text{for} \quad a \to 0. \end{cases} \tag{3.2.5}$$

This means that the rotation curve naturally becomes flat at the outskirts of a galaxy without the need for another mass component. Milgrom's theory became known as MOdified Non-relativistic Dynamics (MOND) (cf.[6, 8]). Not only was MOND very successful in explaining the rotation curves of galaxies, but it also was in alignment with the *Tully-Fisher relation*, which is an empirical power-law relation between the mass or luminosity of a spiral galaxy and its asymptotic rotation speed. MOND even satisfied the *Faber-Jackson relation*, which is the Tully-Fisher equivalent of elliptical galaxies (cf.[3, 77]). Figure 3.4 shows how well Milgrom's formula fits the observed rotation curve of NGC 2403 compared with the Newtonian curve. The same results were obtained for about 100 galaxies (cf.[78]). Through this procedure, it was found that the acceleration constant (a_0) has a value equal to cH_0, where c is the speed of light and H_0 is Hubble's constant. This in itself is a remarkable coincidence that could be reflection of a cosmological effect in play (cf.[77]).

However, not all observations are exact fits to what MOND predicts. When the predicted dynamical masses of galaxy clusters were compared with their observed luminous masses, both in the case of Newtonian dynamics and MOND, there was still a discrepancy. As can be seen in Figure 3.5, while MOND still fits observations much better than Newtonian dynamics, it is not a perfect fit. The average discrepancy is estimated to be a factor of two larger than the observed mass (cf.[77, 78]). However, there are potential explanations to this discrepancy. It has been proposed that the missing mass could be made up of neutrinos with masses between

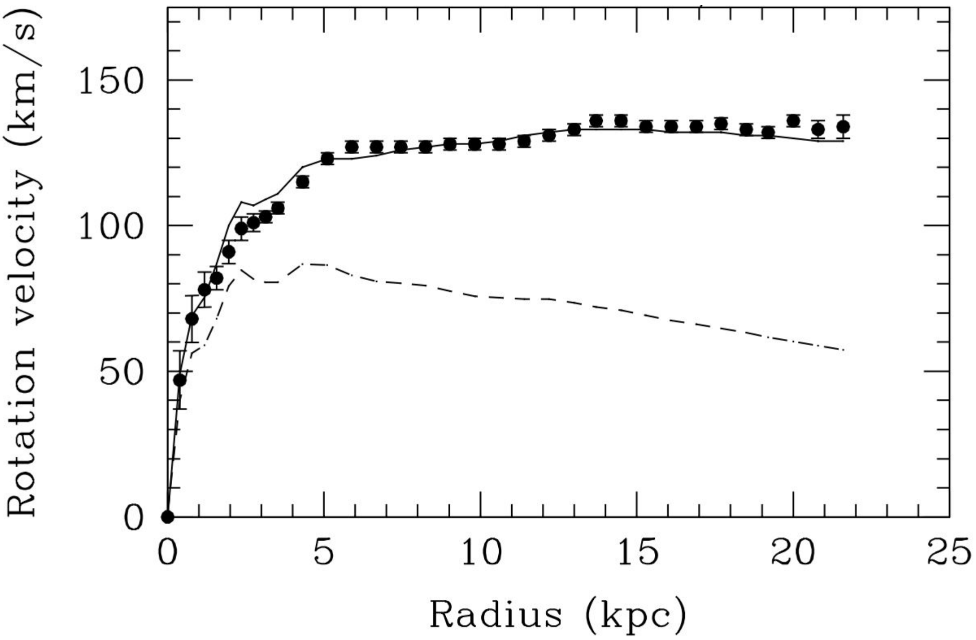

Figure 3.4: The rotation curve of NGC 2403. The curve expected from Newtonian dynamics is represented by the dashed curve while the solid curve represents that determined by Milgrom's formula. The observed rotation curve represented by the points is in agreement with Milgrom's formula[78].

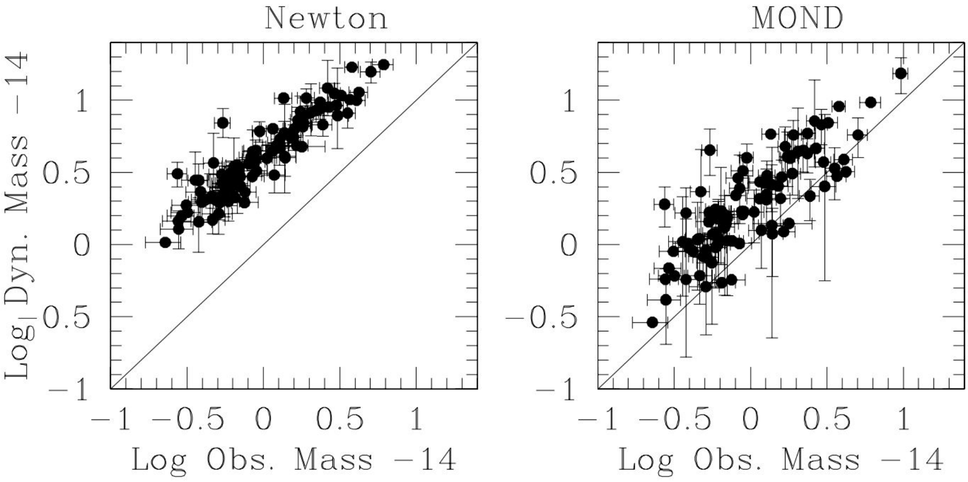

Figure 3.5: On the left is the Newtonian dynamical mass of galaxy clusters, and on the right is the MOND dynamical mass. The solid diagonal line represents the line of perfect agreement between both dynamical and oberved masses[78].

1.5 eV and 2 eV[79]. At this point, there is no observational evidence that conclusively proves or disproves Milgrom's theory (cf.[6]).

Despite the relative observational success of MOND, it has been criticized from a theoretical point of view. It is evident that the motivation behind MOND was to explain the missing mass. Thus, there is no theoretical base for the modification given the formula's empiricism. Another criticism point is the absence of covariance provided by geometrical theories such as GR (cf.[8, 77, 78]), which in turn explains phenomena of gravitational lensing and the large-scale structure of the Universe. This concern opened the door to another modified-gravity theory known as the *Tensor-Vector-Scalar theory* (TeVeS) [80].

As the name implies, TeVeS is a multi-field theory that does not only include the usual metric field of Einstein's GR represented by the tensor $g_{\mu\nu}$, but also a vector associated with a scalar field. The theory reproduces all the results of MOND while integrating all the successes of GR, due to the existence of additional free parameters in the field equations. Since TeVeS, several geometrical theories launched from the same concept of explaining the dark elements of the Universe with gravity. Nevertheless, the intricate nature of these theories still requires more probing from both phenomenological and observational points of views in order to assert their robustness (cf.[77, 78]). Whether the missing mass is a new undetected particle or an illusion of gravity remains to be seen. The answer could still be a combination of both.

3.3 Discussion

In this Chapter, we reviewed different types and classifications of DM, as well as the most-considered candidates of DM from the astrophysical and particle-physical points of view. In recap, a few points worth noting are:

- DM candidates can be classified according to their production mechanism as thermal and non-thermal, or their particle nature as baryonic and non-baryonic, or according to their mass as HDM, WDM, and CDM. Each of these properties would have to be carefully investigated for each suggested candidate, in order to align any potential model with cosmological observations as well as existing theories.

- Despite the results from the MACHO collaboration, which favor MACHOs as DM candidates, observations need to be extended to galaxies other than the LMC to confirm previous findings and assure worries regarding the results being due to the non-flat layout of the LMC.

- The non-interactive nature of SM neutrinos makes them a probable candidate for DM. However, their being classified as HDM means they cannot account for the whole DM contribution in the Universe. To be massive enough to account for most of DM, the Universe would not have evolved into the structures we see today as their temperature and speed would have smoothed out any perturbational seeds.

- WIMPs are perhaps the most-favored candidates for DM. They are classified as cold, non-baryonic DM, and they are massive enough to account for the DM contribution. Their being cold also aligns with the ΛCDM cosmological model. Theory also suggests that their traces can be detected as anomalies in CRs, as will be discussed in detail in the next two Chapters.

- Sterile neutrinos might cover the shortcomings of SM neutrinos as DM candidates. They could also explain pulsar kicks, which favors them from an astrophysical point of view. However, if they indeed exist, they would not be completely dark. That is because one of their decay channels include a photon as a final product. According to the current constraint on their mass, the produced photon would be in the X-ray range making their detection accessible to X-ray telescopes.

- Axions were suggested mainly as a solution to the strong CP violation. Although it might also play the role of a DM candidate, the axion is technically a field particle. This means that it likely has a small mass, making it improbable that it can make up the whole DM content.

- Despite all the objects and particles suggested as DM candidates, some theories advocate strongly that the DM problem is still rooted in gravity. That is, our theory of gravity is missing a piece of the puzzle that would make DM fit in the picture without the need to introduce a new particle. MOND and TeVeS are two of these theories; but there are many others that adopt the same idea while only differing in approach. Nevertheless, in order for the scientific community to accept one such theory, it would have to achieve all the successes of GR, and offer further solutions to currently-standing problems. In addition, it would have to do that with minimum empirical hypotheses.

In the following Chapter, a brief review will be given of the three main approaches to searching for DM; along with a discussion on how they complement one another. We will also consider the advantages and challenges of each approach.

Chapter 4

Searches for Dark Matter

The three main approaches used by astrophysicists and particle physicists attempting to detect DM are: collider searches, direct detection (DD), and indirect detection (ID). Each of these approaches has a different underlying paradigm that determines its search techniques. However, there are two assumptions about DM that they have in common. These are that (cf.[81]):

- at least part of the observed DM effect is due to the existence of new particles that have not yet been identified, and

- there is a form of interaction—regardless how weak it is—between the SM particles and these new dark particles.

Figure 4.1 shows the different potential interactions of DM particles with SM particles. Each of the search approaches mentioned above seeks to detect a different interaction. On one hand, ID experiments try to detect signatures of DM annihilation or decay into SM particles; usually by measuring the flux of rare cosmic-ray components, which will be discussed in §4.3. On the other hand, DD experiments are trying to measure the recoil energy of the scattering of DM coming from outer space off of SM particles, which will be discussed in §4.2. Meanwhile, collider searches are looking for DM particles produced either directly or via a mediator, through pair annihilation of SM particles, which is discussed in §4.1. Because our knowledge of the nature and properties of DM is so scarce, from an observational point of view, each of these search approaches is indispensable if we hope to capture DM (cf[81, 82]).

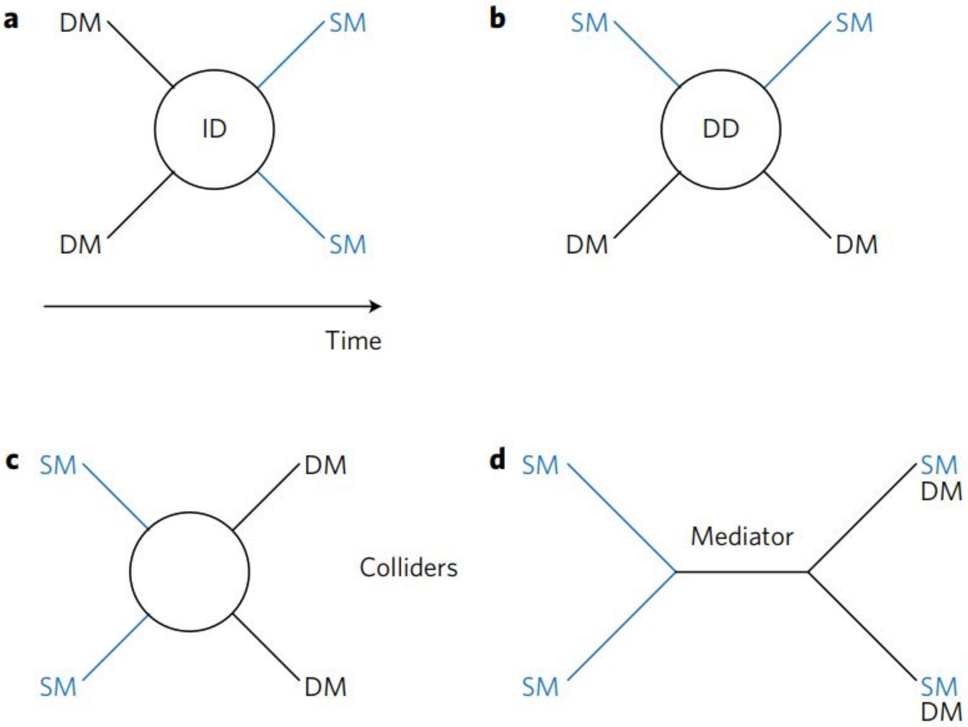

Figure 4.1: A schematic illustration of different potential interactions of DM particles with SM particles, and the corresponding approaches seeking them[82]. **a**, Pair annihilation of DM particles into SM particles, investigated by ID experiments. **b**, Scattering of DM particles off of SM particles, where DD experiments try to measure the recoil energy of the collision. Meanwhile, collider experiments seek to detect pair production of DM particles from the annihilation of SM particles, either directly, **c**, or through a mediator, **d**.

4.1 Collider Searches

With DM making up more than five times the luminous matter represented by the SM, it is naturally a subject of interest for particle physicists. They see DM as a key to physics BSM. One way to search for this key is with high-energy particle colliders, which has been undeniably successful in unveiling many fundamental components of the SM; the last of which was the *Higgs boson* [21, 22]. Thus, there is no reason why collider searches cannot contribute to the study of DM, even if they are not sufficient to cover all potential candidates. As mentioned above, collider searches are based on the possibility of producing pairs of DM particles in colliders from pair-annihilation of SM particles, either directly or via a mediator. If detecting such particles is indeed possible, colliders will have some advantages over astrophysical searches. Firstly, the kinematic configuration of the production process(es) will be accessible for further probing. Secondly, the high luminosity of the colliders will offer a large number of DM events that can be analyzed to decipher the properties of the DM particles involved. Lastly, all the signal background and all uncertainties can be understood and accounted for, which is not the case in astrophysical searches if we consider the many unknown variables [83]. However, for a particle to be identified as a candidate for the DM relic density, its lifetime has to be longer than the age of the Universe. While collider experiments can assess whether a particle decays or not within the detector, they cannot evaluate its stability on a cosmological timeline (cf.[82]).

The advantage of knowing the initial conditions of an event in collider experiments constrains the output so that anomalous events can be spotted. For example, while DM particles cannot be directly detected in collider experiments, the rest of the event products can. From these products, an invisible particle can be inferred from a missing component in the transverse momentum plane. However, one should note that an invisible particle is not necessarily a DM particle; and that is why other search approaches are needed. Nevertheless, this approach can be effectively used to explore and constrain the parameter space of DM candidates.

Collider experiments can be categorized into lepton colliders and hadron colliders. Lepton colliders are effective for studying electroweak interactions without the added complexity of strong interactions. The most prominent experiments of this category were ALEPH, DELPHI, OPAL, and L3. They were all carried out at the LEP (Large Electron-Positron) collider at CERN which operated between 1989 and 2000. Even though lepton experiments would have a much higher signal-to-background ratio, they have lower luminosities in general, which would lessen the chances of a DM production signal. Still, there are currently several proposals for lepton experiments that could be optimized to better the chance of DM detection (cf.[83]). As for hadron experiments, many of them are carried at several hadron colliders. In the context of DM, searches had been carried out at the Fermilab's Tevatron [84], for example, which ceased to operate in 2011. The bulk of current data is provided by experiments at the Large Hadron Collider (LHC). The main experiments concerning DM are ATLAS and CMS (cf.[82]).

Let us now consider how the detection of new particles can be pursued in colliders. Although collider searches can never independently conclude that a detected particle is a DM particle—because results have to be confirmed by cosmological observations of the relic density and lifetime of such particles—they offer the advantage of studying the kinematics of potential interactions of DM with SM particles in more detail than can ever be obtained by other search approaches.

Since DM particles will not manifest visibly at colliders, their existence has to be inferred through other signals. The most-telling sign of an invisible particle is a missing transverse momentum, often denoted as $\not{E}_T$. The transverse momentum in the plane perpendicular to the collision beam is conserved and equal to zero; thus, a negative sum of the transverse momenta of all the final products of an event is indicative of a signal of an invisible particle. However, more-specific search strategies are utilized as well. These strategies are based on theoretical assumptions of DM production. One of these assumptions is that the production DM particles is usually accompanied by an energetic SM particle, such as a photon or a boson. This assumption can be used to be more selective about events. Thus, events with a missing transverse momentum and a high-energy SM particle are targeted. This search strategy is dubbed the *mono-X strategy*. It can be considered the most-commonly-used at colliders. Another search strategy that falls under the search for physics BSM is based on the assumption that some SM mediators decay into pairs of DM particles. So, if such a boson is detected without detecting its final products, it could be assumed that DM was produced. However, this puts a limit on the mass of the produced DM particles according to the mass of the mediator (cf.[81, 82]).

When designing collider experiments with the aim of detecting DM, there are two complementary factors to consider. The first is the scarcity of conclusive evidence about the properties of DM particles, which hinders the optimization of experimental design based on expectations. This requires any search to be based upon a theoretical model where the degree of constraints imposed by the model is determined by the scope of the experiment. A theoretical model also allows for comparing results with non-collider searches. The second factor is the vast parameter space of the properties of DM candidates, which necessitates less-constrained searches. This can be achieved by using benchmark models with generic properties that apply to most DM candidates. Different types of models are used for DM collider searches. These are briefly discussed in the next

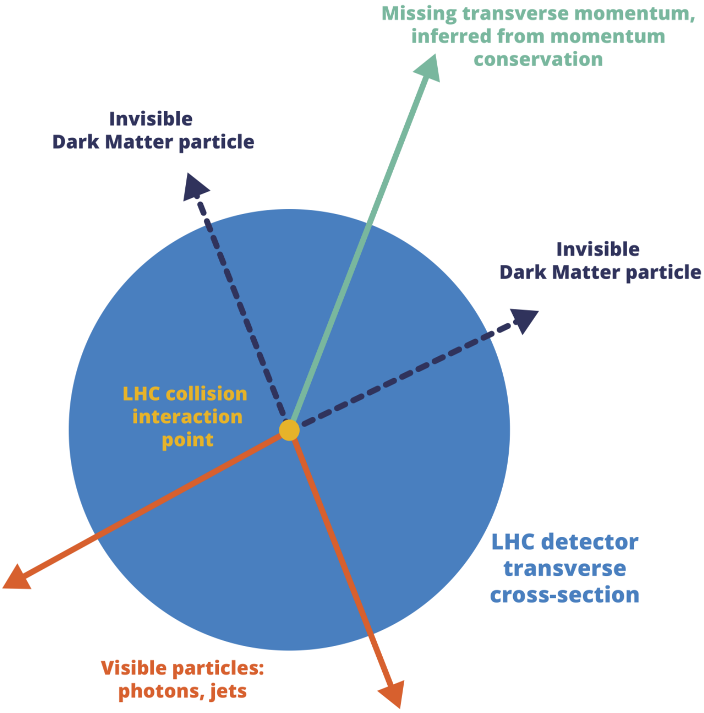

Figure 4.2: A schematic illustration of the concept of missing transverse momentum from which the production of an invisible particle is inferred in an LHC detector [82].

few paragraphs.

There are many types of DM theoretical models that it is beyond the scope of this work to review all of them. However, the most relevant models to our discussion are (*i*) models where DM particles can be produced in collider experiments due to interacting effectively with SM particles; (*ii*) models in which DM particles are *Dirac fermions* (*i.e.* half-spin particles with antiparticles different from themselves, unlike *Majorana fermions*); and (*iii*) models based on the cosmological assumptions that DM was once in thermal equilibrium with the Universe and that the current relic density of DM particles is a consequence of their freeze-out (cf[81]). A review of other types of models can be found in References [85, 86].

A category of models called *portal models* is based on the possibility that an interaction between SM and DM particles is carried out through a mediator (see Figure 4.1**d**). Some models are even more specific as to assume that the Higgs and Z bosons are examples of these mediators. Such models are often referred to as Higgs and Z portal models [87, 88]. It is to be noted that these bosons can still decay into SM particles; and collider searches can constraint portal models by studying such decays (cf.[81]). While current colliders have reached energies and luminosities high enough to investigate Higgs and Z portal models, the mediator of the interaction might still be an unidentified particle undetectable at the current energy scales of colliders. Models integrating such mediators are categorized as models of physics BSM. In other cases, the interaction might to happen on contact (see Figure 4.1**c**) instead of being mediated. The production mechanism is then outlined by nonrestrictive theoretical frameworks known as EFT (Effective Field Theories) [89, 90].

Nevertheless, if an unidentified mediator is within or below the energy scale accessible to current experiments, applying an EFT might restrict the search scope. In such cases, *simplified models* [91, 92] are used instead. These models exclude details of physics higher than the energies relevant to the collider phenomenology. Thus, simplified models can play the role of benchmarks, while they can be implemented within a larger model as an experiment progresses. But the problem with these models is that they can fail to accommodate the complexity of collider signatures. To avoid this issue, some *less-simplified models* are developed to focus on a certain class of models (cf.[93, 94]). These models can be a middle ground between overly-generic and complex models.

There still exists complete theories developed for exploring BSM physics. These can be used to investigate mechanisms of DM (or invisible) particles production. However, they cannot be used for casting a wide net, and have to target certain hypotheses. One of these theories is SUSY, for which experimental evidence is yet to be found [95]. In general, all models of BSM physics that contain stable feebly interacting non-SM particles, and do not contradict astrophysical observations of DM, can be regraded as DM models (cf.[81]). There are other models as well that explore alternate possibilities for DM production and interactions; some of these can be found in References [96–98].

As mentioned above, most current DM data in terms of collider searches are provided by the ATLAS and CMS experiments. So, let us now consider the advantages and challenges of DM searches at hadron colliders. On one hand, when it comes to discovering new particles, hadron colliders have had unrivaled success. Especially in the case of producing massive particles, hadron colliders have much more potential, since the colliding hadrons are orders of magnitude heavier than leptons. This makes it more probable for unknown particles to be produced more abundantly. On the other hand, hadronic events are much more complex compared to leptonic ones, for the same reason. The high energy of the interactions causes the background of known processes to be very high compared to the sought signal. This increases uncertainties, which, in turn, makes it harder to detect the signal even when produced. Thus comes the need to determine these backgrounds with great precision, which is a challenge in itself especially in the case of small backgrounds (cf.[81, 83]).

Another challenge that faces hadron collider experiments is designing the trigger system. Since hadronic colliders produce very high numbers of events, it is not practical to save the data for all of them. In the end, only a small number of events can be studied. Thus, it needs to be quickly decided which events to save and which to discard. This is usually done by selecting events with properties that are promising to the physics questions that the experiment is trying to answer. For example, an experiment might only target events with missing transverse momentum. Nevertheless, there are several sources that could create a misleading signal that coincides with the collision event, such as CRs and detector noise [83]. This means that any event with $\not{E}_T$ below a certain threshold would not be stored, which in turn gives rise to another issue. That is the dismissal of signals with signatures below that determined threshold [81]. However, current experiments are trying to overcome this challenge by only storing data of the final products of such events instead of the information of the whole event [99].

As discussed above, results from collider searches cannot be used alone to reach any conclusions about DM. However, constraints are continuously imposed on the parameter space of DM properties as a result of these searches. But even these constraints have to be considered in light of the theoretical model applied. The LHC DM Working Group coordinates the depiction of results [100]. Other collaborations, such as GAMBIT [101] and MasterCode [102] have been offering different tools to help combine constraints from collider searches with results of DD and ID searches.

4.2 Direct Detection

As mentioned before, direct detection (DD) experiments are based on the hypothesis that, since DM particles are electrically neutral, they will not interact with atomic electrons; however, they will gravitationally interact with atomic nuclei by elastically scattering off them. This scattering of incoming DM particles off nuclei on Earth would then cause a momentum transfer that would in turn produce recoil energy. These DD experiments try to detect this energy. On one hand, the interaction rate is expected to be extremely low: less than one event per ten days per kilogram of material. On the other hand, this rate depends on the atomic number of the material used such that it is proportional to A^2 in spin-independent interactions and to A in spin-dependent interactions. Hence, experiments try to increase the collision rate by choosing materials with high atomic numbers (cf.[4, 103]). It is still worth noting that the collision rate is affected by several other factors, which makes it a spectrum. These factors include the DM particle mass and energy, the expected recoil energy, and the velocity of the Earth in the Galaxy. This makes isolating and identifying a signal very challenging. Figure 4.3 shows the recoil-energy spectra for four different target nuclei assuming spin-independent interactions.

The Earth velocity referred to above is not just the circular motion with $v_c = 220$ km/s of the Sun around the galactic center, but it is the velocity of the Earth moving through the DM halo, which is given by[103]

$$v_E = v_\odot + v_\oplus \, cos(\theta) \, cos[\omega(t - t_0)], \tag{4.2.1}$$

where $v_\odot = v_c + 12$ km/s is the Solar motion w.r.t. v_c taking into account the peculiar motion of the Sun, and $v_\oplus = 30$ km/s is the orbital speed of the Earth around the Sun. The angle $\theta \approx 60°$ is the inclination angle of the Earth's orbit to the galactic plane. The angular frequency is given by $\omega = 2\pi/1\text{yr}$ where the phase is fixed at $t_0 =$ June 2, when the sum $v_\odot + v_\oplus$ is at its maximum. Figure 4.4 shows the different motions relevant to DD experiments. This causes an annual modulation that is to be expected

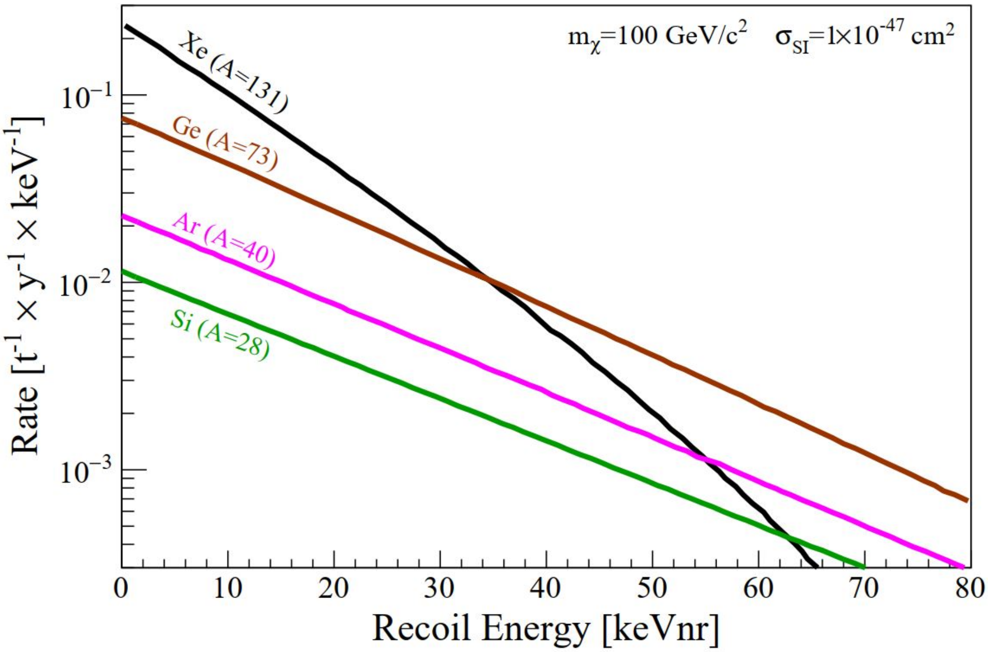

Figure 4.3: Recoil-energy spectra produced by a DM particle χ of mass m_χ in several common target materials, assuming a spin-independent χ-nucleon interaction cross section of $\sigma_{\rm SI}$. While the rate increases with A^2, the rate decreases at higher energies for larger nuclei (*e.g.* Xe) because of form-factor suppression[103].

in the signal. There is also another type of modulation that arises from the daily motion of the Earth and changes the rate of DM events in DD experiments. Even though these modulations complicate detection, they can be advantageous. Some DD experiments try to detect a modulation to prove that a certain detected signal does in fact have a DM origin (cf.[4, 78]).

Before we can further explore DD experiments and results, we first need to outline what these experiments can observe. A recoil can set off three processes inside a detector: phonons, ionization, and scintillation. A phonon is a normal mode of vibration where all the atoms in a lattice oscillate uniformly at a single frequency. This vibration is detected as an

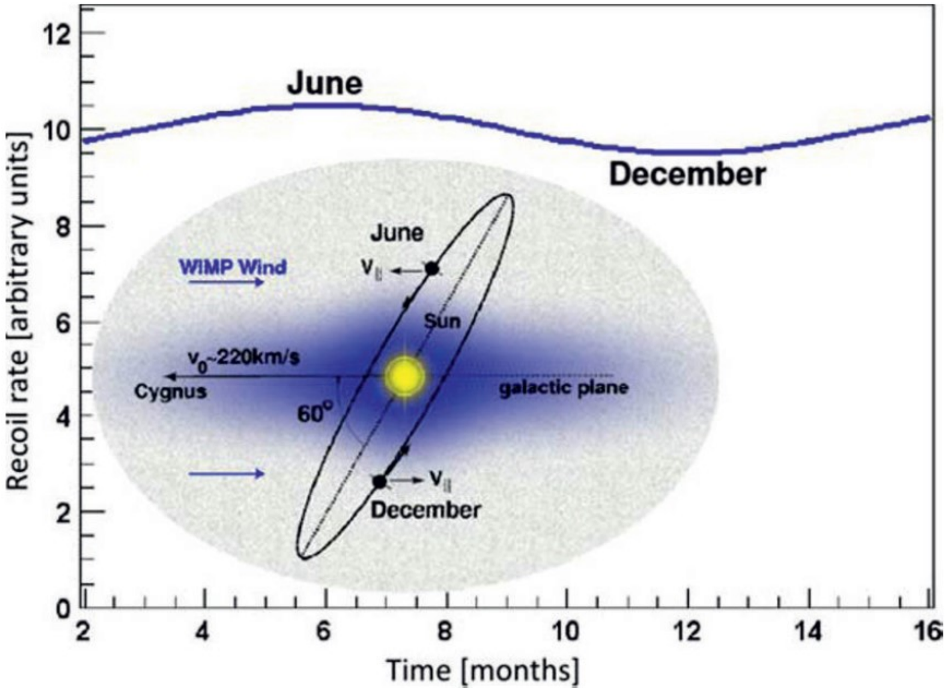

Figure 4.4: Illustration of the Earth's motion relevant to the DM halo where the direction of the Constellation Cygnus is indicated. The expected recoil rate is represented as a function of time[4].

increase in temperature by a bolometer (resistor) technique. Ionization signals arise from the fraction of recoil energy that is directed towards collision with the electrons, which would also give rise to phonon energy. Finally, scintillation occurs when the collision impact excites an atom or a molecule in the ground state, this excitation is eventually re-emitted as light (luminescence), which can be detected and measured (cf.[5]).

The most challenging aspect of these experiments is background mitigation. There are many sources of backgrounds that require sophisticated strategies in order to isolate them from the desired DM signal. These sources include interactions with the detector environments, the components of the detector setup itself, low-energy solar neutrinos, and cosmic ray muons (cf. [103]). To get an image of the challenge these backgrounds represent, it is useful to know that in an unshielded environment, the background signal rate can be 100,000 times larger than the rate of the signal expected from DM[78]. Many strategies are utilized and combined to minimize the effect of these backgrounds, of which a review can be found in Reference [104]. Some of these strategies are using shields to suppress signals from the immediate environment of the detector, vetoing muon events by rejecting any signal that coincides with the detection of a muon, employing several techniques to selecting detector materials with low intrinsic radioactive contamination, purifying target crystals from any radioactive impurities, and using more than one independent signal to identify and reject these background events (cf. [103]).

There are several properties that are desirable in DD experiments detectors. They allow the optimization of multiple factors such as recoil impact, signal amplification, and background rejection and minimization. As shown in Figure 4.3, choosing a material with a higher mass number increases the probability of impact, *i.e.* the interaction rate. In addition, energy resolution is of the utmost importance with such a low signal-to-background ratio. Higher energy resolutions can be achieved by keeping the detector at a very low energy which would mean that a small increase in temperature due to the tiniest energy disposition could be examined. Moreover, the detector's ability to distinguish between nuclear and electronic events would allow it to identify the signal while rejecting the background (cf. [5, 103]).

Based on the processes outlined above, there are multiple approaches to detecting a signal. Ideally, DD experiments aim to detect both the magnitude of the recoil energy and the directionality of the recoiling nucleus. This, in turn, would enable the extraction of DM mass and scattering cross section. Experiments also have to establish an energy scale for the detector to account for the *signal quenching* phenomenon, which is simply that the nuclear recoil signal is smaller than the electronic recoil signal deposited by the same energy deposit (cf. [103]). The three detection techniques indicated above give rise to different classes of experiments. The main classes, along with some example experiments are[5]:

1. Scintillator detectors such as DAMA, NAIAD, ANAIS, and KIMS.
2. Ionization detectors such as CoGENT, TEXONO, and MAJORANA.
3. Phonon detectors, which are cryogenic detectors operated with temperatures below 1°K, include CDMS (CDMS II), SuperCDMS, GEODM, EURECA, and CRESST II.
4. Threshold detectors that are not affected by electron recoil, and are only sensitive to high energy density. They are also often referred to as bubble chamber detectors. These include COUPP, PICASSO, and SIMPLE.
5. Some detectors also use noble liquids to allow for detection in scintillation mode, ionization mode, or in both simultaneously. Such experiments include ZEPLIN III, LUX, XMASS, XENON10 (XENON100), WArP, and ArDM.
6. Other types of detectors are optimized for reconstruction of recoil tracks in 3D. This offers measurement of the directionality of the recoil track, and hence, of the incoming DM particle. These detectors are utilized in detecting directional variation due to the diurnal motion of the Earth. Some examples of them are DRIFT and NEWAGE.

Let us now highlight some advantages of certain detector classes[103]. For example, cryogenic detectors have higher energy resolutions that enable high-precision measurement of energy. In addition, they can utilize two detection channels, which offers more efficient background rejection. Bubble chamber detectors are somewhat similarly advantageous. The bubble formation probability can be adjusted such that only certain events would produce a bubble based on the energy loss of the recoiling particles. Thus, undesirable background sources, such as γ- and β-events can be excluded by a factor $< 10^{-9}$. Table 4.1 shows a list of the most prominent DD experiments with published results (see references within Reference [103]).

Up to this point, no experiment has found a definite DM signal. All results have been around the expected background signal (cf.[78, 103]). However, there is one anomaly; that is, the DAMA experiment. It has been claimed that a modulation signal has been observed in the range $2-5$ keV. The signal has supposedly been observed during both DAMA phases, as shown in Figure 4.5[105], with a statistical significance of $12.9\,\sigma$ with no potential sources other than DM (cf.[103]). Nevertheless, this signal is still controversial as no other experiment could corporate it, even the CDMS which has a much higher sensitivity than DAMA's. However, it has been argued that the DM-nucleon interaction could be spin-dependent whereas CDMS is only sensitive to spin-independent interactions. Meanwhile, DAMA could detect such a signal. This loophole has also been covered recently by COUPP, which is very sensitive to spin-dependent interactions. Thus, the DAMA signal remains unaccepted until another experiment confirms it (cf.[103]).

Table 4.1: Some of the leading experiments of DD experiments that have published results, alphabetically ordered. Some of them are no longer in operation, while some others are still in prototype phases[103].

Experiment	Type	Target	Laboratory
ANAIS-112	Crystal	NaI	Canfranc
CDEX-10	Crystal	Ge	CJPL
CDMSLite	Cryogenic	Ge	Soudan
COSINE-100	Crystal	NaI	YangYang
CRESST-II	Cryogenic	$CaWO_4$	LNGS
CRESST-III	Cryogenic	$CaWO_4$	LNGS
DAMA/LIBRA-II	Crystal	NaI	LNGS
DarkSide-50	TPC[1]	Ar	LNGS
DEAP-3600	Single phase	Ar	SNOLAB
DRIFT-II	Directional	CF_4	Boulby
EDELWEISS	Cryogenic	Ge	LSM
LUX	TPC	Xe	SURF
NEWS-G	Gas Counter	Ne	SNOLAB
PandaX-II	TPC	Xe	CJPL
PICASSO	Superheated Droplet	C_4F_{10}	SNOLAB
PICO-60	Bubble Chamber	C_3F_8	SNOLAB
SENSEI	CCD[2]	Si	FNAL
SuperCDMS	Cryogenic	Si	above ground
XENON100	TPC	Xe	LNGS
XENON1T	TPC	Xe	LNGS
XMASS	Single phase	Xe	Kamioka

[1] Time Projection Chamber

[2] Charge Coupled Device

Although no definite DD signal of DM has been obtained, the results are increasingly constraining the properties of interaction and, consequently, of DM candidates. Figure 4.6 shows a set of constraints compiled for the WIMP mass[106]. More experiments are currently under consideration for the search for light (eV-MeV) DM candidates, instead of devoting most efforts to the WIMP search[107].

4.3 Indirect Detection

The indirect detection (ID) of DM seeks to identify anomalies which might be originating from the annihilation of DM particles in the galaxy. These anomalies are expected to manifest as distortions in the Cosmic Ray (CR) spectrum whereas all ordinary astrophysical sources would act as backgrounds to this signal (cf.[5, 10, 78, 108]). There are many potential channels for these annihilation processes. However, the observable final products are believed to be rare antimatter components (*e.g.* positrons, antiprotons, and antideuterons) in addition to neutrinos and γ-rays[10]:

$$\chi + \chi \longrightarrow q\bar{q}, W^+W^- \cdots \longrightarrow \bar{p}, \bar{D}, e^+, \gamma, \nu. \tag{4.3.1}$$

While this hypothesis has not been proven yet, the argument behind it is no longer controversial. It is thought that DM particles in the galactic environment, after many scattering events, slow down below a certain velocity. If a particle then encounters a massive celestial object that has an escape velocity higher than the particle's, it is captured gravitationally. Then it accumulates at the core of the celestial objects. If enough DM particles are accumulated at the core such that their density is high enough,

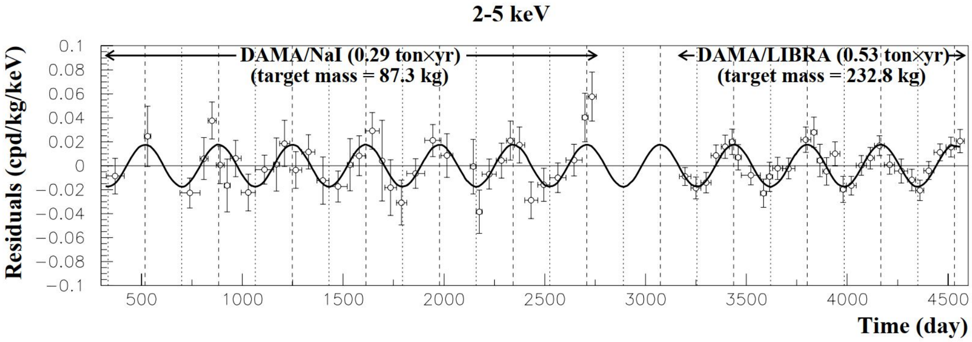

Figure 4.5: Residuals around the mean signal for both phases of the DAMA experiment [105].

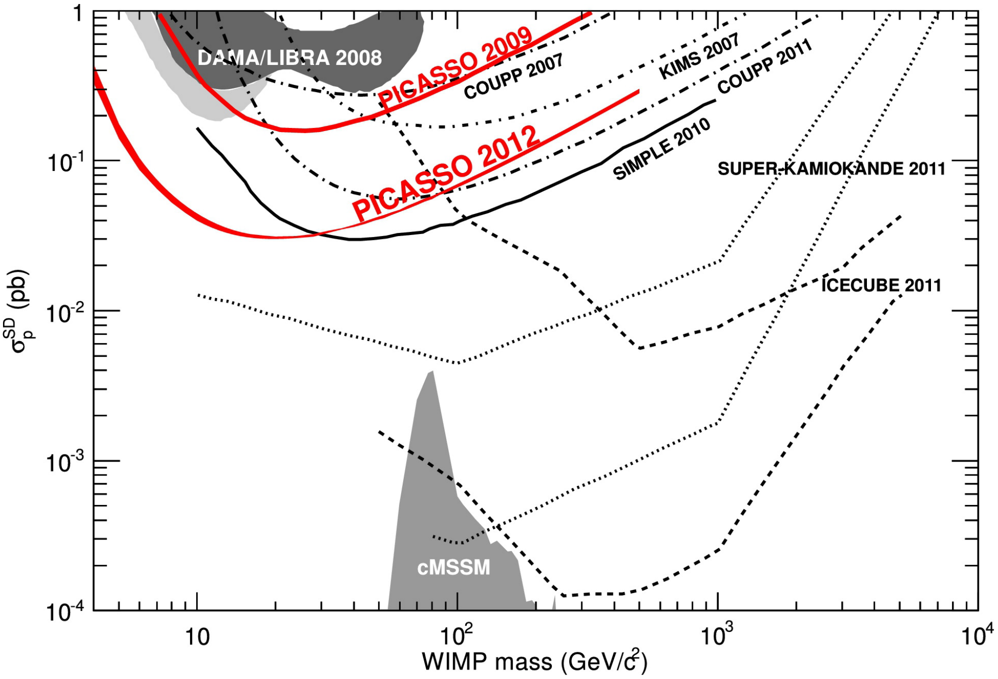

Figure 4.6: Upper limits at 90% C.L. on spin-dependent WIMP-proton interactions, compiled by PICASSO collaboration[106].

the particles start to pair-annihilate producing SM products. Some potential celestial objects are the Sun and the Earth. The products of these annihilations are what ID experiments aim to observe[4, 5].

The strength of such signal would of course depend on several factors. The annihilation rate is one of these factors, which in turn depends on the DM density distribution. The galactic center is expected to have a higher DM density. However, this remains controversial. If it is true, it would be both an advantage and a disadvantage. While the signal coming from this central region would be much stronger than from other targeted areas, the background would also be stronger due to the high abundance of other celestial objects as well at this central hub. It would then depend on how much other astrophysical sources of this region are well-studied and mapped. Nevertheless, the importance of DM density distribution is much higher for γ-rays and neutrinos than it is for the indirect signal of antimatter components. That is because antimatter diffuses and the signal we can observe near the Earth would depend on local factors more than on the galactic structure. On the other hand, since antimatter components are charged, they would be more crucially affected by propagation parameters and the interaction of their source with the Earth[4, 10].

Several experimental techniques are employed in the indirect search for DM. Each of them is more suitable for certain targeted components. The techniques include detectors on balloons and in space which are more optimal for antimatter studies in addition to γ-ray study. Other techniques are large ground CR and γ-ray detectors, as well as underground telescopes that aim to study neutrinos[10]. Each potential component of DM annihilation products has its advantages as well. In what follows, these advantages are outlined for each targeted component; and a brief review of recent results from ID experiments for different components is given. It is to be noted that antiproton results will be addressed in more detail in Chapter 5.

Neutrinos are optimal for targeting certain sites of DM annihilation. Because they are only weakly interacting, they are not deflected due to encountered magnetic fields and other propagation parameters[5]. Neutrinos produced by DM are expected to by highly energetic. Thus, they eventually collide with SM nuclei producing muons that move with relativistic speeds. Sometimes the muons are even "faster than light", when the collision happens within a medium (*e.g.* water), which gives rise to Cherenkov radiation which could be tracked to its origin by photo-multiplier tubes. The high energy of the targeted muons is also convenient for identifying the signal from its background. Since there is a continuous shower of atmospheric CR muons bombarding the Earth, it could have been challenging if the targeted signal was in the same energy range. However, atmospheric muons are not as energetic as the DM final products, and they would not be able to penetrate the entire Earth. Thus, neutrino telescopes targeting DM are pointed downward toward the Earth's core such that the only muons that reach them are those with energies high enough to penetrate the entire Earth (cf.[78]). Some of the experiments targeting neutrinos are AMANDA, ICECUBE, and ANTARES (cf.[4]). However, the same reason that makes neutrinos a favorable target to search for DM makes them hard to detect. That is, their weakly interacting nature makes them harder to detect even with massive detectors. Thus, there has not yet been any evidence of neutrinos from DM annihilation or decay although constraints have been accordingly added on the rate of DM decay in the center of the Earth.

Another signature of DM could be γ-rays, which have the advantage of carrying a lot of information about the source location. Thus, they are optimal for searching for DM in galaxies other than the Milky Way. However, their signal would need to first be extracted from a continuum energy spectrum as a background. Experiments that target γ-rays can be divided into two categories: space-based and ground-based. Space-based experiments, such as Fermi LAT, EGRET, PAMELA, and AMS-02, mainly focus on low-energy γ-rays while ground-based experiments, such as VERITAS, MAGIC, and H.E.S.S., can only access high-energy γ-rays (cf.[4, 5]). As mentioned, the nature of γ-rays makes them optimal for targeting certain regions for detection. The most sought regions include the galactic center and halo. Several experiments have claimed over the years that they have detected an excess γ-ray signal near the galactic center, including Fermi LAT, EGRET, H.E.S.S., and MAGIC (cf.[5, 78]). But there are several astrophysical alternatives that could explain the observed excess at the current significance. This is a clear example of the challenges that face ID of DM. Whenever a potential signature has been observed, there is also an abundance of alternative explanations (cf.[4]). The only way to overcome this difficulty is by precise identification of all contributions from ordinary astrophysical sources. Only then would we be able to pinpoint any anomalies with certainty. While experiments that seek the detection of neutrinos and γ-rays face this challenge, it particularly hinders conclusions about charged-particles signals, as would be shown below and in §5.3. So, as it currently stands, there is no conclusive evidence of a γ-ray signal from DM.

Other DM signatures that ID experiments seek to detect are charged antimatter components, such as positrons, antiprotons, and antideuterons. That is because they are rarer than their matter counterparts which makes them more convenient for identifying any potential excess signature (cf.[108]). To get a measure of how rare they are: At ~ 1 GeV, the $e^+/(e^+ + e^-)$ ratio is $\sim 10\%$, while the $\bar{p}/p$ ratio is about 10^{-5}[4]. However, these components are greatly affected by propagation parameters, in addition to the existence of a secondary antimatter flux from the interactions of primary CRs. Thereupon lies the need fro measuring these fluxes with extreme precision. Experiments targeting antimatter components are either carried out on balloons or are space-based. In what follows, a brief account of positron results is given, while antiproton results are discussed in Chapter 5.

Secondary electrons and positrons are produced through the collisions of protons and hydrogen atoms where they first produce pions that decay into muons that finally decay into electrons and positrons. This chain can be represented in the form[10]

$$p + H \longrightarrow X + \pi^{\pm}$$
$$\pi^{\pm} \longrightarrow \nu_{\mu} + \mu^{\pm}$$
$$\mu^{\pm} \longrightarrow \nu_{\mu} + \nu_{e} + e^{\pm}.$$

As for the positron ratio, general estimates that take into account production cross sections and propagation factors expect it to decrease with increasing energy. However, two experiments (HEAT and PAMELA) have reported a sudden increase above 10 GeV that could be interpreted as a DM signature (cf.[5, 10, 78]). A compilation of experimental data superimposed to the expected bounds from ordinary astrophysical parameters is shown in Figure 4.7[109]. However, other experiments (FGST and H.E.S.S.) with high sensitivity could not reproduce these results. It is to be noted, nonetheless, that both of these experiments cannot distinguish positrons from electrons but instead measure their total flux (cf.[78]). Moreover, the AMS collaboration has confirmed detecting the same excess signal with much higher precision[110]. Thus, these findings still need further inspection by other experiments before any interpretation could be accepted. Several other explanations for the signal have already been suggested (cf.[4, 5, 10, 78]), whereas pulsars and supernova remnants are the most favored alternative sources for the signal. It can be seen, however, from Figure 4.7, that complementary observations are essential to further constrain the expected background, based on propagation parameters, in order to define the contributions from potential alternative sources and confirm or rule out a DM signal.

4.4 Discussion

In this Chapter, we have reviewed the main approaches used in the search for the identity of DM. We have explored the advantages of each approach along with the challenges that face it. We have also discussed how these approaches can complement each other to draw a more defined picture of what DM is. Here are a few points worth recapping:

- There are three main approaches for the search for DM. Each of them is based on a different paradigm about the way DM particles interact with SM ones. On one hand, collider searches are based on the idea that SM particles can pair-annihilate producing pairs of DM ones, either directly or via a mediator. On the other hand, DD experiments rely on the hypothesis that DM particles recoil off SM nuclei producing a recoil energy that could be amplified and

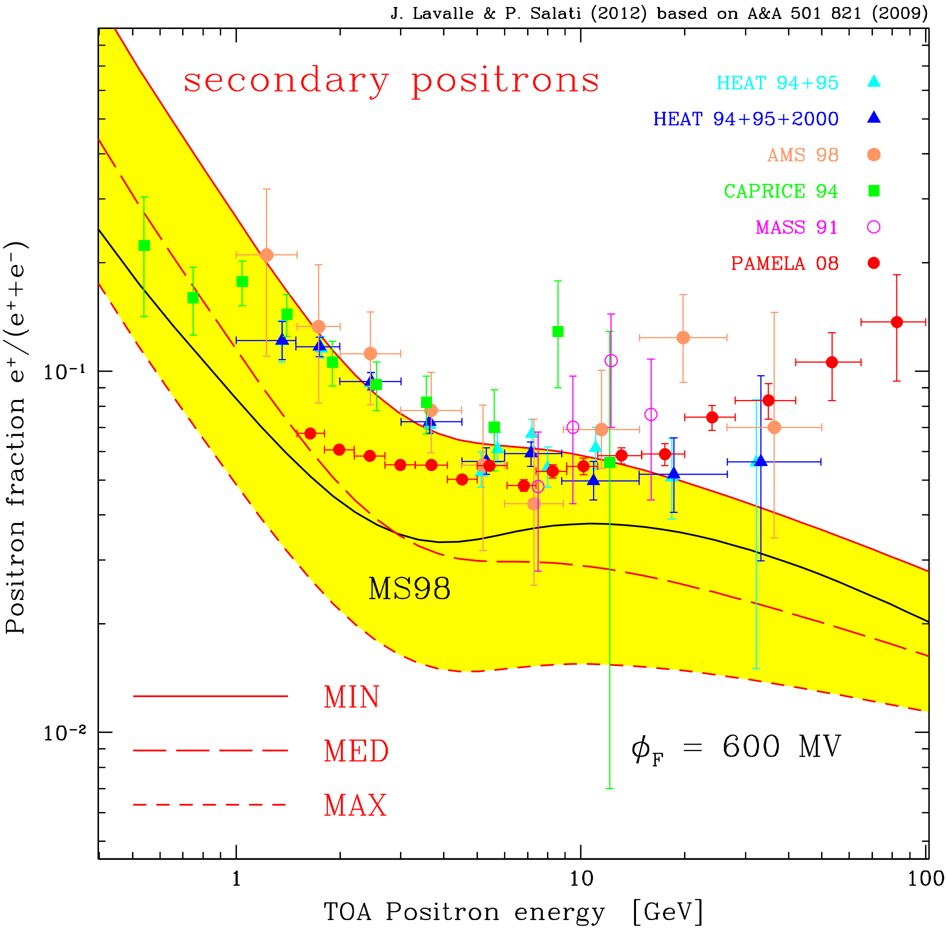

Figure 4.7: A compilation of positron fraction results as measured by several experiments superimposed to the expected background of secondary positrons. The bounds of the band follow the extreme models of propagation parameters while a 600 MV Fisk potential has been applied for the Solar modulation[109].

measured to capture the identity of DM. Finally, ID experiments are based on the idea that DM particles pair-annihilate producing SM ones that would manifest as anomalies in the spectra of rare CR components.

- Despite the different assumptions of the search approaches, they still have some common hypotheses; namely that at least part of the DM content is made up of unknown particles that have not been identified yet, and that there is some type of interaction that takes place between DM particles and SM ones, regardless how weak it could be.

- Collider searches are favored with several advantages including the kinematic accessibility for further investigation, the high luminosity offered by the colliders, and the ability to limit and account for background signals. However, they are also challenged with several obstacles. For example, a collider experiment can not tell if a detected particle is a DM candidate or not. Thus, it is still necessary to implement other search approaches in assessing such results.

- DD experiments are challenged by high background signals and a low event rate. However, the potential of detecting annual modulation due to a DM signal gives them an advantage in identifying anomalous events with more confidence. Nevertheless, with the exception of DAMA, no other experiment has been able to detect any modulation.

- Although ID of DM is faced by many challenges due to the large number of variables where all the astrophysical signals become backgrounds, it is, nevertheless, the most ambitious of approaches. Success of ID experiments will not only enhance our knowledge of DM identity, but it will also help to accurately map the DM distribution in the Universe.

- Each search technique of ID is more optimal for certain CR components. It is thus extremely important to keep diversifying such techniques in order to maximize our chance for capturing DM. They should also be applied simultaneously to collect more pieces of the DM puzzle.

- To take advantage of all search approaches currently employed, several groups have been formed to specifically compare results from different approaches. In addition, they have developing algorithms to identify all potential sets of constraints for DM candidates (see References [81, 82] and references within for more details). This would offer guidance to future research and experimentation, thus accelerating advances on these fronts.

In the next Chapter, we will go deeper into the ID of DM. In particular, we will review recent antiproton results from AMS-02 and the difficulties preventing researchers from optimizing the use of these results. Finally, we will review potential solutions outlined by recent studies with some actionable steps.

Chapter 5

Antiprotons as a Probe for Dark Matter

5.1 Cosmic Rays

Primordial Cosmic Rays are particles that have been produced in their astrophysical sources. On their way to the top of the Earth's atmosphere (TOA), they are affected by their propagation in both the galactic and extragalactic space. Even though there is no definite altitude that marks the TOA, it has become customary to consider the TOA to be at an altitude of ~ 40 km (cf. [111]). Only when primordial CRs reach the TOA are they called *Primary Cosmic Rays*. One way to look at CRs is to consider them as a universal sample that indeed has a similar elemental abundance to that observed in the solar system, as can be seen in Figure 5.1.

In the figure, it can be seen that the most dominant charged components in primary CRs are protons ($\sim 85\%$) followed by helium nuclei ($\sim 12\%$), while all other charged components represent less than 3%. It can also be seen that there are some obvious differences between the abundances of lithium, beryllium, and boron in that they are clearly more abundant in CRs than they are in the solar system. The same goes for the element group below iron ($Z < 26$). This is attributed to the fragmentation of heavier elements on their way to the TOA, which increases the abundance of their product nuclei (cf.[111]). Boron is expected to only be produced secondarily via CR spallation. In addition, the boron-production cross sections from carbon and oxygen are well studied. Thus, the Boron-to-Carbon ratio (B/C) is widely used to understand CR propagation in the galactic environment, and to constraint models associated with it. Eventually, it is utilized in determining the production of secondary antiprotons in the interstellar medium (ISM) (cf.[112]).

Most of the primary CRs with energies $< 10^6$ GeV are supposedly

Figure 5.1: The elemental abundances for both primary CRs and the solar system, for atomic numbers $1 \leq Z \leq 28$[111].

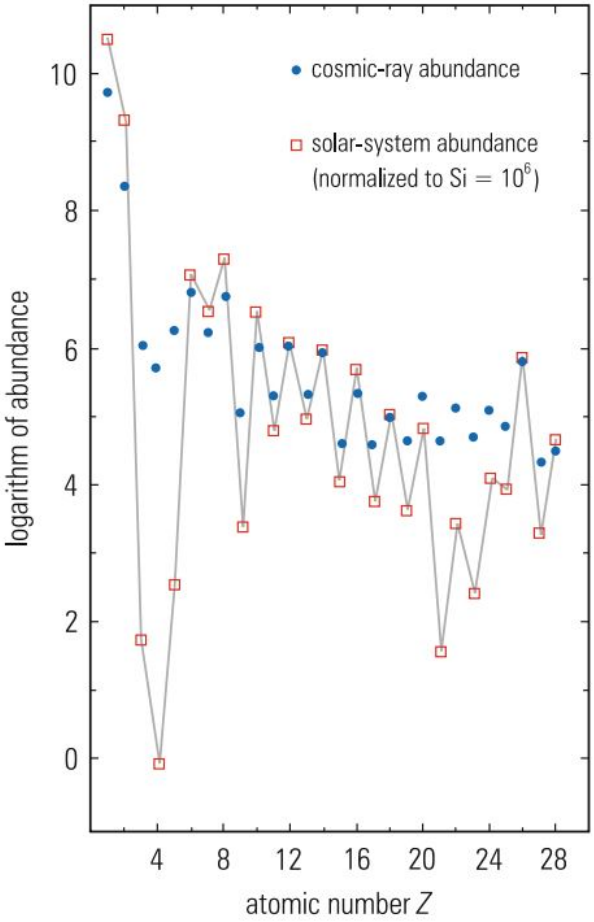

produced within Our Milky Way. Above that energy, however, the spectrum becomes steeper while it again starts to slightly flatten at about 10^{10} GeV, and it finally reaches a cutoff at 6×10^{10} GeV (see Figure 5.2). Let us now outline the potential causes behind this spectrum shape. It is believed that particles that have energies higher than 10^6 GeV can escape from the Milky Way. Thus the spectrum steeply decreases at these energies. Another potential cause might be that supernova explosions do not produce energies higher than 10^6 GeV. Consequently, if a sizable contribution of CRs is produced in these explosions, it is to be expected that the flux would decrease above that energy. As for the final cutoff,

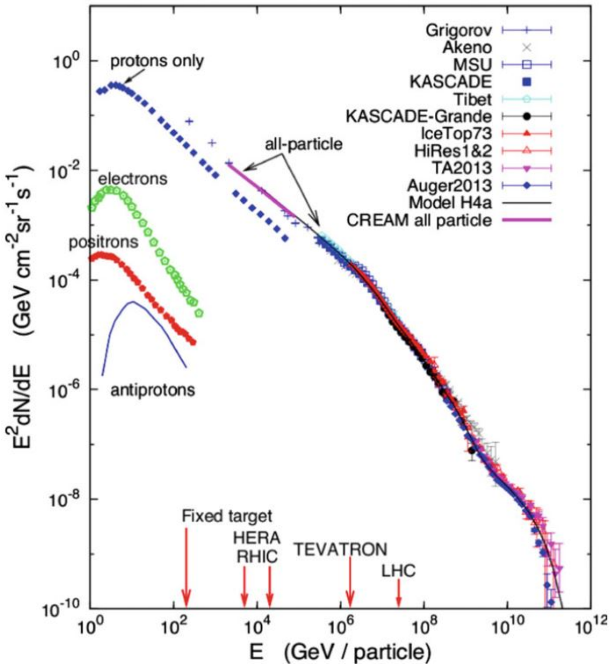

Figure 5.2: The collective primary CRs spectrum as has been measured by several experiments[111], where as the contributions from electrons, positrons, and antiprotons are also indicated based on measurements by the PAMELA experiment[113].

it might be due to the escape of heavier nuclei, such as iron, from the galaxy. The reason could also be that events that produce particles with such high energies are only of extragalactic origins (cf.[111]).

Antiparticles like positrons and antiprotons are very rare in CRs, and belong to what is called *Secondary Cosmic Rays*, which are CRs produced via the interactions between primary CRs and the ISM. While antiprotons are usually produced in nuclear collisions (as will be further discussed in §5.4), positrons are pair-produced by high-energy photons. Even though CRs have been discovered more than a century ago, there are only theories about their origins but no conclusive evidence. Nevertheless, there are a lot of potential candidates such as active galactic nuclei, quasars, and supernovae. There are some challenges that face any theory trying to track different CR components to their origins. One of these is that while neutral components, like neutrinos and photons, travel in space undisturbed by the magnetic fields they encounter, charged CR components are influenced by any irregularity in magnetic fields along their paths. Thus, neutral CRs can be tracked back to their original direction whereas charged CRs travel along elaborate trajectories that could look very random when there is little information about the magnetic fields that shaped them. Consequently, the abundances shown in Figure 5.1, and therefore the corresponding fluxes, are not constant. They depend on several factors. Perhaps the most dominant one, especially at low energies, is the solar cycle. The sunspot cycle repeats every 11 years. Nucleons with low energies are largely affected by the magnetic fields of the Sun and the Earth. The solar activity, in particular, reduces their momenta and the intensity of their flux at the TOA as its magnetic field prevents their reaching the Earth (cf.[111]). It thus alters their spectrum. Accordingly, the spectrum at the TOA, $d\Phi_{\mathrm{TOA}}/dE_{k,\mathrm{TOA}}$, and the LIS (Local Interstellar Spectrum), $d\Phi_{\mathrm{LIS}}/dE_{k,\mathrm{LIS}}$, are related by [114]

$$\frac{d\Phi_{\mathrm{TOA}}}{dE_{k,\mathrm{TOA}}} = \frac{p^2_{\mathrm{TOA}}}{p^2_{\mathrm{LIS}}} \frac{d\Phi_{\mathrm{LIS}}}{dE_{k,\mathrm{LIS}}}, \qquad E_{k,\mathrm{LIS}} = E_{k,\mathrm{TOA}} + |Ze|\phi, \tag{5.1.1}$$

where p is the momentum, Ze is the electric charge of the particle, and ϕ is the Fisk potential. According to this, both protons and antiprotons will be identically affected.

While the solar modulation has a large effect on the CR flux, its influence is mostly limited to CR particles with energies below 10 GeV. The correlation is such that the flux is at its lowest when the sunspot cycle is at its maximum and vice versa, which can be seen in Figure 5.3. At the same time, the solar activity in itself produces particles—mostly protons and electrons—that can be measured at the Earth. They are usually referred to as solar wind. However, these particles typically have low energies of the MeV scale. They either get captured by the magnetic field of the Earth in what is known as the Van Allen belts or get absorbed at the top layers of the Earth's atmosphere (cf.[115]).

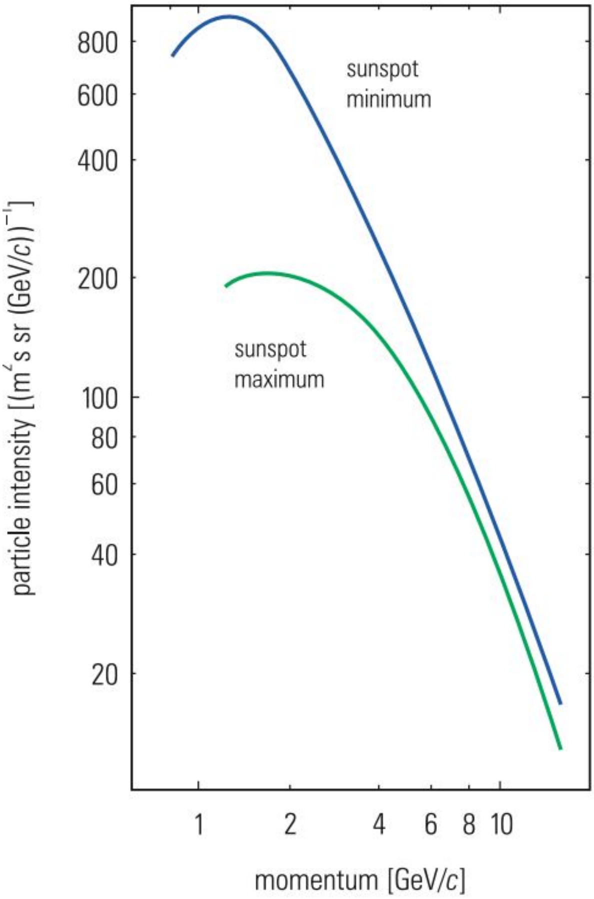

Figure 5.3: The effect of the primary spectrum modulation caused by the 11-year solar cycle[115].

What complicates things even further is that it is not enough to understand the galactic magnetic fields—around which there is already a lot of uncertainty—but it is also necessary to track back the time evolution of these magnetic fields. That is simply because the sources of these CRs could be further than 50 Mpc ($\sim$ 163 million light years). Moreover, the delay of charged particles with respect to their neutral counterparts mean that the time evolution of the magnetic fields needs to be mapped for even further back epochs (cf.[111]).

No primary CRs can reach sea level. This is simply because the thickness of the atmosphere has a depth of about 27 radiation lengths for photons and electrons, and a depth of 11 radiation lengths for hadrons. Moreover, it is even thicker for inclined angles, such that its thickness increases with $1/\cos\theta$, where θ is the zenith angle. Subsequently, at sea level, it is only possible to detect the cascades of secondary CRs that result from the interaction of primary CR particles with the atmosphere; an example of which can be seen in Figure 5.4 (cf.[115]). On the other hand, the last two decades have witnessed substantial progress in the field of CRs, in particular, when it comes to the antimatter components and their implications regarding DM. More progressive and elaborate experiments have been designed to measure the CR components spectra with unprecedented precision (cf.[112]). Figure 5.5 shows an example compilation of some of these recent measurements.

Secondary CRs are utilized to pursue DM where some studies focus on charged rare components while others focus on neutral products. Each study class has a different set of advantages along with its challenges. For example, if there is a signal in the charged antimatter components of CRs, we can expect it to be stronger due to its buildup over time, since they encounter much more interactions along the way. In addition, since antimatter components are predominantly secondary, they are rarer than matter components. Thus the signal-to-background ratio can be expected to be higher. The antiprotons component is one of the most pursued signals. The threshold energy for producing an antiproton is $7m_p \approx 6.5$ GeV, where m_p is the proton mass. In this scenario, the produced antiproton would have an energy of $m_p \sim 0.94$ GeV (*i.e.* at rest). Antiprotons can also be produced as the final stable products via the decay of antineutrons and antihyperons (cf.[112]). But even now, most of our knowledge of an-

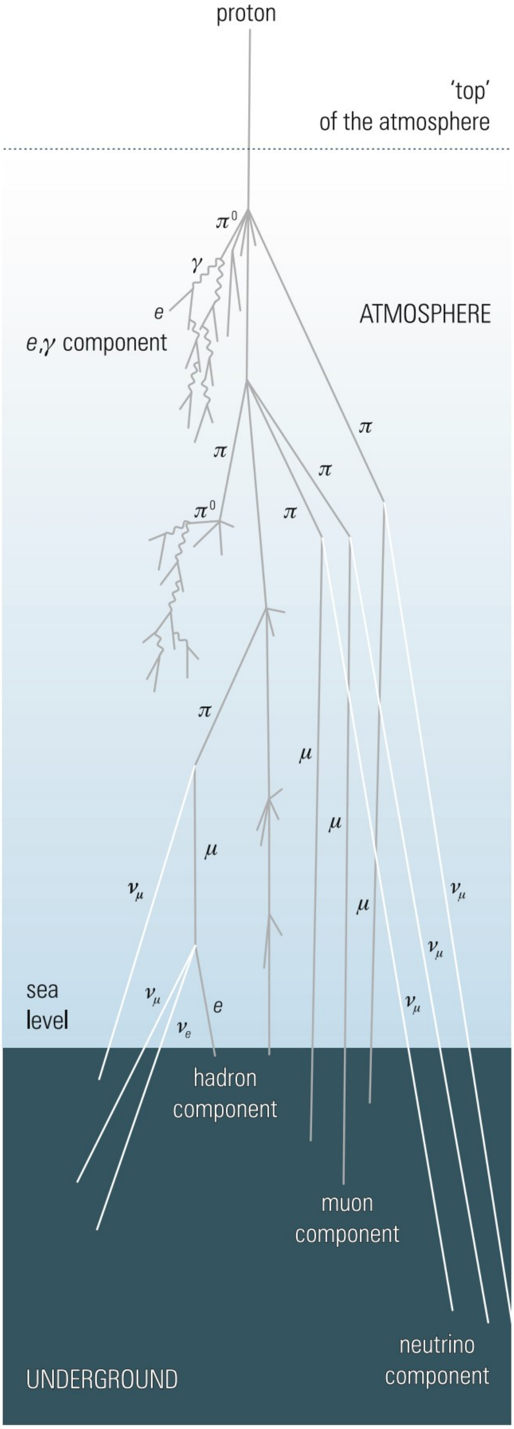

Figure 5.4: An example of the particle cascades that primary CRs make while traveling in the atmosphere[115].

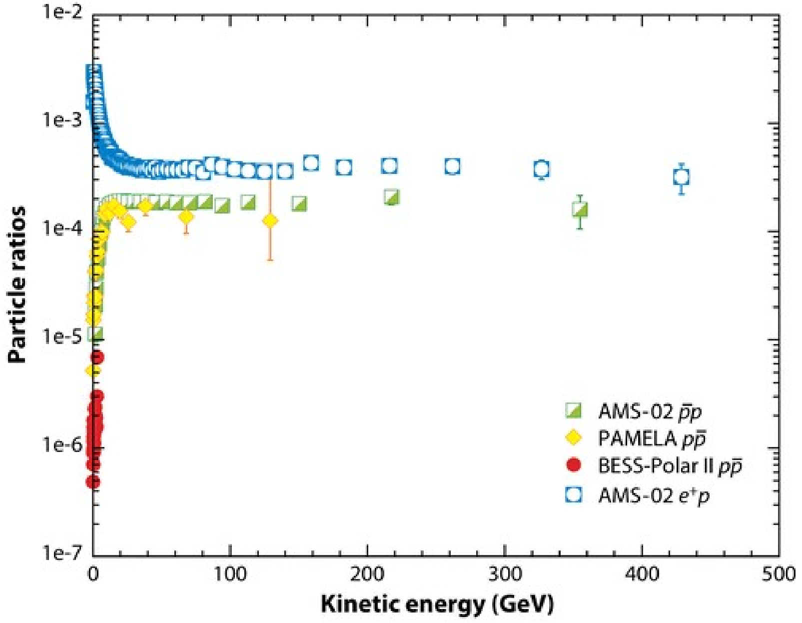

Figure 5.5: A compilation of the spectral intensities ratios for positrons and antiprotons to that of protons based on recent measurements of CRs from several experiments[112].

tiproton production is based on parameterizations drawn from some *pp* datasets that mostly date back to before 1980. Moreover, it has recently been found that the primary CR spectra of proton and helium change behavior at a rigidity between ∼ 200 and 300 GeV[116–118]. Naturally, this will also affect the secondary antiproton production at these energies. However, these old parameterizations have been carefully enhanced by use of two recent datasets from the NA49 experiment at CERN [119]. They have also been extended to include other production channels [120, 121].

Cosmic Ray Antiprotons

There are a few density profiles for DM distribution that depend mainly on the galaxy class. For the Milky Way, the following Navarro-Frenk-

White profile [122] is often adopted [123]

$$\rho(r) = \frac{\rho_0}{(r/r_s)(1+r/r_s)^2}, \tag{5.1.2}$$

where ρ_0 is a normalization parameter, r is the distance from the galactic center, and r_s is the scale radius. The annihilation and decay of DM particles supposedly produce primary quarks, gauge bosons, or leptons. Antiprotons are then thought to be produced either from the hadronization of quarks or gauge bosons, or via electroweak radiation of leptons (cf.[124]). On one hand, the source term of the antiproton flux due to DM annihilation within the galaxy is estimated by [125]

$$q_{\bar{p}}^{(\mathrm{DM})}\left(\boldsymbol{x}, E_{\mathrm{kin}}\right) = \frac{1}{2}\left(\frac{\rho(\boldsymbol{x})}{m_{\mathrm{DM}}}\right)^2 \sum_j \left\langle\sigma v\right\rangle_f \frac{dN_{\bar{p}}^f}{dE_{\mathrm{kin}}}, \tag{5.1.3}$$

where m_{DM} is the DM mass, $\rho(\boldsymbol{x})$ the DM density profile, $\left\langle\sigma v\right\rangle_f$ the thermally averaged annihilation cross section for the SM final state f such that $\mathrm{DM}+\mathrm{DM} \to f+\bar{f}$, and $dN_{\bar{p}}^f/dE_{\mathrm{kin}}$ is the corresponding antiproton energy spectrum per DM annihilation. Finally, the factor 1/2 is specific to Majorana fermion DM. On the other hand, the source terms for secondary CRs are estimated by [126]

$$q_i^{\mathrm{sec}}(T) = \sum_j 4\pi \int dT' \left[n_{\mathrm{H}} \left(\frac{d\sigma}{dT}\right)_{j\mathrm{H}\to i} + n_{\mathrm{He}} \left(\frac{\sigma}{dT}\right)_{j\mathrm{He}\to i} \right] \Phi_j^{\mathrm{IS}}(T'), \tag{5.1.4}$$

where $\Phi_j^{\mathrm{IS}}(T')$ is the interstellar flux of the corresponding incoming CR species given as a function of kinetic energy per nucleon T', T is the kinetic energy per nucleon of the outgoing secondary particle, and $d\sigma/dT$ is the differential cross section including all production processes.

The cross section measured directly by experiments is not the energy-differential cross section $d\sigma_{ij}/dT_{\bar{p}}$, for the ith CR component and the jth ISM component, but the fully differential cross section usually given in a Lorentz invariant form as follows [127]

$$\sigma_{\mathrm{inv}} = E\frac{d^3\sigma}{dp^3}\left(\sqrt{s}, x_{\mathrm{R}}, p_{\mathrm{T}}\right), \tag{5.1.5}$$

where E and p are the total antiproton energy and momentum, respectively, and p_{T} is the transverse momentum. The differential cross section can then be expressed in terms of LAB frame variables and integrated over the solid angle, Ω, to get the energy-differential cross section as follows [127]

$$\frac{d\sigma_{ij}}{dT_{\bar{p}}}\left(T, T_{\bar{p}}\right) = p_{\bar{p}}\int d\Omega\sigma_{\mathrm{inv}}^{(ij)}\left(T_i, T_{\bar{p}}, \theta\right). \tag{5.1.6}$$

The pp channel produces about 50%-60% of secondary antiprotons over the whole spectrum, and the pHe and Hep channels produce around 10%-20% each, while heavier-nuclei channels have a negligible contribution of only a few percents.

5.2 AMS-02 Antiprotons Results

Since May 2011, the Alpha Magnetic Spectrometer (AMS-02) has been operating on the International Space Station (ISS) as a multi-purpose CR detector. It is also planned to continue until the end of the ISS lifetime. The magnetic-spectrometer detector relies on a particle identification system that employs a signal coinciding technique from several sub-detectors. The time-of-flight (TOF) system accommodates speeds up to $\beta \approx 0.8$. The 0.15 T magnetic field has a solenoidal configuration. The detector uses Cherenkov (RICH) counters for velocity measurements. It also utilizes a TRD (transition radiation detector) for suppressing lighter particles such as kaons, pions, and electrons. Figure 5.6 shows an outline of the main parts of the detector [128].

It is by far the most advanced detector for charged CR fluxes. The AMS-02 has measured the electron, positron, proton, and antiproton fluxes. It has also confirmed the existence of a positron excess signal above 10 GeV, which has been previously detected by both PAMELA and FERMI (cf.[124]). The AMS-02 measurements also included the B/C ratio with an extended rigidity range. This ratio is very useful for the determination of propagation parameters between galaxies. This is because boron is only produced secondarily in CRs, while carbon is produced primarily (cf.[126]). The new measurements of $\bar{p}/p$ ratio by AMS-02 [129] have decreased uncertainties to about 5%, in addition to extending the range of energies covered. Not only will this help in estimating CR propagation parameters more accurately, but it will also facilitate the detection of any potential exotic source of antiprotons. In principle, AMS-02 can access potential signals of antiprotons from DM candidates of masses up to several hundred GeV (cf.[130]).

In agreement with previous PAMELA [116] and CREAM [131] measurements, the new AMS-02 measurements of proton and helium spectra show that their primary fluxes cannot be described by a simple power law. They display a spectral hardening at rigidity $\mathcal{R} \sim 400$ GV, as can be seen in Figure 5.7. A new parameterization of interstellar proton and helium fluxes uses a sum of two power laws [126]

$$\Phi_i^{\mathrm{IS}}(T) = \left(\frac{T}{T+b}\right)^c \left(A_1 T^{-\gamma_1} + A_2 T^{-\gamma_2}\right) , \tag{5.2.1}$$

where γ_1 and γ_2 are parameters that can be fitted with observations.

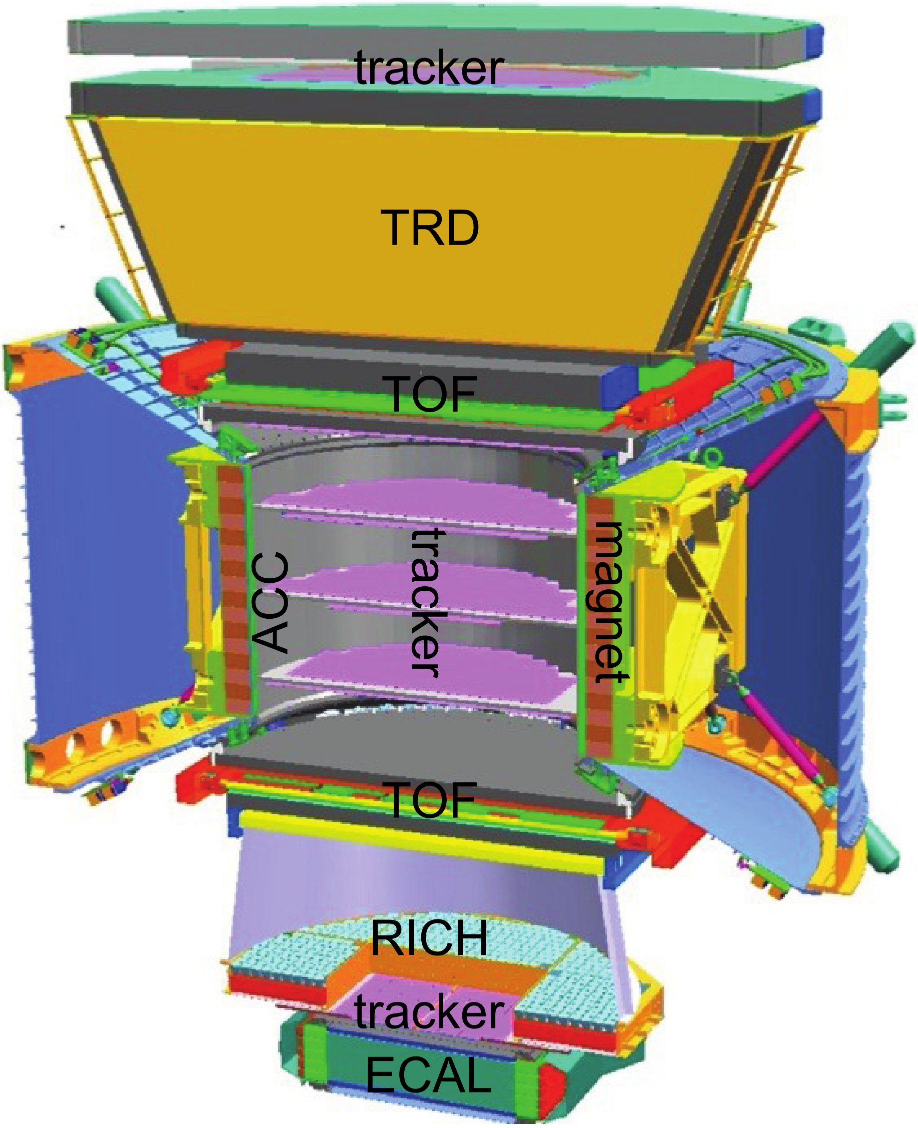

Figure 5.6: An outline of the main operating parts of the AMS-02 CR-detector [128].

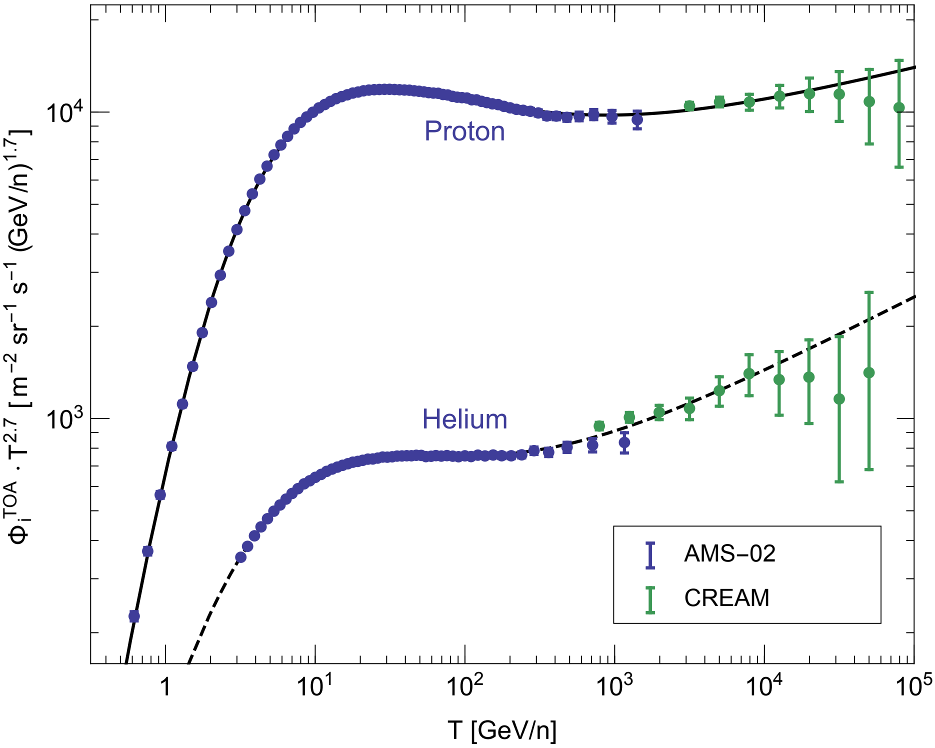

Figure 5.7: The hardening of proton and helium spectra as measured by both AMS-02 and CREAM, superimposed on the fit functions given by (5.2.1) [126].

During the last decade, the AMS Collaboration has confirmed the existence of an excess in the positron fraction signal above 0.5 GeV [132], which supports results from previous measurements from different experiments. Even though many attempts have been made to interpret this positronic excess as a DM signal, other astrophysical explanations are currently more favored (cf.[124]). In addition, in 2016, the collaboration has released their antiproton results so far. It represents the most precise antiproton spectrum so far covering the rigidity range from 1 GV to 425 GV. The data included 2.42×10^9 proton events and 3.49×10^5 antiproton ones [129]. Even though the signal is consistent at energies below

100 GeV, there is a bump in the spectrum in the range $\sim 100-260$ GeV. There are several potential sources for this excess signal, including: (*i*) pulsar wind nebulae, (*ii*) primary CRs collisions with gases of supernova remnants (SNRs), and (*iii*) DM annihilation [133].

There have been several interpretations of the $\bar{p}/p$ AMS-02 data in terms of annihilation of DM particles of TeV masses. Even though several works have demonstrated the lack of any unambiguous excess in the AMS-02 signal after all uncertainties have been accounted for, some models that are consistent with the data seem to be barely on the edge of the uncertainty band (see Reference [126] and references within). The signal has been shown however to be fitted much better with the introduction of DM annihilation to $b\bar{b}$ such that $m_{\mathrm{DM}} \approx 80$ GeV$/c^2$ and $\langle\sigma v\rangle \approx 3 \times 10^{-26}$ cm^3/s, which is consistent with the preferred range of DM masses and annihilation cross sections shown in Figure 5.8 [125]. However, after including the AMS-02 measurements of proton and helium spectra, and the B/C ratio into the calibration of propagation parameters, in addition to including all other relevant sources of uncertainty, the significance of the signal has dropped dramatically from over $5\,\sigma$ to a global significance of $1.1\,\sigma$ [134]. DM particles are thought to produce SM particles either directly or via a mediator. It has been shown that the AMS-02 signal favors the mediator scenario [133], which is also more consistent with previous constraints.

When the AMS-02 measurements were first released, there has been an initial excitement [125, 135]. Nevertheless, the signal needed further investigation. On one hand, while DM could have a contribution to the positron excess, it remains unclear what the origins of the signal are. On the other hand, the antiproton signal could be explained away en-

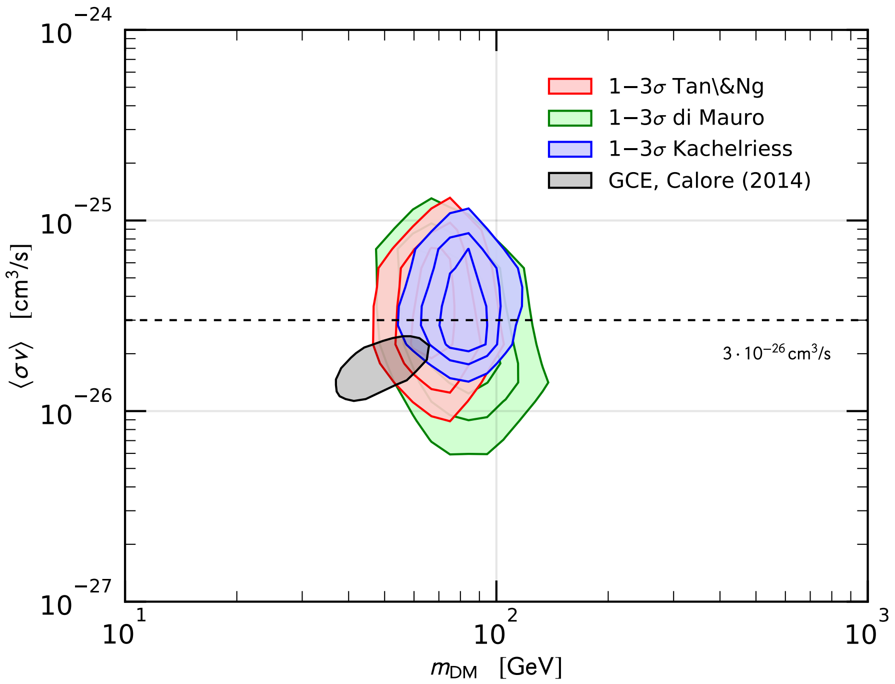

Figure 5.8: Constraints on DM mass and annihilation cross section based on several parameterizations of antiproton-production cross sections; in addition to those based on the galactic center γ-ray excess [125].

tirely by DM annihilation and/or decay. However, it is uncertain. In addition to direct antiproton production in collisions of CRs and ISM, antiprotons are also produced via decay of intermediate hyperon decays, namely $\bar{\Lambda}$ and $\bar{\Sigma}^{-}$, and the eventual decay of antineutrons. There also exists a tertiary antiproton component due to inelastic scattering of secondary antiprotons on ISM (cf.[126]). Nevertheless, several studies that attempt to explain both signals have been released (see Reference [136] and references within).

There are still a lot of controversy surrounding the signal based on the analysis approaches adopted. While some affirm the existence of a potential signal with a statistical significance in the range of $3\,\sigma - 5\,\sigma$

[123, 137], others stress that accounting for uncertainties eliminates this significance and brings it below $2\,\sigma$, making it consistent with a secondary background [138]. Currently, no conclusion can be solidly drawn due to several sources of uncertainties related to the background. Even though several studies have shown that the measured flux is compatible with a secondary origin, the observed slope is at the edge of the uncertainty band, leaving a lot of room for improvement. Thus, the conclusion remains that there is no definite antiproton excess that can be attributed to exotic astrophysical sources (cf.[124, 130]).

5.3 Uncertainties

Despite these new accurate measurements, conclusions are still hindered by astrophysical uncertainties. The antiproton flux measured by satellite-based experiments results from the diffuse production of antiprotons in the Milky Way environment and their subsequent propagation to the location of these experiments. Therefore, the factors that influence the computation of the secondary antiproton background are mainly: the primary fluxes of protons and helium nuclei, the antiproton-production cross sections in collisions of primary CRs and ISM, and the propagation parameters [124].

Secondary CR nuclei are produced after fragmentation of the parent nuclei of CR and ISM through their collision. Therefore, secondary-to-primary particle ratio, such as the B/C ratio, is a very important tool for constraining the propagation parameters of charged particles in the galactic environment (cf.[139]). In frameworks of CR propagation, parameterization of primary sources are performed first before calculating the resultant fluxes of all primary and secondary CR species. It is worth noting that a single framework can unify the propagation of all these species (cf.[126]). The propagation of charged CRs is usually described by the equation [139]

$$\frac{\partial \psi}{\partial t} = \nabla . \left(D_{xx} \nabla \psi - \boldsymbol{V} \psi \right) + \frac{\partial}{\partial p} p^2 D_{pp} \frac{\partial}{\partial p} \frac{\psi}{p^2} + \frac{\partial}{\partial p} \left[b\psi + \frac{p}{3} \left(\nabla . \boldsymbol{V} \right) \psi \right] - \frac{\psi}{\tau} + q. \tag{5.3.1}$$

The CRs are assumed to propagate in a diffusive cylindrically-symmetric halo of radius R_h and a half-height z_h that depends on the magnetic field extension. In the above equation, the first term is represented by D_{xx}, the spatial diffusion coefficient, while the second term is the advection velocity. It is assumed that $\boldsymbol{V}$ increases linearly in the z-direction. The third term represents the stochastic reacceleration parameterized by the coefficient D_{pp}. The following two terms (fourth and fifth) represent energy losses, while the sixth term represents fragmentation and/or decay. Finally, the last term is the source function. The diffusion coefficient can be expressed as follows [123]

$$D_{xx}(R) = \beta D_0 (R/4 \text{ GV})^{\delta}, \tag{5.3.2}$$

where $\beta \equiv v/c$, R is the rigidity, and δ is the diffusion index related to magnetohydrodynamic turbulence in the ISM. Meanwhile, the diffusion coefficient in momentum space, that describes the diffusive reacceleration is given by [140]

$$D_{pp} \propto \frac{R^2 v_A^2}{D_{xx}(R)}, \tag{5.3.3}$$

where v_A is the Alfvén speed; that is, the propagation speed of the hydromagnetic waves in the ISM plasma.

After their production, antiprotons travel in the galactic environment before reaching Earth. During that, they are subject to many processes that affect the final signal, such as pair annihilation with protons, energy losses, tertiary production, and diffusive reacceleration. In addition, the propagation parameters that determine diffusion and convection are usually represented in three sets: MIN, MED, and MAX, which are defined to minimize or maximize the hypothetical primary DM antiproton flux at Earth (cf.[124]). Before the recent measurements from AMS-02, it has been usual to use benchmark propagation models based on the B/C ratio to derive the limits of CR DM. However, this has always been a source of uncertainty in any consequent conclusions. In additions, the recent AMS-02 measurements have in fact indicated that heavy nuclei, such as B and C, propagate differently from light nuclei, such as p and $\bar{p}$, which suggests that applying the benchmark models as referred to above will certainly add a bias to the analysis of antiprotons (cf.[125]). The new AMS-02 measurements of primary fluxes (*e.g.* He, C, O [141]) and secondary fluxes (*e.g.* Li, Be, B [142]) are thus crucial for updating CR propagation parameters to be more consistently constrained. When antiprotons finally reach the vicinity of the Earth, they are affected by solar modulation while penetrating the heliosphere. This modulation is parameterized by the Fisk potential, ϕ_F, whose value depends on ever-changing parameters associated with solar activity, which in turn depends on the time of observation. Thus, the Fisk potential is only a descriptive value of a complex phenomenon, and is inherently uncertain [124].

As for the secondary antiproton background, it is produced from collisions of primary CRs with ISM which are both made up mainly of protons and helium nuclei. Heavier nuclei have a negligible contribution. The AMS-02 has also measured the primary spectra of both protons and helium with superior precision. The fluxes of protons and helium nuclei have been measured up to 1.8 and 3 TeV/nucleon, respectively, and proved what has previously been detected by PAMELA; namely, that there is a hardening above ~ 300 GeV for both spectra. This means that the spectra cannot be described by a single power law, thus adding an uncertainty band around the $\bar{p}/p$ ratio [124].

In terms of antiproton-production cross sections, it is crucial to estimate them for the production channels of pp, and pHe, at least. Since these channels produce about 97% of the total secondary antiproton yield. It is worth mentioning that previously it was assumed that antineutrons were equally produced owing to isospin symmetry. These antineutrons would eventually decay doubling the final yield of antiprotons. However, it has been pointed out recently that antineutron production cross sections might be larger by up to 50% in comparison to these of antiprotons. This also adds uncertainty on the recent measurements due to the scarcity of data for pp collisions. What makes it even more challenging is that pHe datasets are almost nonexistent; and their cross sections are estimated through semi-empirical parameterizations. Some models even suggest the existence of a primary antiproton component that acts as an additional background (cf.[124]).

All these factors accumulate to an uncertainty that ranges between 20% and 50% (depending on the energy) on the recent $\bar{p}/p$ measurements [124]. Most of the uncertainty on the $\bar{p}$-production cross sections manifests in the channel $p + p \to \bar{p} + X$, which leads it to affect all other production channels since they are derived from scaling the pp cross sections [127]. We are now at a point where it is crucial to obtain more accurate and comprehensive measurements of antiproton-production cross sections before we can trust any potential signal that the recent or future AMS-02 measurements might suggest (cf.[125, 138]). Figure 5.9 shows the effect of each of the above-outlined sources of uncertainties. The collective effect of all these uncertainties is that the new $\bar{p}/p$ measurements can be explained entirely by the ordinary astrophysical flux, as can be seen in Figure 5.10.

Antiproton signatures remain the most promising possibility for ID of DM since most of the uncertainties could be further optimized by performing accurate measurements of the associated parameters, whereas positrons and γ-rays have far more complicated backgrounds that will take more efforts to track, and neutrinos are challenged by difficulty of detection (cf.[124]). It can be seen from Figure 5.10 that the recent $\bar{p}/p$ measurements are consistent with a secondary origin, at the level of $1.2\,\sigma$, without the need for primary sources. However, there is still room for improvement due to the large uncertainties in the estimation of the secondary background. Thus, it is crucial to minimize these uncertainties. Fortunately, upcoming AMS-02 data will enhance our estimates for propagation parameters and solar modulation. Thus, uncertainties in antiproton-production cross sections are about to become the largest hurdle in identifying any potential exotic antiproton signal. Hence, there is an urgent need to dedicate experimental efforts to precise measurement of antiproton-production cross sections [126, 130].

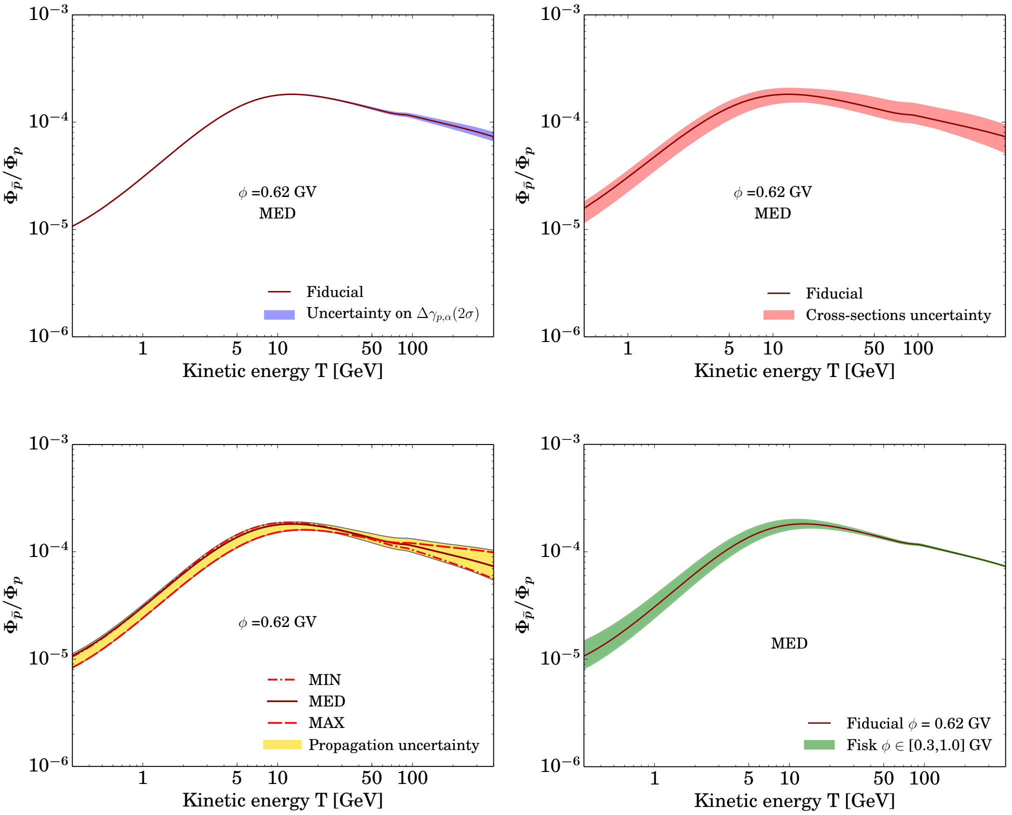

Figure 5.9: Sources of uncertainty of secondary antiproton signal. The upper left panel shows the uncertainty from the spectra slopes of protons and helium nuclei as a blue band. The upper right panel shows the uncertainty in antiproton-production cross sections as a red band. The lower left panel shows the uncertainty due to propagation parameters as a yellow band. Finally, the lower right panel shows the uncertainty due to solar modulation as a green band[124].

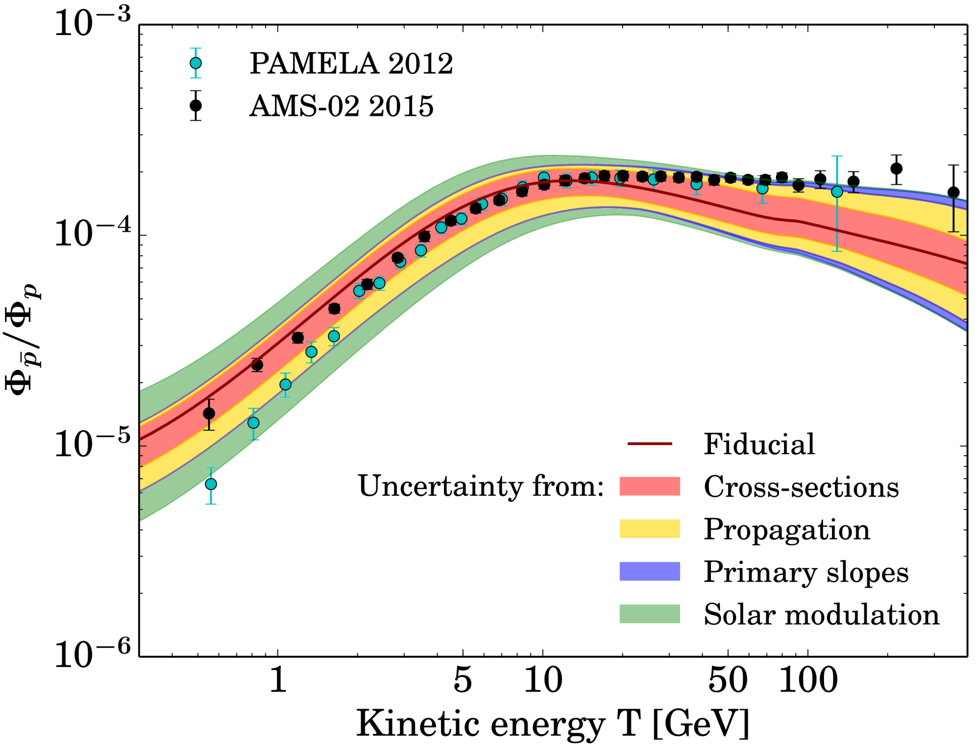

Figure 5.10: The accumulative uncertainty band on the expected secondary $\bar{p}/p$ ratio, superimposed to the datapoints from both PAMELA and AMS-02[124].

5.4 Antiproton Production in Hadronic Collisions

The invariant differential cross section for antiproton production in proton-proton collisions is given by

$$f = E\frac{d^3\sigma}{dp^3} = \frac{E}{\pi}\frac{d^2\sigma}{dp_{\mathrm{L}}dp_{\mathrm{T}}^2}\,, \tag{5.4.1}$$

where E is the antiproton energy, p_L is the longitudinal momentum, and p_T is the transverse momentum. There are several production channels for antiprotons, they are summarized as

$$\sigma = \sigma_{\bar{p}} + \sigma_{\bar{n}}\,, \qquad \sigma_{\bar{p},\bar{n}} = \sigma^0_{\bar{p},\bar{n}} + \sigma^\Lambda_{\bar{p},\bar{n}}\,. \tag{5.4.2}$$

In the above equation, the first term represents direct antiproton production, while the second represents eventual decays of antineutrons. In addition, each of these terms is separated into a prompt-production term and a hyperon-decay term [130].

It has before been assumed that antiprotons and antineutrons are produced equally in hadronic collisions. Thus, the contribution of the eventual decay of antineutrons has been assumed to be equal to antiprotons from prompt production. A potential asymmetry has been noted recently [120]. It was argued that isospin effects might result in a favored production of $\bar{p}n$ or $\bar{n}p$ according to the colliding particles, thus skewing the ratios one way or the other. An instance of this asymmetry was found to be true at $\sqrt{s} = 17.2$ GeV [143]. However, it was also argued that these effects disappear at higher energies [144]. Existing experimental data was treated to determine the ratio Δ_IS as a function of energy [130]. The resulting fit is shown in Figure 5.11. It can be seen that the fit indeed approaches zero at higher energies. Nevertheless, isospin effects might still skew our estimation of the overall antiproton yield. The invariant cross section given in (5.4.1) should thus be rewritten as [130]

$$f = f^0_{\bar{p}}(2 + \Delta_\mathrm{IS} + 2\Delta_\Lambda)\,, \tag{5.4.3}$$

where $\Delta_\mathrm{IS} = f^0_{\bar{n}}/f^0_{\bar{p}} - 1$ is the isospin enhancement factor and $\Delta_\Lambda = f^\Lambda_{\bar{p}}/f^0_{\bar{p}}$

such that $f^{\Lambda}_{\bar{p}} = f^{\Lambda}_{\bar{n}}$.

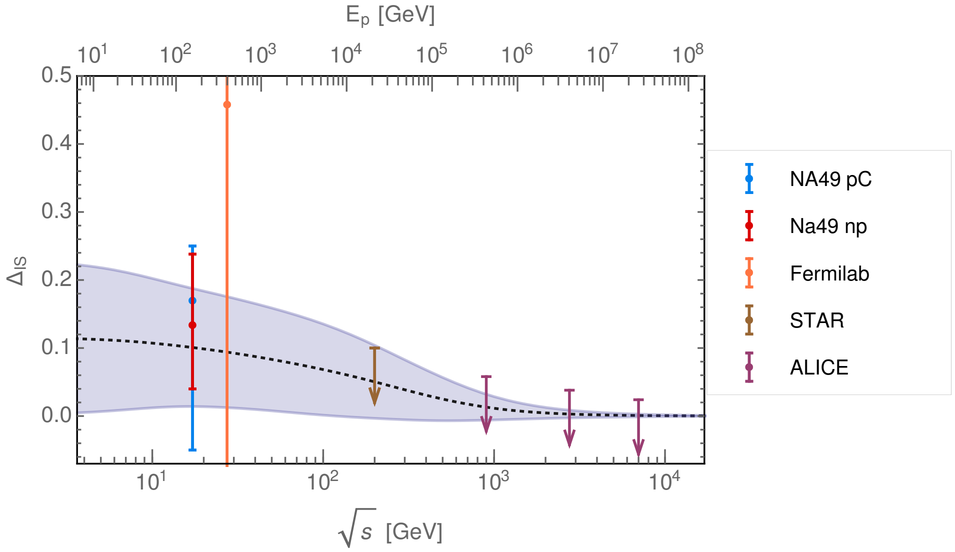

Figure 5.11: The isospin factor as extracted from different datasets. The band of uncertainty associated with the applied fit parameterization is also shown [130].

A significant fraction of the antiproton yield in hadronic scattering processes is produced via antihyperons, $\bar{\Lambda}$ and $\bar{\Sigma}^-$, decay. This contribution cannot always be tracked in accelerator experiments. In fact, recent experiments apply a feed down to account for it. However, older experiments did not apply such a correction. Hence, integration of older and newer datasets becomes more complicated. It has also been found that the multiplicity of hyperon production in proton-proton scattering increases with energy, which implies that antiprotons produced via hyperon decays increase as well. The ratio of hyperon-induced antiprotons can be obtained from [130]

$$\Delta_{\Lambda} = \frac{\bar{\Lambda}}{\bar{p}} \times \mathrm{Br}\left(\bar{\Lambda} \to \bar{p} + \pi^+\right) + \frac{\bar{\Sigma}^-}{\bar{p}} \times \mathrm{Br}\left(\bar{\Sigma}^- \to \bar{p} + \pi^0\right) , \qquad (5.4.4)$$

where $\frac{\bar{\Lambda}}{\bar{p}}$ and $\frac{\bar{\Sigma}^-}{\bar{p}}$ are the hyperon-to-directly-produced ratios. Since there are no experimental data on the ratio $\frac{\bar{\Sigma}^-}{\bar{p}}$, a parameterization [120] is usually applied to take $\frac{\bar{\Sigma}^-}{\bar{p}} = 0.33$ with an assumed uncertainty of 25%. Both branching factors in (5.4.4) can be found in [145] to get

$$\Delta_\Lambda = (0.81 \pm 0.04)\left(\bar{\Lambda}/\bar{p}\right) . \tag{5.4.5}$$

Datasets available for the ratio $\bar{\Lambda}/\bar{p}$ are scarce and inconsistent in terms of measurement parameters (see Reference [130] for a list of these datasets). However, they have been treated to determine $\bar{\Lambda}/\bar{p}$ as a function of energy [130]. The resulting fit is shown in Figure 5.12. It shows that for $\sqrt{s} \lesssim 50$ GeV, the ratio is almost constant at ~ 0.3, while it significantly increases above that energy until it plateaus again at $\sqrt{s} \gtrsim 1$ TeV.

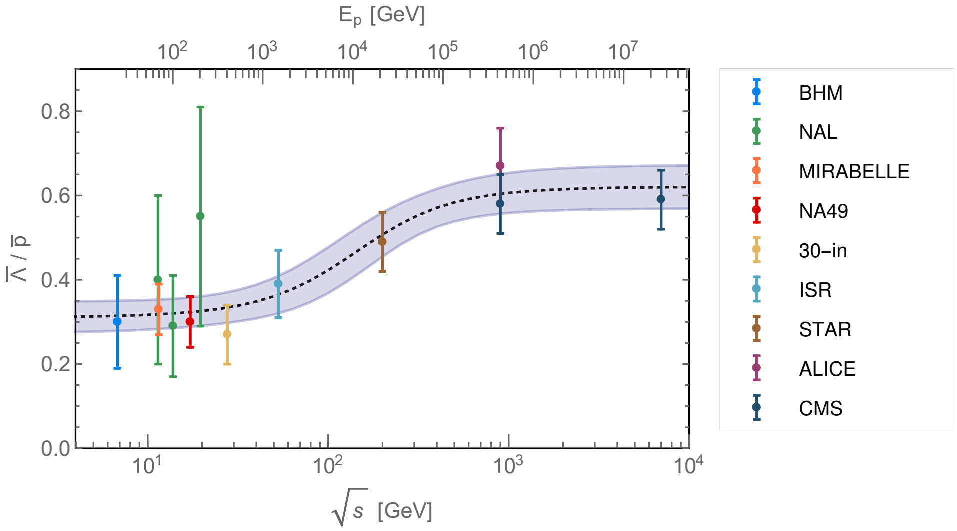

Figure 5.12: The ratio $\bar{\Lambda}/\bar{p}$ in pp collisions, extracted from several experiments. The uncertainty band of the parameterization used for the fit is also shown [130].

Due to the scarcity of datasets on antiproton-production cross sections, other tools had to be applied to bridge the gap when it came to astrophysical modeling of secondary CRs. Among these tools are theoretical parameterizations and Monte Carlo (MC) predictions (cf. [146]). Figure 5.13 shows a comparison of the results from several parameterizations for the differential cross sections of direct $\bar{p}$ production in pp collisions at several representative energies. While the results seem almost congruent at higher energies, they seem to relatively diverge at antiprotons energies below 10 GeV [127].

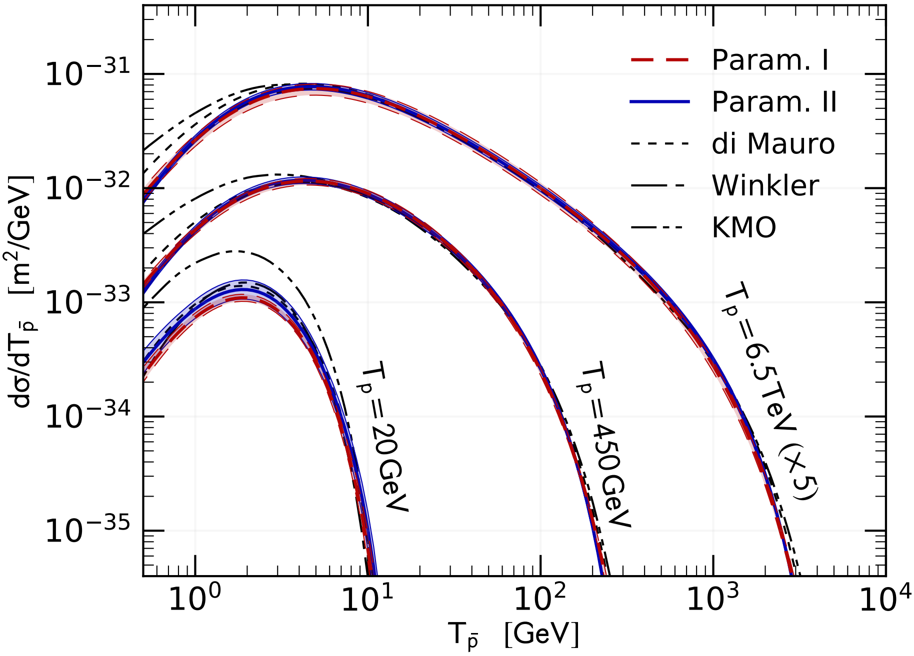

Figure 5.13: A comparison of different parameterizations for the differential cross section $d\sigma/dT_{\bar{p}}$ for the prompt production of antiprotons in pp collisions, at several representative energies [127].

Moreover, since the first measurements (the pHe dataset by LHCb [147]) of any production channel other than pp have only been released in 2018, scaling the cross sections to these other channels has mostly been performed through parameterization of the pp channel. This has often been done with a straightforward assumption of nucleon-nucleon interaction, thus leading to a scaling factor of A^D, where A is the mass number and D is a parameter whose value range between 2/3 and 1. This is based on the approximation of the target area from a classical sphere or the assumption that all nucleon-interactions are completely independent. Because the cross sections for channels other than pp are scaled up from it, the uncertainty that affects that channel propagates to all others, consequently amplified. In addition, production induced by antineutrons and antihyperons increases this uncertainty even further (cf.[127]).

The total secondary-antiproton yield will thus depend on the species of the colliding nuclei and the abundances of these species in both CRs and ISM. Table 5.1 shows previous estimations [148–150] of the abundances of protons, deuteron, helium-3, and helium-4, in both CRs and ISM [151]. Using these abundances, a simple geometric parameterization can be used to estimate the interaction cross sections of each production channel based on the mass numbers of the interacting nuclei. Here, a specific form of the technique referred to above was used. The cross sections, σ_{ij}, normalized to the cross section of the proton-proton collisions, σ_{pp}, were calculated by

$$\frac{\sigma_{ij}}{\sigma_{pp}} = \left(\frac{A_i^{\frac{1}{3}} + A_j^{\frac{1}{3}}}{2A_p^{\frac{1}{3}}} \right)^2 . \tag{5.4.6}$$

Consequently, the collision rate of the i-component of CRs with the j-component of ISM will be directly proportional to $n_i n_j \sigma_{ij}$, where n represents the abundance. The relative contributions to the inclusive antiproton production from the interactions of CRs and ISM components, calculated using (5.4.6) along with the abundances given in Table 5.1, are shown in Table 5.2 normalized to that of pp collisions. It can clearly be seen that pp collisions are the dominant production channel of secondary antiprotons, followed distantly by $p\,^4$He. One might safely then assume that the uncertainty in the antiproton-production cross sections in pp collisions are also the most problematic. Hence, tackling this challenge will be a large step toward matching the precision of the AMS-02 measurements.

Table 5.1: Abundances, n_i, of the light isotopes in CRs[148, 149] and in the ISM[150].

Nuclei	Cosmic Rays	Interstellar Medium
p	0.844	0.911
D	0.029	1.6×10^{-5}
^{3}He	0.027	2×10^{-5}
^{4}He	0.10	0.089

Table 5.2: Relative contributions from interactions of the components of CRs and the ISM into the inclusive antiproton production[124].

Collision	$\bar{p}$ yield normalized to the $\bar{p}$ yield in pp collisions
pp	1
$p\,^4$He	0.4
$p\,^3$He	0.08
pD	0.06
^{4}He^{4}He	0.014

In order to reach the accuracy required to keep up with the recent AMS-02 measurements, researchers have estimated the relative uncertainty, with respect to the AMS-02 measurements, that can be allowed over the invariant cross section of $\bar{p}$-production as follows [146]

$$\sigma^{\text{rel}}_{\sigma_{\text{inv}}}(x, T_{\bar{p}}) = \begin{cases} 3\% & x < x_t(T_{\bar{p}})\,, \\ 30\% & \text{elsewhere}, \end{cases} \tag{5.4.7}$$

where $x_t(T_{\bar{p}})$ is a threshold for the *containment function*, for containing 90% of the source term for a given $\bar{p}$-energy (see Reference [146] for more details on how these limits are chosen). These results are outlined for pp interactions in Figure 5.14 in both laboratory and center-of-mass (CM) frames. The pseudorapidity of the produced antiproton is given by [146]

$$\eta = -\ln\left(\tan\left(\frac{\theta}{2}\right)\right), \tag{5.4.8}$$

where θ is the scattering angle. Moreover, the radial and Feynman scaling variables are defined as [130]

$$x_{\text{R}} = \frac{E^*}{E^*_{\text{max}}}\,, \qquad x_f = \frac{p^*_{\text{L}}}{\sqrt{s}/2}\,, \tag{5.4.9}$$

where * represents the quantities in the CM frame. The maximal energy, E^*_{max}, is entirely determined by the CM energy, $\sqrt{s}$, and is given by

$$E^*_{\text{max}} = \frac{(s - 8m_p^2)}{(2\sqrt{s})}\,, \tag{5.4.10}$$

where m_p is the proton mass. These ranges can be summarized in ranges in terms of LAB frame variables of proton-beam energies from 10 GeV to 6 TeV and pseudorapidity from 2 to almost 8; or in terms of CM frame variables—more suitable for collider experiments—of the radial scaling, given in (5.4.9), ranging from 0.02 to 0.7 and transverse momenta from 0.04 to 2 GeV [146].

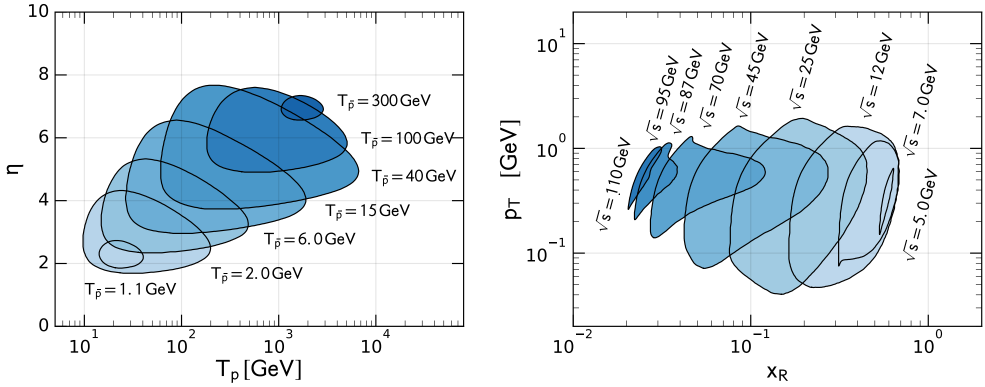

(a) LAB frame (b) CM frame

Figure 5.14: The parameter space for $\bar{p}$-production in pp collisions required to match the recent AMS-02 measurements [129], in both (a) LAB frame variables and (b) CM frame variables. Here, it is necessary to measure the cross section with a 3% accuracy within the shaded regions, and with a 30% accuracy outside the contours [146].

Recent years have offered us several glimpses, of what could be interpreted as DM evidence, from different observation channels including positrons, γ-rays, and antiprotons (see Reference [152] and references within). To come to any conclusions regarding these observations, it is first crucial to test both their consistency with each other and with all previous data, and their statistical significance after accounting for all sources of uncertainties. Upcoming data from AMS-02 is expected to enhance the situation, and help form more firm conclusions (cf.[133]).

In principle, experimental sensitivity is now at a level where a DM contribution that is as low as 10% can be detected. However, for that to be achieved, theoretical and systematic experimental uncertainties have to be first constrained and minimized [137]. Nevertheless, more attention has recently been employed to enhance the situation of these uncertainties, in particular the production cross sections. Some experiments have already started releasing relevant data. The NA61/SHINE at CERN

[153], which is a fixed-target experiment, has collected data for pp interactions with beam momenta ranging from 13 to 400 GeV/c. The LHCb collaboration has also released the first pHe dataset in 2018 at $\sqrt{s} = 110$ GeV [147]. All upcoming LHCb data can be expected to be at higher CM energies. The COMPASS++/AMBER collaboration is also planning to perform measurements with proton beam momenta of 50-280 GeV/c on fixed hydrogen and helium targets [154].

5.5 Discussion

In this Chapter, we discussed the properties of CRs and their components, along with the recent results of space experiments like the AMS-02. In particular, we considered the potential antiproton signal found, and the uncertainties surrounding that signal. Finally, we discussed the outlook for the efforts required for reducing these uncertainties. Some points worth highlighting are:

- CR antiprotons are mainly produced via secondary collisions between primary CRs and ISM nuclei. Primarily produced antiprotons are thought to be produced by exotic sources, such as the decay and annihilation of DM particles. However, in order to be able to detect any exotic contributions, we first need to quantify the secondary production of antiprotons with outstanding precision.

- Proton-proton and proton-helium interactions are the dominant contributors to the secondary antiproton yield in CRs. It naturally follows that any uncertainty regarding the antiproton-production cross sections from these interaction channels will have the largest effect on the total estimation of the secondary antiproton flux.

- Recent measurements by the AMS-02 spectrometer include a potential antiproton signal that could have originated from DM. The signal is consistent with a DM particle of mass around 80 GeV/c^2. However, the signal is surrounded by several sources of uncertainty that prevent researchers from making any firm conclusions about its viability.

- While the uncertainty sources around the signal include propagation parameters—regarding both the galactic environment and the solar modulation—and primary fluxes of protons and helium nuclei, the dominant source of uncertainty is that of production cross sections.

- Antiprotons can be produced via several mechanisms, either promptly or through the decay of short-lived hyperons and antineutrons. The scarcity of data for antiproton production, along with the recent controversy about the effect of isospin on the symmetry of antiproton-antineutron production complicates the estimation of production cross sections.

- New measurements of antiproton-production cross section in all dominant channels are necessary at this point; in addition to tracking each production mechanism individually. Researchers have outlined the parameter space that needs coverage to catch up with the AMS-02 precision. In light of these findings, several experiments are planning to perform measurements of antiproton production in pp and pHe interactions, including LHCb and COMPASS++/AMBER. Nevertheless, the gap is still wide, and more efforts are required to close it.

In the next Chapter, we will introduce the upcoming Spin Physics Detector (SPD) experiment at the NICA collider. We will review its capabilities and limitations in light of the aims and motivation behind the experiment; before we can explore how the SPD can contribute to the search for DM.

Chapter 6

The Spin Physics Detector at NICA

6.1 Motivation & Aims

In spite of the remarkable advances achieved in the realm of high-energy physics, there is still a lot that researchers have not been able to explain or understand yet. This includes, but is not limited to, understanding the different phases of matter at low temperature, the properties of neutron stars, and the stability of the Universe. Since the nucleon spin is evidently related to all of these phenomena, the study of its structure becomes of particular importance. Notwithstanding the success of the quark model, it fails to explain how hadron constituents impact its spin properties. In other words, the question is how the nucleon spin is made up of the spins and orbital momenta of its constituents. While the last few decades have witnessed several experiments (such as CERN, DESY, JLab, SLAC, and RHIC) that increased our information about the functions of the spin-dependent structure of the nucleon, our knowledge is still limited, particularly with regard to the gluon contribution.

The Spin Physics Detector (SPD) has been proposed [155] to be constructed at one of the two interaction points at the Nuclotron-based Ion Collider fAcility (NICA) that is currently under construction at the Joint Institute for Nuclear Research (JINR) in Dubna, Russia. It is proposed as a universal facility to study the nucleon spin structure and other related phenomena, with the availability of polarized and deuteron beams as a start. While the main objective of the experiment is to study the unpolarized and polarized gluon content of the nucleon, the proposed program goes even beyond. It is believed that this detector will have a sizable contribution to our understanding of both the nucleon spin structure and physics BSM.

The experiment is expected to operate with polarized proton and deuteron beams with a collision energy of up to 27 GeV and a luminosity of up to 10^{32} cm^{-2}s^{-1}. In *pp* collisions, the SPD experiment will be able to cover the kinematic gap between low-energy and high-energy measurements, both previous and planned. The aims of the experiment include providing access to the gluon helicity, gluon Sivers, and Boer-Mulders functions, in addition to the gluon transversity distribution and tensor parton distribution functions (PDFs) in the deuteron. Other polarized and unpolarized physics is also planned. The complete proposed physics program can be found in Reference [155].

The layout of the detector, shown in Figure 6.1, is determined by the physics goals. The setup is planned to be a universal 4π one with advanced tracking and particle identification capabilities. A 100 μm (or less) resolution is proposed for the vertex position reconstruction. This will be provided by a silicon vertex detector (VD). As some of the physics goals require secondary-vertex reconstruction, such resolution is necessary. The transverse momentum resolution is planned to be $\sigma_{p_\mathrm{T}}/p_\mathrm{T} \approx 2\%$, for a particle momentum of 1 GeV$/c$. In combination with a time-of-flight system (PID) with a time resolution of 60 ps, this will provide $3\,\sigma$ resolution for π/K separation up to 1.2 GeV$/c$ and for K/p separation up to 2.2 GeV$/c$. It is also possible to use an aerogel-based Cherenkov detector, which will extend these ranges. Photon detection will be available by the electromagnetic calorimeter (ECal) with energy resolution $\sim 5\%/\sqrt{E}$. The detector material will be optimized for minimization of multiple scattering. A muon (range) system will provide muon identification, as well as rough hadron calorimetry. Local polarimetry and luminosity control will be achieved by BBC (Beam-Beam Counters) and zero-degree calorimeters. It is planned to equip the SPD with a triggerless data acquisition (DAQ) system to minimize potential systematic effects. Given that the collision rate could reach 4 MHz, and the few hundred thousand detector channels, it will be significantly challenging to optimize the DAQ, online monitoring, offline computing system, and data processing software.

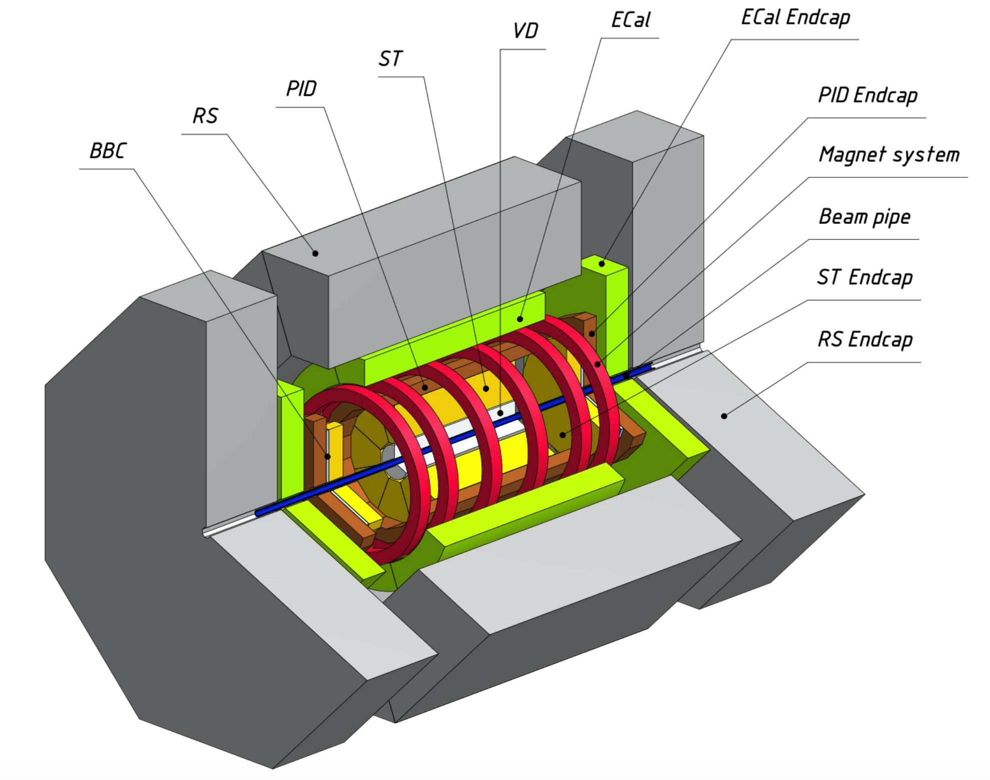

Figure 6.1: General layout of the SPD setup [155].

At this point, the physics program covers at least 5 years of operation with an estimated cost of about 95 M$, not including the research and development (R&D), test-zone construction, or NICA polarized beam infrastructure. In the rest of this Chapter, a brief account of the detector features and capabilities is given, based on the current Conceptual Design Report (CDR) [155] of the experiment.

6.2 Polarized Beams & Detector Setup

At the first stage of the SPD, proton and deuteron beams will be available. At the second stage, there is a possibility to include helium-3 ions as well. It is worth noting that any combination of available colliding beams is possible; that is, pd, $p\,^3\mathrm{He}$, $d\,^3\mathrm{He}$. The dependence of both the luminosity and the number of protons, in the case of pp collisions, on the energy is shown in Figure 6.2. It shows that at a bunch intensity of 10^{11} polarized protons, the luminosity level is at 1×10^{30} cm^{-2}s^{-1}. However, a luminosity level of up to 1×10^{32} cm^{-2}s^{-1} could be obtained, depending on whether a multi-bunch storage mode is used [156].

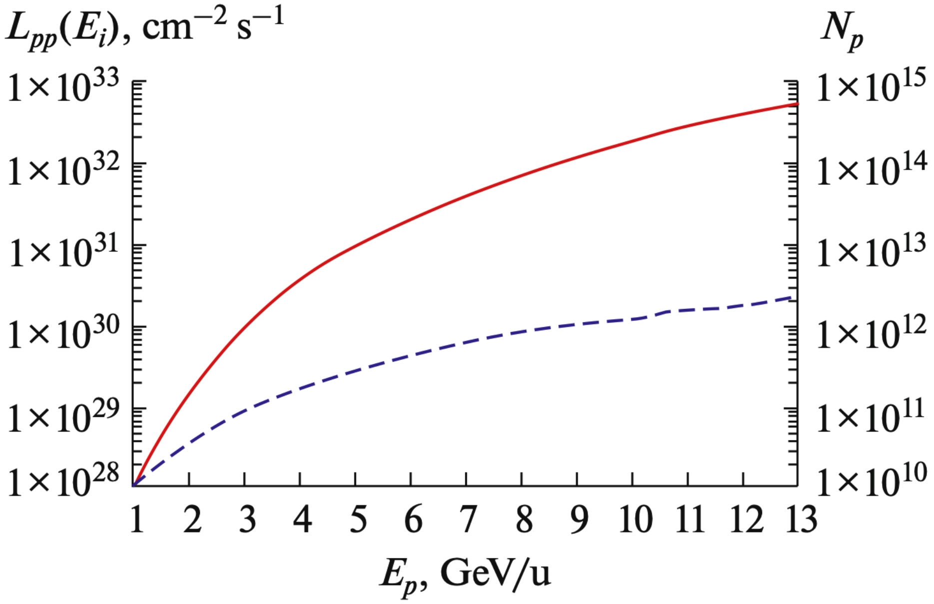

Figure 6.2: Normalized dependence of luminosity (red curve and left scale) and beam intensity (blue curve and right scale) on the proton kinetic energy for pp collisions [157].

The requirements on the design of the SPD layout are imposed by the proposed physics program. Because the interaction energies can be considered relatively low in terms of order of magnitude, the resulting particles are expected to have a uniform distribution over the kinematic range. In combination with small production cross sections, this imposes a $\sim 4\pi$ coverage requirement on the SPD setup. Proposed muon physics probes also impose a requirement of a range system with a high separation power of muons and hadrons. A precision vertex detector will also be necessary for reconstruction of secondary vertices from the decays of short-lived particles. For photon physics, an electromagnetic calorimeter would be required for signal/background separation. A low material budget throughout the setup will also enhance the conditions for photon physics. Of course, for any proposed probes that include protons and/or kaons as final products, hadron identification will be required. As investigation of tiny effects is included in the program, a triggerless DAQ system is also required to minimize potential systematic uncertainties. Some limitations are also imposed on the SPD setup due to external factors. Some of these are the maximum weight the experimental hall floor could withstand, the minimum nuclear interaction lengths required for the overall thickness of the muon system limiting both the outer and inner sizes of the detector, and the limit on the size of the SPD setup along the beam axis that is defined by the location of the collider infrastructure.

A schematic representation of the general layout of the SPD is shown in Figure 6.3. The SPD magnetic system, like other setup components, has to satisfy the criteria of minimal material, and weight. Many options, including solenoidal, toroidal, and hybrid configurations, were considered and analyzed. The result was in favor of a separate 6-coil design. A beam pipe will separate the detector and high vacuum of the accelerator. While being mechanically sturdy, it will also be as thin as possible to minimize the number of radiation lengths, thus optimally preventing multiple scattering and radiation effects. A diameter, of about 6 cm with 0.5-mm wall thickness, has been chosen to allow coordinate detectors to be positioned as close to the interaction point as possible. This in turn will enhance the reconstruction of primary and secondary vertices. While a beryllium beam pipe has been proposed, a cheap stainless steel one will likely be used at the first stage of the SPD running. A schematic view of the pipe inside the setup is shown in Figure 6.4.

The vertex detector will be responsible for coordinate determination of the primary interaction point as well as secondary vertices from decays of short-lived particles. It consists of a barrel and two end caps. The barrel part covers a radius from 96 to 500 mm. All five layers are equipped with silicon strip detectors that determine the (r, ϕ, z) coordinates of the tracks, where a point is measured in each layer. The end-cap regions detect particle tracks radially between 96 mm and 500 mm. The vertex detector will have a length of 1.1 m. The general layout of the vertex detector is shown in Figure 6.5. The requirements imposed on the vertex detector are: a geometric acceptance close to 4π;, a muon-track reconstruction efficiency greater than 99% at $p \leq 13$ GeV/c, a low material budget, and coordinate resolutions of $\sigma_{r,\phi} < 50$ μm and $\sigma_z < 100$ μm. Finally, the lifetime of the vertex detector has to be at least 10 years of the NICA running.

The straw tracker will be responsible for reconstruction of primary and secondary particle tracks with high efficiency, as well as precisely measuring their momenta based on the track curvature in the magnetic field, and contributing to particle identification by use of the energy deposition (dE/dx) measurement. Its spacial resolution is expected to be about 150

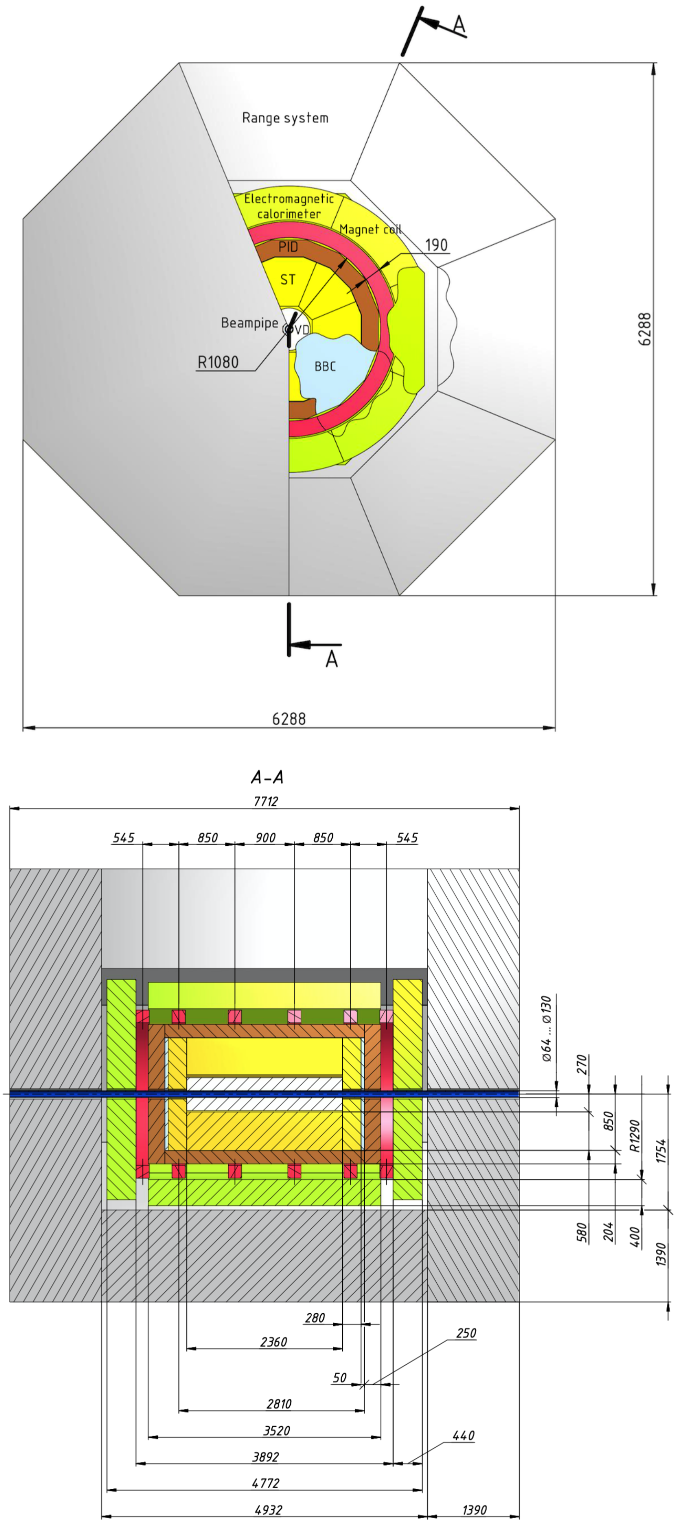

Figure 6.3: The general layout of the Spin Physics Detector [155].

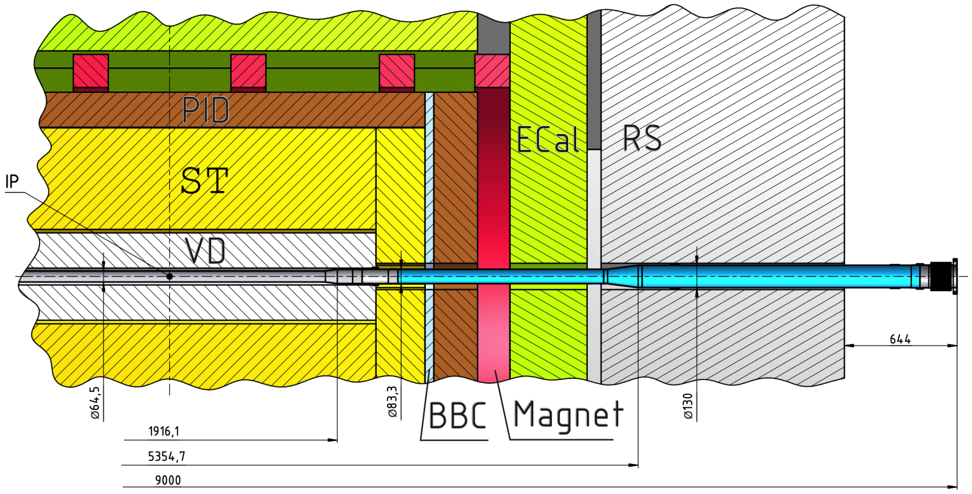

Figure 6.4: The SPD beam pipe inside the setup [155].

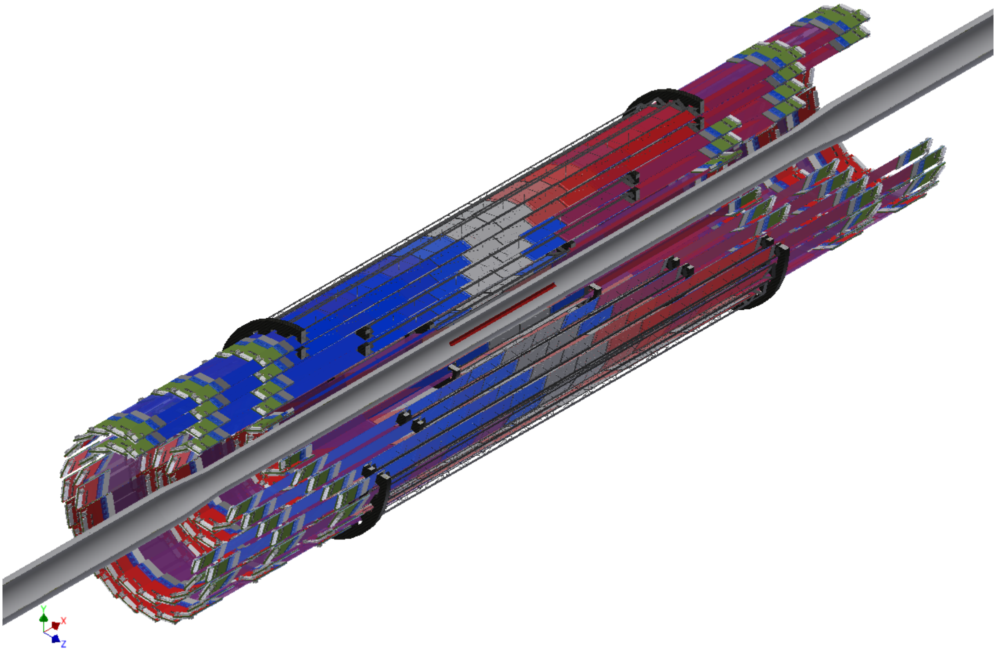

Figure 6.5: The general layout of the SPD vertex detector [155].

μm. It is planned to be built of low-mass straw tubes with a concept similar to the ATLAS TRT [158] and PANDA [159] straw trackers. The criteria imposed on the ECal by the physical goals of the experiment are: photon and electron reconstruction within the energy range from 50 MeV to 10 GeV, energy resolution $\sim 5\%/\sqrt{E}$ [GeV], high separation of two-particle showers, operation in the magnetic field, and long-term stability ($2-3\%$ in a 6-month period of data taking). The ECal will consist of a barrel and two end-caps. It will cover a 4π solid angle, and will be placed between the range system and magnet coils. A schematic view of the calorimeter is shown in Figure 6.6(a).

The range system will be responsible for identifying muons in the presence of high hadronic background, and for coarse hadron calorimetry; that is, rough determination of hadronic energy. Neutron identification is entirely dependent on this device, where its signal can be combined with the ECal and inner trackers for that purpose. It also consists of a barrel and two end-caps. Their absorption thickness is planned to be 4 nuclear interaction lengths (λ_I) such that when combined with the ECal thickness of $0.5\lambda_I$, the total thickness of the SPD setup becomes about $4.5\lambda_I$.

The particle identification (PID) system of the SPD will include a time-of-flight (TOF) detector and a Cherenkov threshold detector with an aerogel radiator. Particles with longer trajectories can be identified by the TOF and aerogel counters. However, in the case of soft particles with shorter trajectories, the PID system data will have to be combined with energy-loss data from the straw tracker. Two TOF technologies are being considered, which are indicated in Figure 6.7. The final choice is bending more detailed studies of performance and costs. The TOF sys-

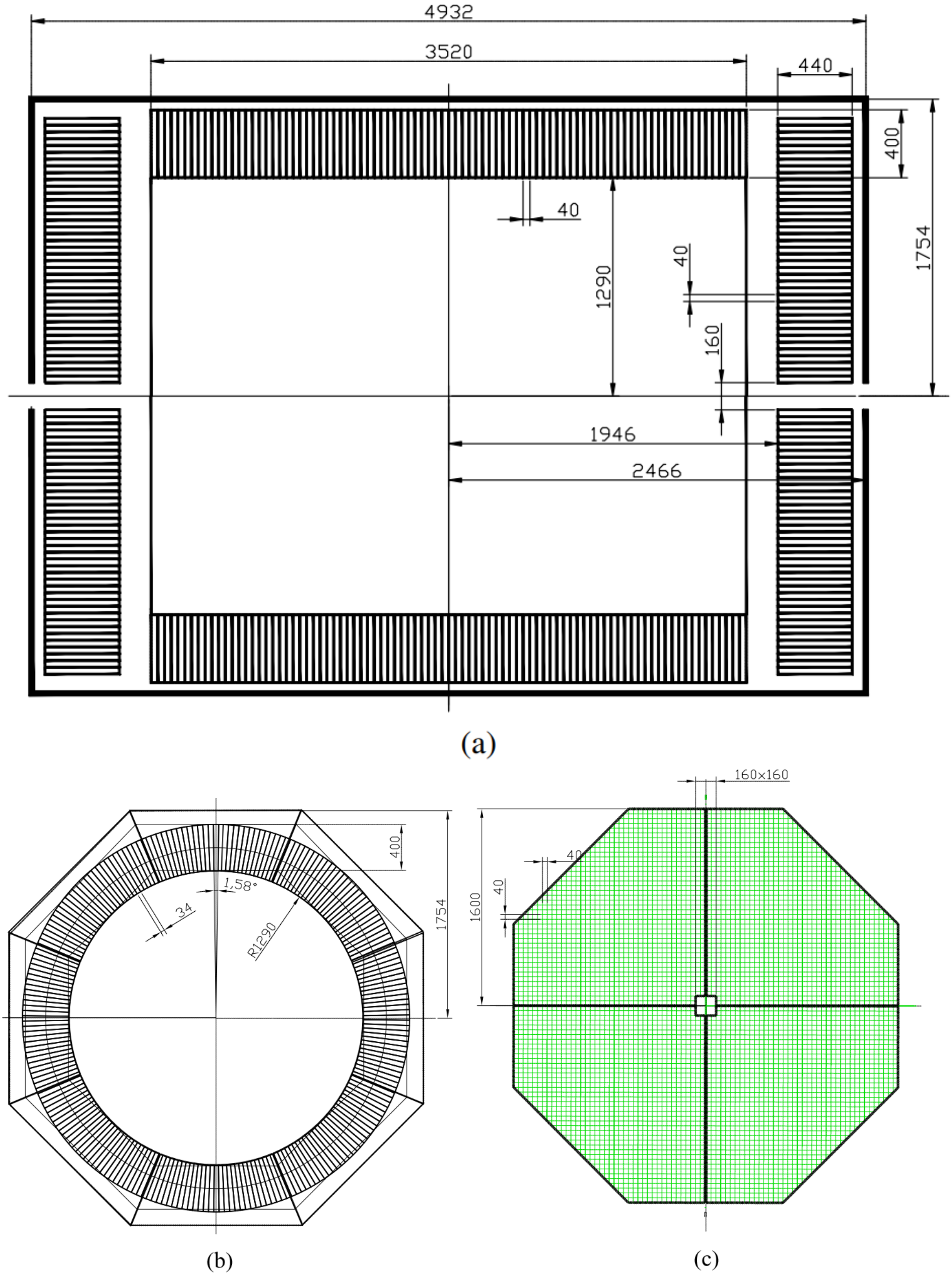

Figure 6.6: A schematic view of (a) barrel and end-cap parts of the ECal, (b) a cross section of the barrel part of the calorimeter, and (c) the end-cap part of the calorimeter [155].

tem will separate charged particles of different masses with momenta up to a few GeV/c. Due to the short distance of 108 cm from the interaction point, it is necessary for the TOF system to have a time resolution better than 70 ps. Both particle identification and event-time (t_0) reconstruction can only be performed for multi-track events. The procedure for t_0-reconstruction will be outlined in Chapter 7. The TOF system will have a barrel and two end-caps. Its overall area will be of 27.1 m^2.

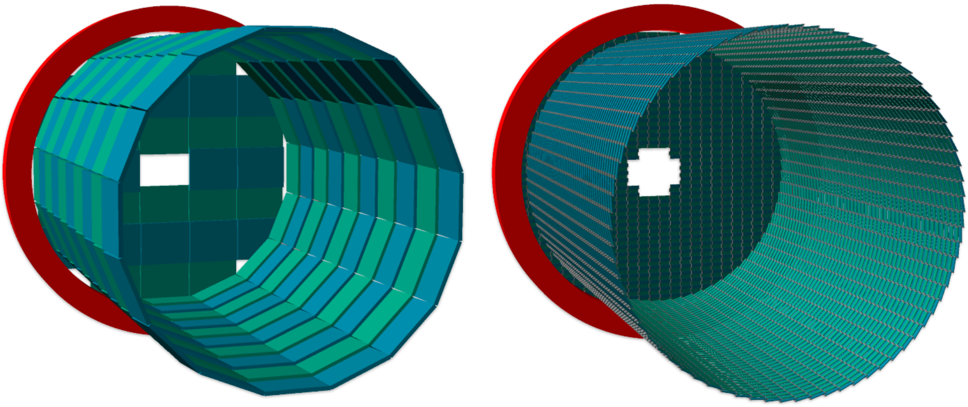

Figure 6.7: The two technologies being considered for the TOF system of the SPD: a multigap Timing Resistive Plate Chamber, mRPC (*left*), and a plastic scintillator option (*right*). Shown in red is one of the six magnet coils restricting the volume of the TOF system [155].

6.3 Computing System

For pp collisions at $\sqrt{s} = 27$ GeV and a luminosity of 10^{32} cm^{-2}s^{-1}, the event rate of the SPD is expected to be around 3 MHz, which in terms of raw data is about 20 GB/s or 200 PB/year, with a detector duty cycle of 0.3 and a signal-to-background ratio of the order 10^{-5}. Since a trigger decision would have to depend on momentum measurement and vertex determination, which makes tracking necessary, there is no simple selection of physics events at the hardware level. In addition, the continuous data stream from the free-running DAQ would require sophisticated unscrambling before building events individually. Thus, a trigger system at the hardware level would be over-complicated and unattainable in terms of computing capabilities. While noise filtering can be performed by DAQ, a software trigger system will have to be applied by an online filter that performs fast partial event reconstruction and data selection. Its aim will be decreasing the data rate by a factor of at least 50. After that, the data will be transferred to the Tier-1 facility where the data will be fully reconstructed and permanently stored.

As for data analysis and Monte-Carlo simulation, they will be performed at remote computing centers (Tier-2). To deal with such large data volumes, the event model and reconstruction performance and simulation algorithms will have to be thoroughly optimized. To take advantage of recent advances in computing hardware and software, an R&D program will be in place to deploy software for DAQ, management, processing, and analysis. This will be parallel to the physics program elaboration and the detector design. Machine learning (ML) algorithms will also be employed for multi-track recognition problems. However, validation data will be regularly utilized to monitor the performance of these algorithms, in order to avoid any bias that might arise due to insufficient training data. The overall scheme of the SPD computing as currently planned is shown in Figure 6.8. It is planned to utilize distributed computing tools for the URMS (Unified Resource Management System). These tools have already been developed for LHC experiments such as PANDA and DIRAC. Such tools will be evaluated and implemented in the phase of Technical Design Report (TDR) preparation.

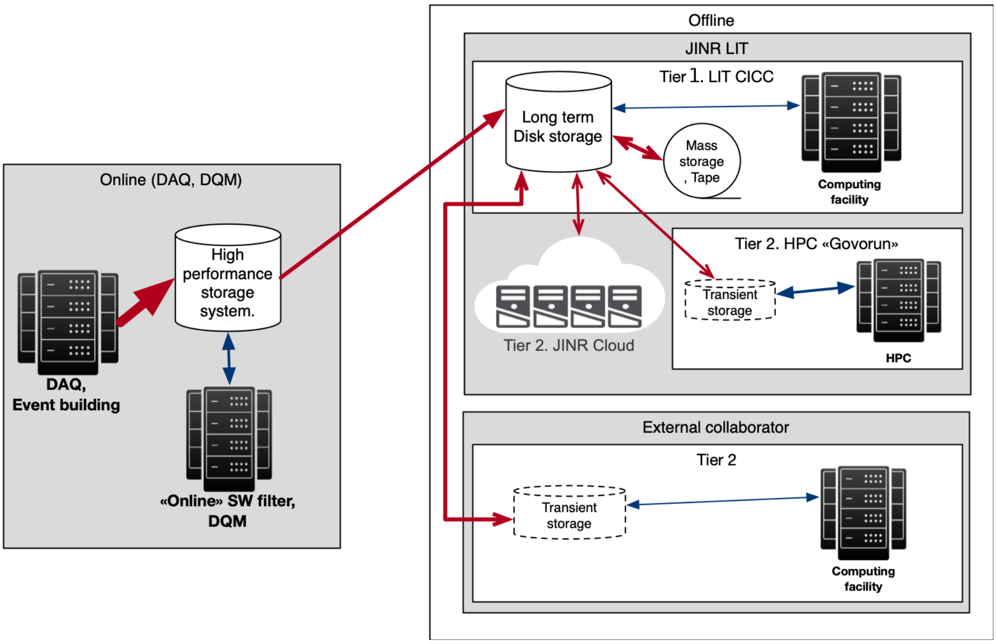

Figure 6.8: Scheme of the SPD computing system [155].

6.3.1 SpdRoot

The offline software package is SpdRoot. It is currently being developed for the future SPD detector for event reconstruction, MC simulation, data analysis, and visualization, with Linux as the base OS. The current version of the SpdRoot package can be found at [160]. Until now, SpdRoot utilizes a lot of the code and structure of FairRoot [161]. The FairRoot is a framework for data simulation, reconstruction, and analysis. It employs object-oriented-programming concepts to provide physicists with a unified package to handle high-energy-physics tasks without encountering purely software-engineering issues. HTML documentation can be created for the list of SpdRoot classes using the Doxygen package. There are three geometries available in SpdRoot, corresponding to different magnetic field configurations. They are namely: solenoidal, toroidal, and hybrid. The package also includes previously-written scripts for simulating a series of events with different geometries. The user can also customize the geometry and specify the number of events to be simulated. Output files include data and simulation parameters, independently. The main primary vertex generator for *pp* collisions in SpdRoot is Pythia8 [162]. Secondary particle transportation and detector response simulation are performed by the Geant4 toolkit [163]. The package also offers output data visualization in terms of the setup geometry and particle tracks. It also includes magnetic field tutorial scripts. Naturally, the package accommodates direct data access for analysis.

6.4 Project Timeline & Discussion

The CDR [155] for the SPD has been presented at the 54th meeting of the JINR Programme Advisory Committee (PAC) for particle physics in January 2021 [164]. The Committee has consequently recommended the NICA management to appoint a detector advisory committee for a thorough review of the CDR and its subsequent evolution into an SPD TDR. The proposed physics program covers at least 5 years of the SPD running, while the timeline of the project is planned to be as follows:

- **2022, Jan.:** Presentation of the TDR at the JINR PAC;
- **2022:** Start of the NICA collider operation;
- **2023–2025:** Assembling the SPD detector;
- **2023+:** Detector and physics tests at the SPD interaction point;
- **2025+:** SPD physics run.

In this Chapter, we have taken a look at the upcoming SPD experiment at the NICA collider. We have reviewed its capabilities and limitations; and we have seen the different systems planned as parts of the general layout of the experiment, in light of its physics program. A few points to recall are:

- The main aim of the SPD is to study the nucleon gluon content. However, the physics program includes the gluon helicity, tensor PDFs in the deuteron, and other polarized and unpolarized physics.
- The SPD will operate with polarized proton and deuteron beams with a collision energy up to 27 GeV and a luminosity up to 10^{32} $\text{cm}^{-2}\text{s}^{-1}$. The SPD will thus cover the kinematic gap between low-energy and high-energy measurements. The layout will include a vertex detector, a magnetic system, a PID system, an ECal, a range system, and local polarimetry and luminosity control.
- In addition to proton and deuteron beams, there is the possibility of including helium-3 and helium-4 in the subsequent stages of the experiment. This will enable further measurements fro interactions involving these nuclei; especially with the possibility to use any combination of the available beams.
- The high luminosity of the SPD would be equivalent to about 20 GB/s of raw data. This requires a triggerless DAQ system along with an online filter for partial reconstruction and data selection. Nevertheless, such a large data system will call for the implementation of ML algorithms that would need to be developed, deployed,

monitored, and optimized. An R&D program is planned for the software deployment for data acquisition, management, processing, and analysis.

In the next Chapter, we will first discuss the motivation behind this work. We will then explore the possibility of performing measurements at the SPD to contribute to the ID search for DM. We will finally review our results and discuss the feasibility of the proposed measurements.

Chapter 7

Measuring Antiproton Production at NICA

7.1 Introduction & Motivation

We have seen how DM has been a long-standing problem in our understanding of the Universe. Until now, all our knowledge of the physical content of the Universe only covers less than 5% of the energy budget; the rest remains a mystery to us. It can easily be argued that deciphering the identity of DM will provide us with many more pieces to complete the puzzle that is Our Universe. Unlike dark energy, which has mostly been associated with gravity in terms of both the problem and its solutions, DM lies at the overlap between the gravitational force and the rest of the forces identified by the SM. While the evidence of DM existence is almost all gravitational, the road to its identity calls for integration of the rest of the forces as well. This can be seen in the theories of DM candidates, which range from SM particles, exotic particles, and theories of modified gravity that accommodates the phenomena associated with DM. We can thus see how all efforts can complement each other by pursuing several lines of theoretical investigation. We have also seen how the experimental search approaches employed for hunting DM are complementary to each other. Each of them is based on a certain hypothesis about DM, but also each of them helps constrain the properties of any potential DM candidate to narrow the search.

The AMS-02 is one experiment trying to indirectly detect DM by tracking any anomalous traces in CRs. We have seen in Chapter 5 how the antiproton signal found recently by the AMS-02, and suggesting a DM particle of mass around 80 GeV/c^2, still cannot be confirmed due to several sources of uncertainty. The most significant uncertainty that hinders any conclusions is that associated with antiproton-production cross sections. There is no use increasing the precision of astrophysical measurements if our understanding of the background for potential signals remains limited. Naturally, this drew the attention of many researchers who started working on accurately outlining the measurements required for matching the AMS-02 precision levels. Consequently, several collider experiments have included the required measurements in their physics program. Of course, the kinematic range covered by each experiment will depend on the energy scales and detection coverage available for it.

The upcoming SPD experiment planned at the NICA collider is one experiment that can contribute to these measurements, and consequently to the ID search for DM that could lead to the discovery of new physics. Not only will it be possible to perform measurements of antiproton yield in proton-proton collisions, but measurements can also include deuteron collisions, and maybe helium in the future; in addition to any available combination thereof. Nevertheless, in order to assess the possibility of performing such measurements with rewarding outcomes, and to outline the contribution the SPD can make to the parameter space requiring coverage, theoretical estimations based on Monte Carlo simulations have to first be performed. This work aims at supplying these requirements.

This MC study has been carried out in two stages: In the first stage[151], the kinematic features of antiproton production in *pp* collisions were explored based only on simulations using Pythia8 [162], with the addition of some cuts applied according to what the expected limitations of the SPD would be at the time[151]; in the second stage[165], the SpdRoot toolkit [160] was used to simulate *pp* collisions at $\sqrt{s} = 26$ GeV, and investigate previous findings further; in addition to implementing some specific techniques to predict the feasibility of the proposed measurements.

7.2 Antiproton Production Simulation Using Pythia8

Since the energy of a produced antiproton must be at least equal to the proton mass, we get from (5.4.10) that

$$\frac{s-8m_p^2}{2\sqrt{s}} \geq m_p\,, \tag{7.2.1}$$

where the the CM energy is given by

$$\sqrt{s}=\sqrt{2m_p\,(E_p+m_p)}, \tag{7.2.2}$$

while E_p is the total energy of the incident proton in the LAB frame. Substituting with (7.2.2) into (7.2.1) gives us the inequality

$$E_p^2-8m_pE_p+7m_p^2\geq 0. \tag{7.2.3}$$

Solving this gives us two possibilities: either $E_p \leq m_p$ or $E_p \geq 7m_p$. Since also the energy of the incident proton cannot be less than the proton mass, this tells us that the threshold energy for the incident proton is $E_{p\,,\mathrm{th}} \geq 7m_p$.

To gauge the possibility of measuring antiproton yield at NICA SPD in light of the expected luminosity, Pythia8 [162] was used to generate MC simulations to estimate the yield of antiprotons in pp collisions in a wide-energy range, starting from the minimum energy available ($\sqrt{s} =$ 10 GeV) and up to 2 TeV. Figure 7.1 shows the results for the antiproton-production cross section in pp collisions multiplied by the average antiproton multiplicity as a function of the CM energy. It can be seen that the inclusive cross section in the NICA SPD kinematic range (< 27 GeV) is on the level of a few millibarns. The antiproton-production rate is obtained by

$$\frac{dN_{\bar{p}}}{dt} = L\,.\,\sigma_{\bar{p}}. \tag{7.2.4}$$

Given that the NICA SPD luminosity (L) is expected to reach 10^{32} cm^{-2}s^{-1}, this will correspond to an antiproton-production rate on a level $> 10^{5}$ s^{-1}.

The momenta of produced antiprotons were represented along with the polar angle (θ), as shown in Figure 7.2, for the CM energies of 13 GeV and 26 GeV. The results indicate how the 4π coverage, allowed by the collision mode, of the NICA SPD will offer a significant advantage in covering most of the antiproton yield in terms of angular distribution. Such an advantage is rarely achievable in fixed-target experiments.

As mentioned in Chapter 5, antiprotons can be produced either directly or via the decay of short-lived particles; namely, anti-hyperons ($\bar{\Lambda}$ and $\bar{\Sigma}^{-}$) and antineutrons. Figure 7.3 shows the momentum spectra for antiprotons produced from each of these four contributions separately. It can be seen that the bulk of the produced antiprotons have momenta below 5 GeV/c. The momenta are thus low enough to be identified by the TOF system of NICA SPD. It can also be seen that this bulk will include antiprotons produced by all four contributions without introducing any bias to the measurements.

The relative yields of antiprotons in pp collisions from direct production and the decay of anti-lambdas, anti-sigmas, and antineutrons, were estimated using Pythia8 simulations at CM energies of 13 GeV and 26 GeV. The results are presented in Table 7.1. These estimations stress the importance of secondary-vertex reconstruction for investigating the

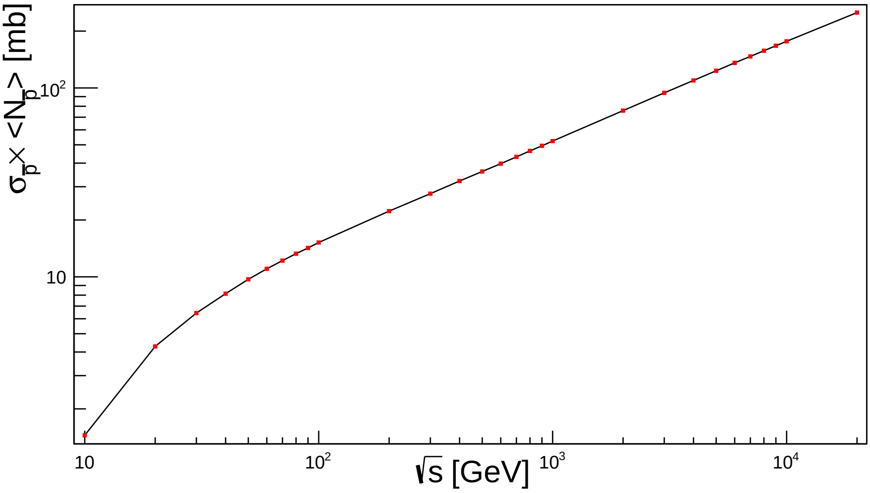

Figure 7.1: The antiproton-production cross section in pp collisions multiplied by the average antiproton multiplicity as a function of the CM energy; covering a range from 10 GeV to 20 TeV[151].

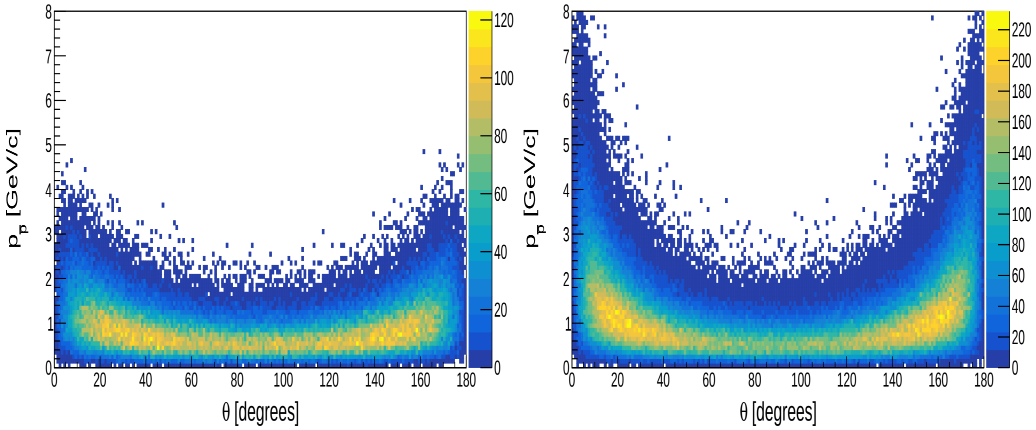

(a) (b)

Figure 7.2: The momentum ($p_{\bar{p}}$) versus the polar angle (θ) of antiprotons produced in pp collisions at (a) $\sqrt{s} = 13$ GeV and (b) $\sqrt{s} = 26$ GeV.

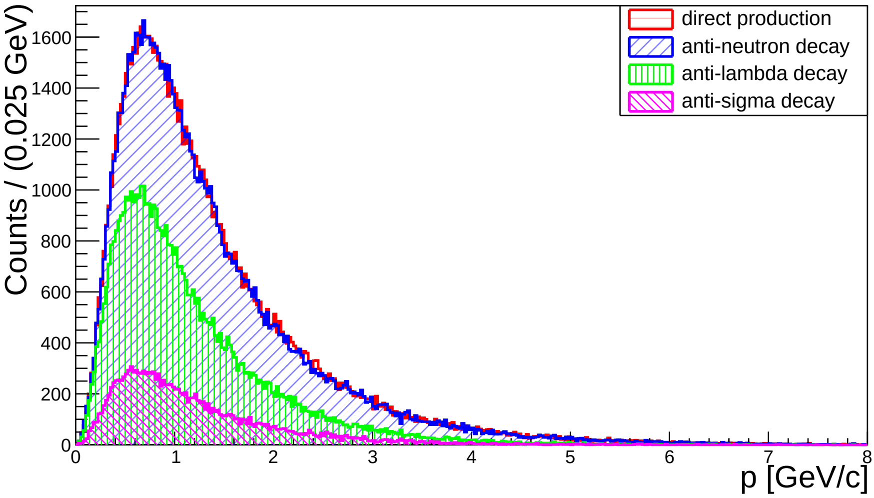

Figure 7.3: The momentum spectra of the different antiproton-contributions produced in pp collisions at CM energy $\sqrt{s} = 26$ GeV[151].

antiproton yield from anti-hyperon decays. In addition, they also show how the significance of this yield increases with energy.

Another matter that needed to be taken into account is the ability of the detector to separate antiprotons from other antiparticles that have the same electric charge; namely, negatively-charged kaons and pions. At this stage of the study, only the yield of each particle species was investigated in terms of momentum. Figure 7.4 shows the momentum spectra of antiprotons, and negatively-charged kaons and pions, in pp

Table 7.1: The relative yields of antiprotons in pp collisions at CM energies $\sqrt{s} = 13$ and 26 GeV[151].

Production	$\sqrt{s} = 13$ GeV	$\sqrt{s} = 26$ GeV
Direct	38.6	37.3
$\bar{n}$ decay	37.9	36.9
$\bar{\Lambda}$ decay	18.1	19.8
$\bar{\Sigma}^-$ decay	5.4	6.0

collisions of CM energy $\sqrt{s} = 26$ GeV. As could be expected, π^-'s are the most abundant while both $\bar{p}$'s and K^-'s have similar profiles. It is worth noting that only final products were counted in this figure. More in depth analysis of this had been performed in the second stage of the study, as will be discussed in §7.3. At this point, it was estimated that $\bar{p}/K^-$ separation will be possible up to a momentum of 4 GeV/c [151].

The last part investigated at this stage of the study was comparing the potential contribution of the suggested measurements to overcoming the challenge of uncertainties of antiproton-production cross sections. To do that, the antiproton yield was assessed through Pythia8 MC simulations. As mentioned in §5.4, the current data available for antiproton production in pp collisions were collected and evaluated in Reference [130]. In addition, the parameter space that needs to be covered in order to match the AMS-02 measurements had also been outlined in the same work. So, the antiprotons produced in the pp collisions simulated by Pythia8 were represented in the CM frame in terms of the radial scaling variable given by (5.4.9) and the transverse momentum, for CM energies of both 13 GeV and 26 GeV. Then, these representations were superimposed on the results given by [130]: the already-existing datasets and the required phase-space coverage. However, some cuts were first applied based on the expected limitations—due to the magnetic field and the material budget of the detector—and the power of separation of the NICA SPD at the time. These cuts included transverse momenta below 200 MeV/c, momenta above 3.5 GeV/c, and polar angles below 0.02 radian or above $(\pi - 0.02)$ radian. The results are shown in Figure 7.5. In particular, it seems that relatively-high transverse momenta are accessible even at a low radial scaling (*i.e.* energy). It can thus be clearly seen that the first indications were promising that NICA SPD could indeed add a valuable contribution to minimizing the uncertainties hindering the indirect search for DM.

7.3 Antiproton Production Simulation Using SpdRoot

The second stage of this MC study [165] was performed using the SpdRoot toolkit [160] of which a brief account has been given in §6.3.1. Although the simulated detector features have changed as the SPD design consolidated, the conclusions drawn from the results outlined below have not changed.

The first result that was revisited using the SpdRoot package was the last result given in the previous section; namely, the kinematic coverage accessible to the NICA SPD; shown previously in Figure 7.5. However, this time, the SpdRoot toolkit allowed the geometrical acceptance of the tracking system, which affects the efficiency of track reconstruction and the energy losses of the produced antiprotons, to be taken into account; in addition to the magnetic field that prevents low-energy particles to reach the TOF system. Thus, only detected antiprotons were included in this representation shown in Figure 7.6. It is also worth noting that antiprotons produced by decays of short-lived particles were not included in this representation.

This brings us to the next result of this stage of the study; that is, assessing the efficiency of antiproton detection by the TOF system. A directly-produced antiproton was considered detected if it reached either the barrel or an end-cap of the TOF system; its track thus being regis-

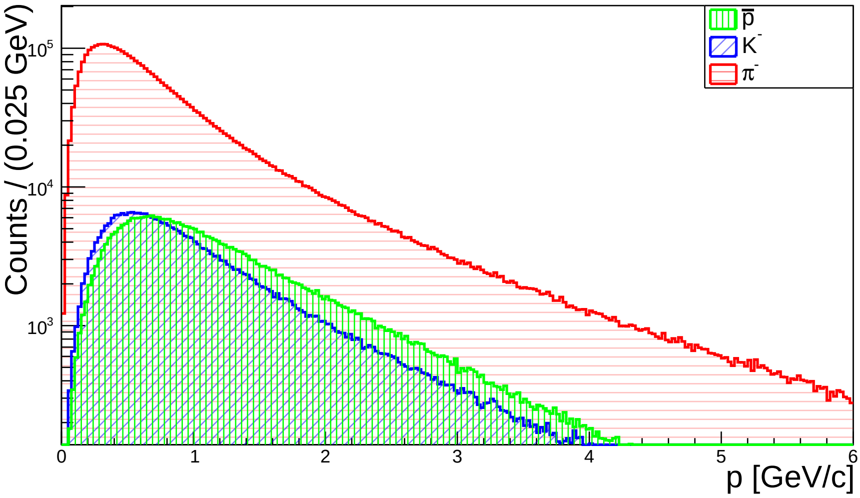

Figure 7.4: The momentum spectrum of antiprotons, and negatively-charged kaons (K^-) and pions (π^-), produced in pp collisions at CM energy $\sqrt{s} = 26$ GeV[151].

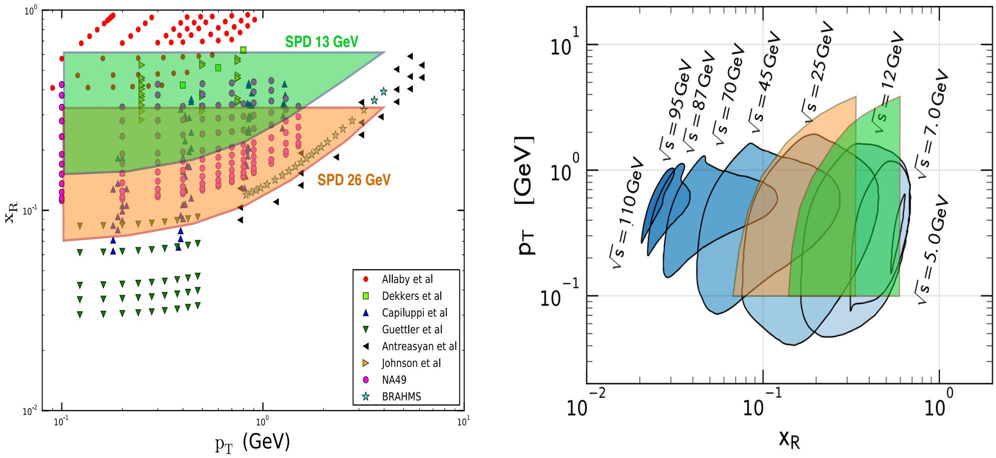

(a) (b)

Figure 7.5: The kinematic range accessible for pp collisions at the SPD detector[151], superimposed on (a) the graphic illustration of currently existing data[121], and (b) the required measurement range to match the uncertainty level of the AMS-02 measurements[146]. Some cuts were applied to the momenta (p), the transverse momenta (p_T), and the polar angle of the produced antiprotons, based on the conceptual design of the SPD at the time.

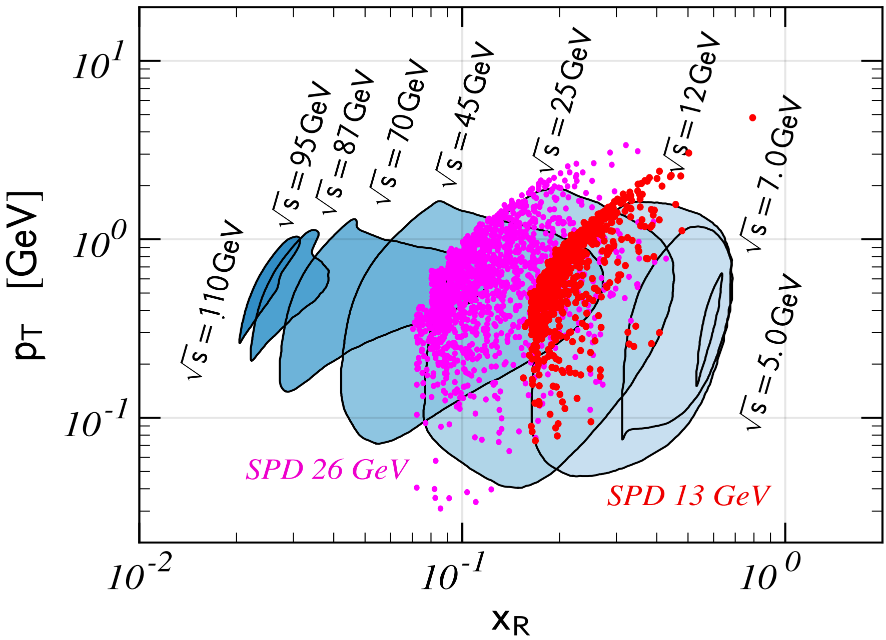

Figure 7.6: The kinematic range accessible for *pp* collisions at the SPD detector[165], where the *red* points represent a CM energy of 13 GeV and the *magenta* points represent a CM energy of 26 GeV, superimposed on the required measurement range to match the precision level of the AMS-02 measurements[146].

tered. Each of the radius of the barrel part and the distance from the center of the detector to each of the end-cap parts were assumed to be 2.0 m. The results are shown in Figure 7.7 for *pp* collisions at a CM energy of 26 GeV. It is clear that the efficiency of antiproton detection can be expected to be quite high, at least 83% for antiprotons with momenta higher than 0.5 GeV/c. It can also reach up to 97% for momenta higher than 3 GeV/c.

For the evaluation of the event collision time (t_0) and as a first step to PID, the algorithm described in Reference [166] was applied. The algorithm uses a χ^2-minimization procedure on track-mass combinations to

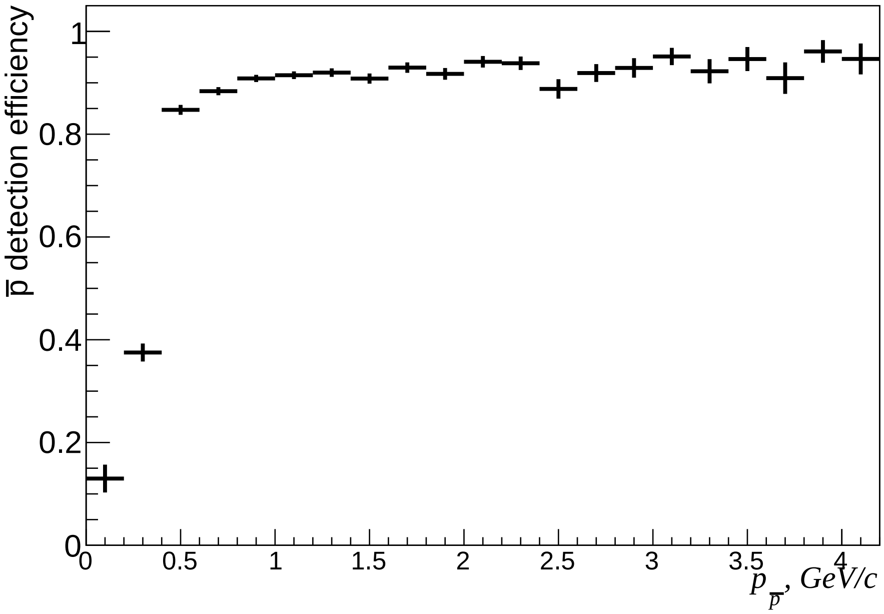

Figure 7.7: Detection efficiency as a function of antiproton momentum for pp collisions at $\sqrt{s} = 26$ GeV.

determine the most accurate evaluation of the event collision time. In this work, this procedure was only applied on events with track multiplicities above 3, as a threshold for antiproton production. For each track in the event, a mass hypothesis is independently assigned from three possible masses; namely, the masses of π, K, and p. When this is applied to all tracks, 3^n mass combinations can be identified for the event, where n is the number of tracks. These can be defined by

$$\vec{m}_j = (m_1, m_2, \ldots, m_n) \ , \tag{7.3.1}$$

where m_j is the j^{th} mass combination among the 3^n ones. Then, the expected time-of-flight is calculated for each track, based on its consecutive mass hypotheses, by the formula

$$t_{\mathrm{exp},i} = \frac{\sqrt{p^2 + m_i^2}}{p}\, l\,, \tag{7.3.2}$$

where i denotes the track number, p the momentum, m_i the mass hypothesis of the track, and l the track length. Both p and l are measured by the detector. The weight of each track is then evaluated by

$$W_i = \frac{1}{\sigma_{\mathrm{TOF}}^2 + \sigma_{t_{\mathrm{exp},i}}^2}\,, \tag{7.3.3}$$

where σ_{TOF} is the TOF detector resolution, taken to be 70 ps, and $\sigma_{t_{\mathrm{exp},i}}$ is the uncertainty on the expected time-of-flight of the track as calculated by (7.3.2). The latter, as can be expected from the above equation, depends on momentum and particle species in addition to the tracking and reconstruction precision. Propagating the expected uncertainties through (7.3.2), it was possible to evaluate it by

$$\sigma_{t_{\mathrm{exp},i}} = \frac{t_{\mathrm{TOF}}}{p}\,\frac{m^2}{p^2 + m^2}\,\sigma_p\,, \tag{7.3.4}$$

where σ_p is the measured-momentum resolution, which was taken to be $0.02\,p^2/p_T$. The event time for the particular mass combination can be then evaluated by

$$t_{\mathrm{ev}}^{\mathrm{TOF}}(\vec{m}_j) = \frac{\sum_{i=1}^{n} W_i (t_{\mathrm{TOF}} - t_{\mathrm{exp},i})}{\sum_{i=1}^{n} W_i}\,, \tag{7.3.5}$$

where the resolution can then be evaluated by

$$\sigma_{t_{\mathrm{ev}}^{\mathrm{TOF}}}(\vec{m}_j) = \sqrt{\frac{1}{\sum_{i=1}^{n} W_i}}. \tag{7.3.6}$$

It is then finally possible to calculate χ^2 by

$$\chi^2(\vec{m}_j) = \sum_{i=1}^{n} \frac{\left(\left(t_{\text{TOF}} - t_{\text{ev}}^{\text{TOF}}(\vec{m}_j)\right) - t_{\exp,i}\right)^2}{\sigma_{\text{TOF}}^2 + \sigma_{t_{\exp,i}}^2}. \tag{7.3.7}$$

Whichever mass combination minimizes the χ^2 value is taken to calculate the event collision time (t_0) as given by (7.3.5).

It would be expected from (7.3.6) that the uncertainty on the event collision time evaluated by this procedure depends on the track multiplicity of the event such that $\sigma_{t_0} \propto 1/\sqrt{n}$. By evaluating the collision times evaluated for SpdRoot MC events, and assessing the value of σ_{t_0} as a function of the track multiplicity, this was found to be satisfied. This result is shown in Figure 7.8. The resolution was found to be of 40-50 ps and lower for tracks with multiplicities above 9.

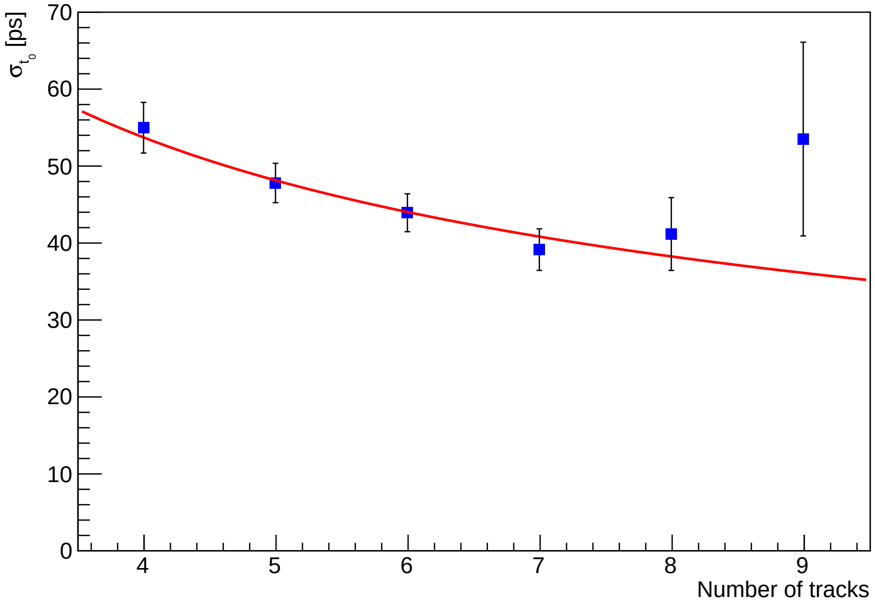

Figure 7.8: Event time (t_0) reconstruction accuracy as a function of the number of charged tracks in the event[165].

The possibility of antiproton identification and separation from other identically-charged particles; that is, π^- and K^-, was explored in two stages. In the first stage, the relative speeds of the detected negative pions and kaons, and antiprotons were plotted as a function of the produced particle momenta. It was done once without applying any uncertainties and another with a TOF resolution of 100 ps and a momentum resolution of 2%. The resulting plots are shown in Figure 7.9. These were then used to determine a cutoff speed to include 90% of the detected antiprotons. Accordingly, the maximum separation momentum possible was determined such that the contamination ratio from π^-'s and K^-'s into the $\bar{p}$-yield does not exceed 10%. It was found that this separation momentum was around 3.5 GeV/c.

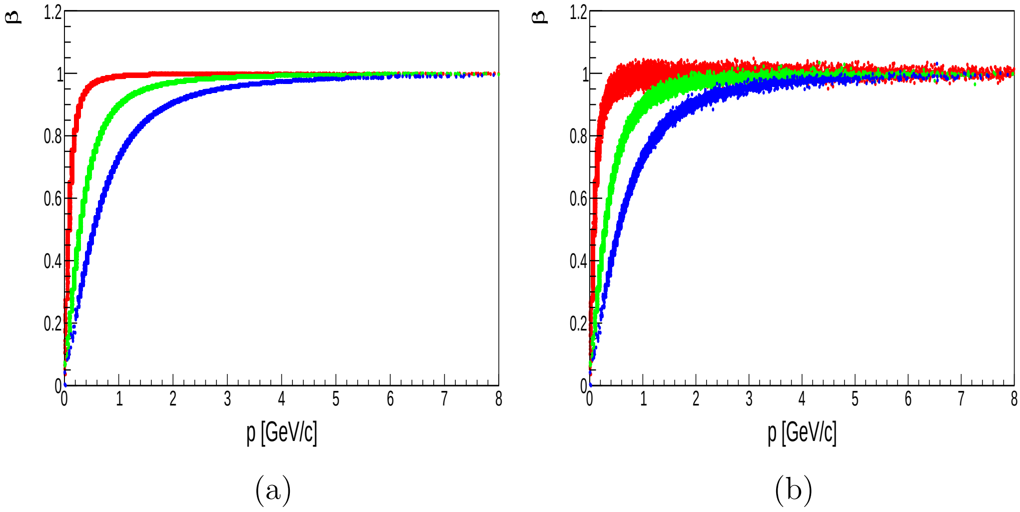

(a) (b)

Figure 7.9: The relative speeds of detected π^- (*red*), K^- (*green*), and $\bar{p}$ (*blue*) for $\sqrt{s} = 26$ GeV as a function of the particle momentum (a) as measured by the TOF system, and (b) with the application of a 100-ps time resolution and a 2% momentum resolution.

The second stage of investigating the possibility of correct antiproton identification was performed after implementing the χ^2-minimization procedure [166] outlined above. The evaluated event collision time was used to reconstruct the mass of negatively-charged pions and kaons, and antiprotons. Figure 7.10 shows the reconstructed masses in terms of momentum for the three species. It was found that antiprotons can be safely separated with a purity of $\sim 99\%$ up to a momentum of 3.5 GeV$/c$[165].

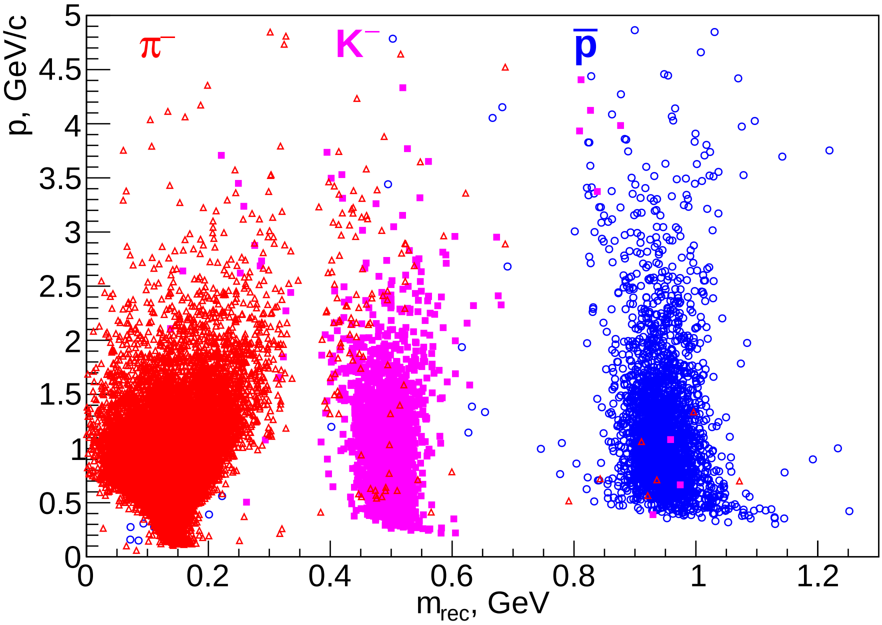

Figure 7.10: Mass reconstruction for π^-, K^-, and $\bar{p}$ using the TOF system. Simulation was performed for $\sqrt{s} = 26$ GeV[165].

In addition to studying primarily-produced antiprotons, the capability of secondary vertex reconstruction at the NICA SPD would provide a chance to enhance our estimation of the $\bar{\Lambda}/\bar{p}$ ratio which has a relative uncertainty level of about 12% for the SPD energies. As mentioned in §5.4, there are no datasets available for the $\bar{\Sigma}^-$-decay, and the ratio $\bar{\Sigma}^-/\bar{p}$ is currently parameterized to be ~ 0.33 with an assumed uncertainty of 25%. It was found that, at $\sqrt{s} = 26$ GeV, almost 93% of the produced $\bar{\Lambda}$'s decay within the inner part of the SPD setup while almost all $\bar{\Sigma}^-$'s decay there. It is thus possible for the SPD to lower both of the uncertainties mentioned above by investigating the antiproton yield from hyperon decay. The range of energies accessible to the SPD is shown in Figure 7.11 with the previous experimental measurements as reference.

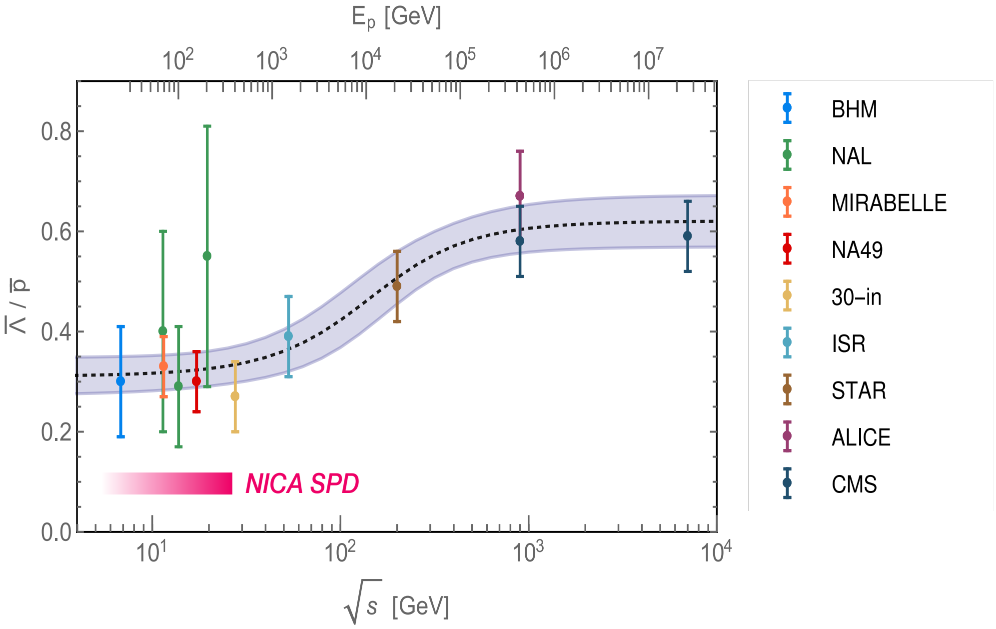

Figure 7.11: $\bar{\Lambda}/\bar{p}$ ratio in proton-proton collisions as measured by several experiments [130]. The range of $\sqrt{s}$ accessible at NICA SPD is shown in red at the lower left part [165].

Some final results obtained by members of the same study [165] are worth mentioning here. It was found that both the invariant masses of $\bar{p}\pi^+$ from $\bar{\Lambda}$ decay and of $\bar{p}\pi^0$ from $\bar{\Sigma}^-$ decay can be estimated with a Gaussian peak widths of 2 MeV and 19 MeV, respectively. In the case of $\bar{\Lambda}$ decays, this is completely defined by momentum measurement uncertainty, while in the case of $\bar{\Sigma}^-$ decays, it is mainly defined by the energy resolution of the electromagnetic calorimeter that detects the pair of photons produced from the π^0 decay in the found secondary vertex. Both of these estimations are shown in Figure 7.12. This promises the ability to finally determine $\bar{\Lambda}/\bar{p}$ and $\bar{\Sigma}^-/\bar{p}$ with minimal uncertainty.

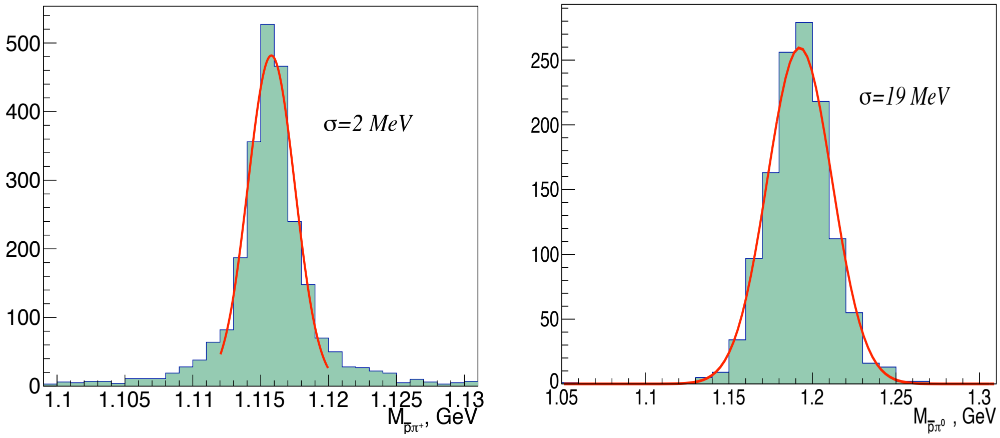

(a) (b)

Figure 7.12: (a) The reconstructed $\bar{p}\pi^+$ invariant mass spectrum with a $\bar{\Lambda}$ signal; and (b) the reconstructed $\bar{p}\pi^0$ invariant mass spectrum with a $\bar{\Sigma}^-$ signal [165].

Requirements

Based upon all of the above results, it was concluded that the Spin Physics Detector at the NICA collider is capable of adding a sizable contribution to the indirect search for DM and probably to our understanding of physics BSM. But first, some requirements must be fulfilled for the SPD to achieve these promising results. The most crucial of these requirements are:

1. A 4π angular acceptance for the solid angle, in order to maximize the kinematic range accessible to the detector and thus covering most of the antiproton yield.
2. A TOF system with a time resolution of 70-80 ps, for precise reconstruction of the event collision time which would consequently

provide a better PID and separation power.

3. The ability to reconstruct secondary vertices, in order to investigate the antiproton yield from hyperon decay, which makes up a significant fraction of the total antiproton yield.

Concluding Remarks

In this work, the accumulating evidence of the existence of DM has been reviewed in Chapter 1. An account of the apparent discrepancy between luminous and gravitational masses in galaxies and galaxy clusters has been given. We have seen how most of the evidence of DM is gravitational in nature. In Chapter 2, we reviewed the basics of particle physics, focusing on the fundamental forces of nature and their respective theories. We also summarized the elementary particles and their classification.

In Chapter 3, an account has been given of different classifications of DM candidates according to their different properties. We then reviewed each of the common candidates and how far the search for them has come. We have seen how they vary from baryonic SM particles, to exotic unknown candidates that were never detected before, to astrophysical objects like MACHOs. We have also seen an example of gravitational theories that try to explain the DM phenomena by a new formulation of gravity.

In Chapter 4, we reviewed the different search approaches employed in pursuing the identity of DM. We have seen how each of them is based on a different paradigm, while they all share some common hypotheses as well. We have discussed how one approach will never be enough to identify DM, and how they complement each other in their common quest. We have reviewed briefly the results obtained by each approach so far and the outlook for upcoming experiments.

In Chapter 5, we explored the properties of CRs, and how secondary CRs are produced in collisions of primary CRs with ISM. We reviewed the recent results from space experiments pursuing the ID of DM. We have seen how the AMS-02 antiproton measurements indicate a signal consistent with a DM particle of mass around 80 GeV/c^2. We have seen how several uncertainties surrounding the signal hinder any conclusions and lower the statistical significance of the signal to below $2\,\sigma$. We reviewed these uncertainties, showing that the antiproton-production cross sections are the most significant source of uncertainty, giving an account of different production mechanisms such as hyperon decay. Finally, we reviewed the outlined parameter space in need of coverage if we were to match the AMS-02 precision; and how several experiments started to include measurements of antiproton yield into their programs.

In Chapter 6, we introduced the upcoming SPD experiment at the NICA collider. We reviewed the planned layout of the detector, and the projected capabilities and limitations of the experiment. A brief account has also been given of the offline analysis toolkit (SpdRoot), which has been used to apply the second stage of the study described in this work.

In Chapter 7, the results of this study were introduced. We began by making the case for our motivation behind the study. Then, we described the study in two stages. The first stage was performed based on simulations using the Pythia8 software; while the second stage was based on simulations using the SpdRoot toolkit. Some of the parameters explored were the expected antiproton yield, the angular distribution of produced antiprotons, the relative contributions of different production mechanisms, the detection efficiency, the separation power, the potential contribution of the proposed measurements to the parameter space outlined for catching up with the AMS-02 precision, and the reconstruction of secondary hyperon decays. Here are a few points that stood out from this study:

- The SPD luminosity could reach 10^{32} cm^{-2}s^{-1}. At a CM energy of about 26 GeV, the inclusive antiproton-production cross section would be on the level of a few millibarns. This corresponds to an antiproton-production rate on a level greater than 10^5 s^{-1}. Thus, statistics will not be an issue.

- Unlike experiments operating in fixed-target mode, the 4π coverage, allowed by the collision mode of the SPD, gives it an advantage in efficiently detecting the antiproton yield in terms of angular distribution. This will in turn enhance the accuracy of the cross sections measured and lower corresponding uncertainties.
- The bulk of antiprotons produced has momenta below 5 GeV/c, making them accessible for detection within the SPD kinematic range. Moreover, the yield distribution over momenta is similar for different production mechanisms, which makes any results representative of the overall yield. It was shown that the detection efficiency could reach up to 97% at higher momenta.
- The measurements proposed to be performed at the SPD will represent a significant contribution to the parameter space outlined for matching the AMS-02 precision level. While no single experiment can cover the entire parameter space, contributions from several experiments can make faster progress in covering it; particularly when experiments with diverse energy levels include the measurements as part of their programs.
- A TOF resolution of 70 ps or lower and a momentum resolution of $0.02\,p_{\mathrm{T}}$ allow for the reconstruction of event time with a resolution of 50 ps or lower depending on the track multiplicity.
- The reconstructed event-time is then applied for mass reconstruction of antiprotons and negatively charged pions and kaons. The

results show that antiprotons could be safely separated with a purity around 99% for momenta up to 3.5 GeV/c.

- The ability to reconstruct secondary hyperon decays will finally allow us to lower the uncertainty on the $\bar{\Lambda}/\bar{p}$-ratio. This will consequently lower the uncertainty on the inclusive production cross section.

- For the proposed measurements to achieve the promised results, a TOF resolution of 70-80 ps is required; along with a 4π angular coverage, and the ability to reconstruct secondary vertices for decays of short-lived particles.

- Based on the study outlined in this thesis, the proposed antiproton-production cross section measurements have been included in the physics program for the first stage of the SPD, which is planned to begin in 2025. Later stages of the experiment could also include the corresponding measurements for helium-3 and helium-4 nuclei if they become available at the NICA collider. It would also be possible then to use any combination of available beams.

- The polarization feature of the colliding beams is not currently necessary for the proposed measurements. However, there is a possibility that the polarization of the colliding particles would affect the yield in a way that makes it necessary to take it into account when it comes to CR antiprotons. If, or when, that occurs, the measurements performed by the SPD will be particularly valuable.

From the above results, we can draw the conclusion that the SPD experiment planned at the NICA collider can significantly contribute to space experiments for the ID search for DM, which could open the door to physics BSM, by performing the proposed measurements of antiproton-production cross sections. Nevertheless, this study is only a first step in a long road to the desired output. In light of these results, however, some future steps can be outlined. These include reevaluation of the obtained results once the SPD plans have been finalized, and modeling the astrophysical results based on MC simulation studies performed in light of the SPD capabilities. Naturally, further assessment of the astrophysical results can be performed after the start of the SPD run.

References

[1] J. R. Primack and N. E. Abrams. Cosmic questions. 950:1–16, 2001.

[2] D. W. Sciama. *Modern Cosmology and the Dark Matter Problem.* Cambridge University Press, 2003.

[3] M. Livio, editor. *The Dark Universe: Matter, Energy and Gravity.* Cambridge University Press, 2016.

[4] S. Matarrese, M. Colpi, V. Gorini, and U. Moschella, editors. *Dark Matter and Dark Energy: A Challenge for Modern Cosmology.* Springer-Verlag GmbH, 2011.

[5] D. Majumdar. *Dark Matter: An Introduction.* CRC Press, 2014.

[6] K. Freeman and G. McNamara. *In Search of Dark Matter.* Springer-Verlag New York Inc., 2006.

[7] J. Einasto, A. Kaasik, and E. Saar. Dynamic evidence on massive coronas of galaxies. *Nature*, 250:309–310, 1974.

[8] J. Bahcall, T. Piran, and S. Weinberg, editors. *Dark Matter In The Universe.* World Scientific Publishing Co. Pte. Ltd., second edition, 2004.

[9] V. C. Rubin, Jr. W. K. Ford, and N. Thonnard. Extended rotation curves of high-luminosity spiral galaxies. IV - Systematic dynamical properties, SA through SC. *The Astrophysical Journal*, 225:L107, 1978.

[10] G. Bertone, editor. *Particle Dark Matter: Observations, Models and Searches.* Cambridge University Press, 2010.

[11] A. De Angelis and M. Pimenta. *Introduction to Particle and Astroparticle Physics: Multimessenger Astronomy and its Particle Physics Foundations (Undergraduate Lecture Notes in Physics).* Springer, 2018.

[12] G. Kane. *Modern Elementary Particle Physics.* Cambridge University Press, 2019.

[13] H. V. Klapdor-Kleingrothaus, K. Zuber, and B. Sadoulet. Particle astrophysics. *Physics Today*, 51(11):66–69, 1998.

[14] P. D. B. Collins, A. D. Martin, and E. J. Squires. *Particle Physics and Cosmology.* John Wiley & Sons, Inc., 1989.

[15] D. H. Perkins. *Particle Astrophysics.* Oxford University Press, 2003.

[16] M. Tanabashi et al. Review of Particle Physics. *Phys. Rev. D*, 98:030001, 2018.

[17] R. Purdy. *Particle Physics: An Introduction.* MERCURY LEARNING & INFORMATION, 2018.

[18] V. P. Nair. *Concepts in Particle Physics.* WSPC, 2017.

[19] T. W. Donnelly, J. A. Formaggio, and B. R. Holstein. *Foundations of Nuclear and Particle Physics.* Cambridge University Press, 2019.

[20] G. E. Marsh. *An Introduction to the Standard Model of Particle Physics for the Non-Specialist*. WSPC, 2017.

[21] G. Aad et al. Combined search for the standard model higgs boson inppcollisions ats=7 TeVwith the ATLAS detector. *Phys. Rev. D*, 86(3), 2012.

[22] S. Chatrchyan et al. Observation of a new boson at a mass of 125 GeV with the CMS experiment at the LHC. *Phys. Lett. B*, 716(1):30–61, 2012.

[23] J. F. Donoghue, E. Golowich, and B. R. Holstein. *Dynamics of the Standard Model*. Cambridge University Press, 2009.

[24] R. E. Marshak. *Conceptual Foundations of Modern Particle Physics*. World Scientific Publishing Company, 1993.

[25] I. Aitchison. *Gauge Theories in Particle Physics : A Practical Introduction*. Institute of Physics Pub, 1989.

[26] J. M. Overduin. *Dark sky, dark matter*. Institute of Physics Pub, 2003.

[27] M. Fukugita, C. J. Hogan, and P. J. E. Peebles. The cosmic baryon budget. *The Astrophysical Journal*, 503(2):518–530, 1998.

[28] J. Einasto. *Dark Matter and Cosmic Web Story*. WORLD SCIENTIFIC, 2013.

[29] E. Komatsu et al. Seven-Year Wilkinson Microwave Anisotropy Probe (WMAP) Observations: Cosmological Interpretation. *The Astrophysical Journal Supplement Series*, 192(2):18, 2011.

[30] Y. Akrami et al. Planck 2018 results. i. overview and the cosmological legacy of planck.

[31] L. Papantonopoulos, editor. *The Invisible Universe: Dark Matter and Dark Energy.* Springer Berlin Heidelberg, 2007.

[32] B. Paczynski. Gravitational microlensing by the galactic halo. *The Astrophysical Journal*, 304:1, 1986.

[33] K. H. Cook et al. A Feasibility Study for Detection of Gravitational Microlensing by Baryonic Dark Matter via CCD Photometry. In *BAAS*, volume 23, page 952, 1991.

[34] K. Griest. *WIMPs and MACHOs*, page E2634. 2002.

[35] C. Alcock et al. Possible gravitational microlensing of a star in the large magellanic cloud. *Nature*, 365(6447):621–623, 1993.

[36] C. Alcock et al. The MACHO project: Microlensing results from 5.7 years of large magellanic cloud observations. *The Astrophysical Journal*, 542(1):281–307, 2000.

[37] P. Tisserand et al. Limits on the macho content of the galactic halo from the EROS-2 survey of the magellanic clouds. *Astronomy & Astrophysics*, 469(2):387–404, 2007.

[38] S. Mao et al. Optical gravitational lensing experiment OGLE 1999 BUL 32: the longest ever microlensing event – evidence for a stellar mass black hole? *MNRAS*, 329(2):349–354, 2002.

[39] M. C. Smith et al. Optical gravitational lensing experiment: OGLE-1999-BUL-19 – the first multipeak parallax event. *MNRAS*, 336(2):670–684, 2002.

[40] K. Akiyama et al. First M87 Event Horizon Telescope Results. I. The Shadow of the Supermassive Black Hole. 875(1):L1, 2019.

[41] M. R. S. Hawkins. The case for primordial black holes as dark matter. *MNRAS*, 415(3):2744–2757, 2011.

[42] S. Hawking. Gravitationally Collapsed Objects of Very Low Mass. *MNRAS*, 152(1):75–78, 1971.

[43] S. W. Hawking, I. G. Moss, and J. M. Stewart. Bubble collisions in the very early universe. *Phys. Rev. D*, 26(10):2681–2693, 1982.

[44] M. W. Choptuik. Universality and scaling in gravitational collapse of a massless scalar field. *Phys. Rev. Lett.*, 70(1):9–12, 1993.

[45] H. I. Kim. Primordial black holes under the double inflationary power spectrum. *Phys. Rev. D*, 62(6), 2000.

[46] S. W. Hawking. Black holes from cosmic strings. *Phys. Lett. B*, 231(3):237–239, 1989.

[47] B. Ya. Zel'dovich and I. D. Novikov. The Hypothesis of Cores Retarded during Expansion and the Hot Cosmological Model. *Sov. Astron.*, 10:602, 1967.

[48] S. W. Hawking. Black hole explosions? *Nature*, 248(5443):30–31, 1974.

[49] B. Carr, F. KÃijhnel, and M. Sandstad. Primordial black holes as dark matter. *Phys. Rev. D*, 94(8), 2016.

[50] D. N. Page and S. W. Hawking. Gamma rays from primordial black holes. *Astrophys. J.*, 206:1–7, 1976.

[51] B. J. Carr. Some cosmological consequences of primordial black-hole evaporations. *Astrophys. J.*, 206:8–25, 1976.

[52] F. Halzen, B. Keszthelyi, and E. Zas. Neutrinos from primordial black holes. *Phys. Rev. D*, 52(6):3239–3247, 1995.

[53] A. Barrau et al. Antiprotons from primordial black holes. *Astronomy & Astrophysics*, 388(2):676–687, 2002.

[54] A. Barrau et al. Antideuterons as a probe of primordial black holes. *Astronomy & Astrophysics*, 398(2):403–410, 2003.

[55] E. Kotok and P. Naselsky. Blue spectra and induced formation of primordial black holes. *Phys. Rev. D*, 58(10), 1998.

[56] M. K. Parikh and F. Wilczek. Hawking Radiation As Tunneling. *Phys. Rev. Lett.*, 85(24):5042–5045, 2000.

[57] S. O. Alexeyev, M. V. Sazhin, and M. V. Pomazanov. Black Holes of A Minimial Size in String Gravity. *International Journal of Modern Physics D*, 10(02):225–230, 2001.

[58] R. Murgia, G. Scelfo, M. Viel, and A. Raccanelli. Lyman- α Forest Constraints on Primordial Black Holes as Dark Matter. *Phys. Rev. Lett.*, 123(7), 2019.

[59] C. L. Cowan, F. Reines, F. B. Harrison, H. W. Kruse, and A. D. McGuire. Detection of the Free Neutrino: a Confirmation. *Science*, 124(3212):103–104, 1956.

[60] J. M. Overduin and P. S. Wesson. *The Light/Dark Universe: Light From Galaxies, Dark Matter And Dark Energy.* World Scientific, 2008.

[61] M. Bauer and T. Plehn. *Yet Another Introduction to Dark Matter*. Springer International Publishing, 2019.

[62] V. Barger. *The Physics of Neutrinos*. Princeton University Press, 2012.

[63] M. Aker et al. Improved Upper Limit on the Neutrino Mass from a Direct Kinematic Method by KATRIN. *Phys. Rev. Lett.*, 123(22), 2019.

[64] G. Bertone et al. Identifying WIMP dark matter from particle and astroparticle data. *JCAP*, 2018(03):026–026, 2018.

[65] B. W. Lee and S. Weinberg. Cosmological Lower Bound on Heavy-Neutrino Masses. *Phys. Rev. Lett.*, 39(4):165–168, 1977.

[66] H. V. Klapdor-Kleingrothaus and R. Arnowitt, editors. *Dark Matter in Astro- and Particle Physics*. Springer Berlin Heidelberg, 2005.

[67] A. Boyarsky, M. Drewes, T. Lasserre, S. Mertens, and O. Ruchayskiy. Sterile Neutrino Dark Matter. *Progress in Particle and Nuclear Physics*, 104:1–45, 2019.

[68] E. Kh. Akhmedov, G. C. Branco, and M. N. Rebelo. Seesaw mechanism and structure of neutrino mass matrix. *Phys. Lett. B*, 478(1-3):215–223, 2000.

[69] R. N. Mohapatra. Seesaw Mechanism and Its Implications. In *Seesaw25*. World Scientific, 2005.

[70] A. Rudakovskyi and D. Iakubovskyi. Dark matter model favoured by reionization data: 7 keV sterile neutrino versus cold dark matter. *MNRAS*, 483(3):4080–4084, 2018.

[71] G. M. Fuller, A. Kusenko, I. Mocioiu, and S. Pascoli. Pulsar kicks from a dark-matter sterile neutrino. *Phys. Rev. D*, 68(10), 2003.

[72] A. Kusenko, B. P. Mandal, and A. Mukherjee. Delayed pulsar kicks from the emission of sterile neutrinos. *Phys. Rev. D*, 77(12), 2008.

[73] M. Srednicki, editor. *Particle Physics and Cosmology: Dark Matter*. North-Holland, 1990.

[74] T. P. Sotiriou and V. Faraoni. $f(R)$ Theories of Gravity. *Reviews of Modern Physics*, 82(1):451–497, 2010.

[75] Y. Zhang, H. Li, Y. Gong, and Z. Zhu. Notes on $f(T)$ Theories. *JCAP*, 2011(07):015–015, 2011.

[76] M. Milgrom. A modification of the Newtonian dynamics as a possible alternative to the hidden mass hypothesis. *The Astrophysical Journal*, 270:365–370, 1983.

[77] R. Sanders. Modified Gravity Without Dark Matter. In *Lecture Notes in Physics*, pages 375–402. Springer Berlin Heidelberg, 2007.

[78] R. Sanders. *The dark matter problem : a historical perspective*. Cambridge University Press, 2010.

[79] R. H. Sanders. Clusters of galaxies with modified Newtonian dynamics. *MNRAS*, 342(3):901–908, 2003.

[80] J. D. Bekenstein. Relativistic gravitation theory for the modified Newtonian dynamics paradigm. *Phys. Rev. D*, 70(8), 2004.

[81] A. Boveia and C. Doglioni. Dark Matter Searches at Colliders. *Annual Review of Nuclear and Particle Science*, 68(1):429–459, 2018.

[82] O. Buchmueller, C. Doglioni, and L. Wang. Search for dark matter at colliders. *Nature Physics*, 13(3):217–223, 2017.

[83] M. Bauer and T. Plehn. Collider Searches. In *Yet Another Introduction to Dark Matter*, pages 145–173. Springer International Publishing, 2019.

[84] P. J. Fox, R. Harnik, J. Kopp, and Y. Tsai. LEP shines light on dark matter. *Phys. Rev. D*, 84(1):014028, 2011.

[85] J. A. Evans, S. Gori, and J. Shelton. Looking for the WIMP next door. *Journal of High Energy Physics*, 2018(2), 2018.

[86] D. Abercrombie et al. Dark Matter benchmark models for early LHC Run-2 Searches: Report of the ATLAS/CMS Dark Matter Forum. *Physics of the Dark Universe*, 27:100371, 2020.

[87] A. Djouadi, O. Lebedev, Y. Mambrini, and J. Quevillon. Implications of LHC searches for Higgs-portal dark matter. *Phys. Lett. B*, 709(1-2):65–69, 2012.

[88] M. Escudero, A. Berlin, D. Hooper, and M. Lin. Toward (finally!) ruling out Z and Higgs mediated dark matter models. *JCAP*, 2016(12):029–029, 2016.

[89] J. Goodman, M. Ibe, A. Rajaraman, W. Shepherd, T. M. P. Tait, and H. Yu. Constraints on dark matter from colliders. *Phys. Rev. D*, 82(11):116010, 2010.

[90] P. J. Fox, R. Harnik, J. Kopp, and Y. Tsai. Missing energy signatures of dark matter at the LHC. *Phys. Rev. D*, 85(5):056011, 2012.

[91] J. Alwall, P. C. Schuster, and N. Toro. Simplified models for a first characterization of new physics at the LHC. *Phys. Rev. D*, 79(7):075020, 2009.

[92] D. Alves et al. Simplified models for LHC new physics searches. *Journal of Physics G: Nuclear and Particle Physics*, 39(10):105005, 2012.

[93] I. Boucheneb, G. Cacciapaglia, A. Deandrea, and B. Fuks. Revisiting monotop production at the LHC. *Journal of High Energy Physics*, 2015(1), 2015.

[94] M. Blanke and S. Kast. Top-flavoured dark matter in Dark Minimal Flavour Violation. *Journal of High Energy Physics*, 2017(5), 2017.

[95] K. A. Olive. Review of Particle Physics. *Chinese Physics C*, 40(10):100001, 2016.

[96] K. M. Zurek. Asymmetric Dark Matter: Theories, signatures, and constraints. *Physics Reports*, 537(3):91–121, 2014.

[97] Y. Hochberg, E. Kuflik, T. Volansky, and J. G. Wacker. Mechanism for Thermal Relic Dark Matter of Strongly Interacting Massive Particles. *Phys. Rev. Lett.*, 113(17):171301, 2014.

[98] N. Craig, S. Knapen, and P. Longhi. Neutral Naturalness from Orbifold Higgs Models. *Phys. Rev. Lett.*, 114(6):061803, 2015.

[99] M. Aaboud et al. Search for Low-Mass Dijet Resonances Using Trigger-Level Jets with the ATLAS Detector in pp Collisions at $\sqrt{s} = 13$ TeV. *Phys. Rev. Lett.*, 121(8), 2018.

[100] ATLAS Collaboration. *Summary plots from the ATLAS exotic physics group.* CERN, Geneva, 2018.

[101] P. Athron et al. GAMBIT: the global and modular beyond-the-standard-model inference tool. *Eur. Phys. J. C*, 77(784), 2017.

[102] E. Bagnaschi et al. Likelihood analysis of the pMSSM11 in light of LHC 13-TeV data. *Eur. Phys. J. C*, 78(256), 2018.

[103] M. Schumann. Direct detection of WIMP dark matter: concepts and status. *Journal of Physics G: Nuclear and Particle Physics*, 46(10):103003, 2019.

[104] G. Heusser. Low-Radioactivity Background Techniques. *Annual Review of Nuclear and Particle Science*, 45(1):543–590, 1995.

[105] R. Bernabei et al. First results from DAMA/LIBRA and the combined results with DAMA/NaI. *Eur. Phys. J. C*, 56(3):333–355, 2008.

[106] S. Archambault et al. Constraints on low-mass WIMP interactions on 19F from PICASSO. *Phys. Lett. B*, 711(2):153–161, 2012.

[107] M. Battaglieri et al. US Cosmic Visions: New Ideas in Dark Matter 2017: Community Report. 2017.

[108] M. Bauer and T. Plehn. Indirect Searches. In *Yet Another Introduction to Dark Matter*, pages 111–127. Springer International Publishing, 2019.

[109] J. Lavalle and P. Salati. Dark matter indirect signatures. *Comptes Rendus Physique*, 13(6-7):740–782, 2012.

[110] M. Aguilar et al. First Result from the Alpha Magnetic Spectrometer on the International Space Station: Precision Measurement of the Positron Fraction in Primary Cosmic Rays of 0.5–350 GeV. *Phys. Rev. Lett.*, 110(14), 2013.

[111] C. Grupen. Primary Cosmic Rays. In *Astroparticle Physics*, pages 121–233. Springer International Publishing, 2020.

[112] R. Cowsik. Positrons and Antiprotons in Galactic Cosmic Rays. *Annual Review of Nuclear and Particle Science*, 66(1):297–319, 2016.

[113] P. Blasi. Recent Results in Cosmic Ray Physics and Their Interpretation. *Brazilian Journal of Physics*, 44(5):426–440, 2014.

[114] C. Evoli, D. Gaggero, and D. Grasso. Secondary antiprotons as a Galactic Dark Matter probe. *JCAP*, 2015(12):039–039, 2015.

[115] C. Grupen. Secondary Cosmic Rays. In *Astroparticle Physics*, pages 235–291. Springer International Publishing, 2020.

[116] O. Adriani et al. PAMELA Measurements of Cosmic-Ray Proton and Helium Spectra. *Science*, 332(6025):69–72, 2011.

[117] M. Aguilar et al. Precision Measurement of the Proton Flux in Primary Cosmic Rays from Rigidity 1 GV to 1.8 TV with the Alpha Magnetic Spectrometer on the International Space Station. *Phys. Rev. Lett.*, 114(17), 2015.

[118] M. Aguilar et al. Precision Measurement of the Helium Flux in Primary Cosmic Rays of Rigidities 1.9 GV to 3 TV with the Alpha Magnetic Spectrometer on the International Space Station. *Phys. Rev. Lett.*, 115(21), 2015.

[119] NA49 experiment website.

[120] R. Kappl and M. W. Winkler. The cosmic ray antiproton background for AMS-02. *JCAP*, 2014(09):051–051, 2014.

[121] M. di Mauro, F. Donato, A. Goudelis, and P. D. Serpico. New evaluation of the antiproton production cross section for cosmic ray studies. *Phys. Rev. D*, 90(8), 2014.

[122] J. F. Navarro, C. S. Frenk, and S. D. M. White. The Structure of Cold Dark Matter Halos. *The Astrophysical Journal*, 462:563, 1996.

[123] I. Cholis, T. Linden, and D. Hooper. A robust excess in the cosmic-ray antiproton spectrum: Implications for annihilating dark matter. *Phys. Rev. D*, 99(10), 2019.

[124] G. Giesen et al. AMS-02 antiprotons, at last! Secondary astrophysical component and immediate implications for Dark Matter. *JCAP*, 2015(09):023–023, 2015.

[125] A. Cuoco, M. KrÃďmer, and M. Korsmeier. Novel Dark Matter Constraints from Antiprotons in Light of AMS-02. *Phys. Rev. Lett.*, 118(19), 2017.

[126] R. Kappl, A. Reinert, and M. W. Winkler. AMS-02 antiprotons reloaded. *JCAP*, 2015(10):034–034, 2015.

[127] M. Korsmeier, F. Donato, and M. Di Mauro. Production cross sections of cosmic antiprotons in the light of new data from the NA61 and LHCb experiments. *Phys. Rev. D*, 97(10), 2018.

[128] K. LÃijbelsmeyer et al. Upgrade of the Alpha Magnetic Spectrometer (AMS-02) for long term operation on the International Space

Station (ISS). *Nuclear Instruments and Methods in Physics Research Section A: Accelerators, Spectrometers, Detectors and Associated Equipment*, 654(1):639–648, 2011.

[129] M. Aguilar et al. Antiproton Flux, Antiproton-to-Proton Flux Ratio, and Properties of Elementary Particle Fluxes in Primary Cosmic Rays Measured with the Alpha Magnetic Spectrometer on the International Space Station. *Phys. Rev. Lett.*, 117(9), 2016.

[130] M. W. Winkler. Cosmic ray antiprotons at high energies. *JCAP*, 2017(02):048–048, 2017.

[131] Y. S. Yoon et al. COSMIC-RAY PROTON AND HELIUM SPECTRA FROM THE FIRST CREAM FLIGHT. *The Astrophysical Journal*, 728(2):122, 2011.

[132] L. Accardo et al. High Statistics Measurement of the Positron Fraction in Primary Cosmic Rays of 0.5–500 GeV with the Alpha Magnetic Spectrometer on the International Space Station. *Phys. Rev. Lett.*, 113(12), 2014.

[133] X. Huang, C. Wei, Y. Wu, W. Zhang, and Y. Zhou. Antiprotons from dark matter annihilation through light mediators and a possible excess in AMS-02 p^{-}/p data. *Phys. Rev. D*, 95(6), 2017.

[134] A. Reinert and M. W. Winkler. A precision search for WIMPs with charged cosmic rays. *JCAP*, 2018(01):055–055, 2018.

[135] M. Cui, Q. Yuan, Y. S. Tsai, and Y. Fan. Possible Dark Matter Annihilation Signal in the AMS-02 Antiproton Data. *Phys. Rev. Lett.*, 118(19), 2017.

[136] C. Chen, C. Chiang, and T. Nomura. Dark matter for excess of AMS-02 positrons and antiprotons. *Phys. Lett. B*, 747:495–499, 2015.

[137] A. Cuoco, J. Heisig, L. Klamt, M. Korsmeier, and M. KrÃďmer. Scrutinizing the evidence for dark matter in cosmic-ray antiprotons. *Phys. Rev. D*, 99(10), 2019.

[138] M. Boudaud et al. AMS-02 antiprotons' consistency with a secondary astrophysical origin. *Physical Review Research*, 2(2), 2020.

[139] M. Cui, X. Pan, Q. Yuan, Y. Fan, and H. Zong. Revisit of cosmic ray antiprotons from dark matter annihilation with updated constraints on the background model from AMS-02 and collider data. *JCAP*, 2018(06):024–024, 2018.

[140] E. S. Seo and V. S. Ptuskin. Stochastic reacceleration of cosmic rays in the interstellar medium. *The Astrophysical Journal*, 431:705, 1994.

[141] M. Aguilar et al. Observation of the Identical Rigidity Dependence of He, C, and O Cosmic Rays at High Rigidities by the Alpha Magnetic Spectrometer on the International Space Station. *Phys. Rev. Lett.*, 119(25), 2017.

[142] M. Aguilar et al. Observation of New Properties of Secondary Cosmic Rays Lithium, Beryllium, and Boron by the Alpha Magnetic Spectrometer on the International Space Station. *Phys. Rev. Lett.*, 120(2), 2018.

[143] H. G. Fischer et al. Baryon Yields, Isospin Effects and Strangeness

Production in Elementary Hadronic Interactions. *Acta Physica Hungarica A) Heavy Ion Physics*, 17(2-4):369–386, 2003.

[144] F. Videbæk and Ole Hansen. Baryon rapidity loss and midrapidity stacking in high energy nucleus-nucleus collisions. *Phys. Rev. C*, 52(5):2684–2693, 1995.

[145] P. A. Zyla et al. Review of Particle Physics. *Progress of Theoretical and Experimental Physics*, 2020(8), 2020.

[146] F. Donato, M. Korsmeier, and M. Di Mauro. Prescriptions on antiproton cross section data for precise theoretical antiproton flux predictions. *Phys. Rev. D*, 96(4), 2017.

[147] R. Aaij et al. Measurement of Antiproton Production in p-He Collisions at sNN=110 GeV. *Phys. Rev. Lett.*, 121(22), 2018.

[148] G. A. de Nolfo. A measurement of cosmic ray deuterium from 0.5–2.9 GeV/nucleon. In *AIP Conference Proceedings*. AIP, 2000.

[149] E. Vannuccinini. *The Study of the Deuterium Spectrum in Cosmic Rays with the CAPRICE98 Experiment.* PhD thesis, University of Florence, 2001.

[150] T. L. Wilson and R. T. Rood. Abundances in the Interstellar Medium. *Annual Review of Astronomy and Astrophysics*, 32(1):191–226, 1994.

[151] A. Guskov and R. El-Kholy. On the Possibility to Study Antiproton Production at the SPD Detector at NICA Collider for Dark Matter Search in Astrophysical Experiments. *Phys. Part. Nucl. Lett.*, 16(3):216–223, 2019.

[152] P. von Doetinchem et al. Cosmic-ray antinuclei as messengers of new physics: status and outlook for the new decade. *JCAP*, 2020(08):035–035, 2020.

[153] N. Abgrall et al. NA61/SHINE facility at the CERN SPS: beams and detector system. *Journal of Instrumentation*, 9(06):P06005–P06005, 2014.

[154] B. Adams et al. Letter of Intent: A New QCD facility at the M2 beam line of the CERN SPS (COMPASS++/AMBER). 2018.

[155] V. M. Abazov et al. Conceptual Design of the Spin Physics Detector. 2021.

[156] A. D. Kovalenko et al. NICA Facility in Polarized Proton and Deuteron Mode. *International Journal of Modern Physics: Conference Series*, 40:1660096, 2016.

[157] I. N. Meshkov. Luminosity of an Ion Collider. *Phys. Part. Nucl.*, 50(6):663–682, 2019.

[158] E. Abat The ATLAS TRT collaboration et al. The ATLAS Transition Radiation Tracker (TRT) proportional drift tube: design and performance. *J. Instrum.*, 3(02):P02013–P02013, 2008.

[159] P. Gianotti et al. The straw tube trackers of the PANDA experiment. In *ANIMMA*. IEEE, 2013.

[160] SpdRoot Package.

[161] M. Al-Turany et al. The FairRoot framework. *J. Phys. Conf. Ser.*, 396(2):022001, 2012.

[162] TorbjÃűrn SjÃűstrand et al. An introduction to PYTHIA 8.2. *Comput. Phys. Commun.*, 191:159–177, 2015.

[163] S. Agostinelli et al. Geant4—a simulation toolkit. *Nucl. Instrum. Methods Phys. Res., Sect. A*, 506(3):250–303, 2003.

[164] Conceptual design report of the SPD experiment, 2021.

[165] V. Alexakhin, A. Guskov, Z. Hayman, R. El-Kholy, and A. Tkachenko. On the study of antiprotons yield in hadronic collisions at NICA SPD. 18(2):196–201, 2021.

[166] J. Adam et al. Determination of the event collision time with the ALICE detector at the LHC. *The European Physical Journal Plus*, 132(2), 2017.

Arabic Summary

الفصل الرابع: طرق البحث عن المادة المظلمة

في هذا الفصل، تمت مناقشة الطرق المختلفة التي يتم تكريثها للسعي وراء هوية المادة المظلمة؛ بما في ذلك البحث في تجارب المصادمات، وتجارب الكشف المباشر، وغير المباشر عن المادة المظلمة. كما تم استعراض الفرضيات الكامنة وراء كل من طرق البحث المختلفة، إلى جانب الفرضيات المشتركة بينها. وتم استعراض النتائج الأخيرة والتجارب المستقبلية فيما يخص كل طريقة للبحث، على نحو مختصر.

الفصل الخامس: البروتونات المضادة كأداة لسبر المادة المظلمة

في هذا الفصل، تمت مناقشة خواص الأشعة الكونية الأولية والثانوية. كما تم استعراض النتائج الأخيرة، فيما يخص البروتونات المضادة، للتجارب الفضائية للكشف غير المباشر عن المادة المظلمة. وتم استكشاف مصادر عدم التأكد المحيطة بالإشارة الأخيرة لتجربة «مطياف ألفا المغناطيسي». كما تمت مناقشة الخطوات القادمة والاحتمالات الممكنة للحد من مصادر عدم التأكد.

الفصل السادس: «مكشاف فيزياء الغزل» بمصادم «نِيكا»

في هذا الفصل، تم تقديم تجربة «مكشاف فيزياء الغزل». كما تم تحديد الدافع وراء التجربة وأهداف البرنامج الفيزيائي لها. وتم وصف التصميم العام للمكشاف ومكوناته الرئيسية. كما تمت مناقشة النظام الحوسبي للتجربة وحقيبة البرمجيات المخصصة لتحليل بياناتها. وأخيرًا تم استعراض المخطط الزمني للتجربة.

الفصل السابع: قياس إنتاج البروتونات المضادة بمصادم «نِيكا»

في هذا الفصل، تم البدء بمقدمة عن الدافع وراء هذا العمل. ثم تم اقتراح قياس إنتاج البروتونات المضادة بـ«مكشاف فيزياء الغزل». بعد ذلك، تم إجراء دراسة محاكاة من مرحلتين: الأولى باستخدام «بيثيا٨»، والثانية باستخدام حقيبة «إس بي دي رووت» البرمجية. تم تقييم النواحي المختلفة للقياسات المقترحة ومتطلباتها في ضوء الإمكانات المتوقعة لـ«مكشاف فيزياء الغزل». وأخيرًا، تمت مناقشة النتائج التي تم الحصول عليها والخطوات القادمة التي مهدت لها هذه الرسالة.

الملخص

إنتاج البروتونات المضادة في تفاعلات الأنوية الخفيفة والبحث عن المادة المظلمة في التجارب الفضائية

الهدف من هذه الرسالة هو مناقشة النتائج الأخيرة، فيما يخص البروتونات المضادة، للتجارب الفضائية للكشف غير المباشر عن المادة المظلمة؛ ومناقشة مصادر عدم التأكد المحيطة بالإشارة الأخيرة لتجربة «مطياف ألفا المغناطيسي»؛ وأخيرًا، التحقق من إمكانية قياس إنتاج البروتونات المضادة في تجربة «مكشاف فيزياء الغزل» المقرر إنشاءه بمصادم «نِيكا».

تحتوي الرسالة على سبعة فصول، وقائمة مراجع:

الفصل الأول: الأدلة على المادة المظلمة

في هذا الفصل، تمت مناقشة الأدلة على وجود المادة المظلمة؛ مع التركيز على منحنيات دوران المجرات الحلزونية، وفروق الكتلة في الحشود المجرية، وأرصاد المفعول العدسي التثاقلي في غياب العدسات المضيئة. كما تمت مناقشة حدث «حشد الرصاصة» باعتباره مؤشر على الطبيعة اللا تصادمية للمادة المظلمة.

الفصل الثاني: أساسيات فيزياء الجسيمات

في هذا الفصل، تم استعراض الجسيمات الأساسية في نظرية النموذج العياري لفيزياء الجسيمات. كما تمت مناقشة القوى الأربعة الرئيسية في الطبيعة، بالإضافة إلى النظرية التي تحكم كل منها والجسيمات التي تتوسط التفاعلات القائمة عليها. وتمت أيضًا مناقشة نجاحات نظرية النموذج العياري وتحدياتها.

الفصل الثالث: أنواع المادة المظلمة ومرشحيها

في هذا الفصل، تمت مناقشة التصنيفات المختلفة لمرشحي المادة المظلمة. كما تم استعراض المرشحين المفضلين بمزيد من التفصيل؛ بما في ذلك، أجرام الـ«ماتشو»، وجسيمات الـ«ويمب»، وجسيمات الـ«أكسيون»، وغيرها. كما تمت مناقشة التفسيرات البديلة لظواهر المادة المظلمة في ضوء نظريات التثاقل المُحوَّر.

إنتاج البروتونات المضادة في تفاعلات الأنوية الخفيفة والبحث عن المادة المظلمة في التجارب الفضائية

إعداد

ريهام إبراهيم سيد إبراهيم

رسالة مقدمة

إلى

كلية العلوم

كجزء من متطلبات الحصول على

درجة دكتوراه الفلسفة

(فلك رياضي)

قسم علوم الفلك والفضاء والأرصاد الجوية

كلية العلوم

جامعة القاهرة

(٢٠٢١)